AJS American Journal of Science
publishing earth-sciences research since 1818

de Hoÿm de Marien, L., Štípská, P., Schulmann, K., Kylander-Clark, A., Lexa, O., Jiang, Y., Jeřábek, P., Racek, M., & Buriánek, D. (2026). Permian Syn-Extensional Barrovian Metamorphism in the Envelope of a Migmatite Dome of the Mongolian Altai – Petrostructural and Geochronological Arguments. *American Journal of Science*, *326*, Article 3. https://doi.org/10.2475/001c.155605

Science Paper

# Permian Syn-Extensional Barrovian Metamorphism in the Envelope of a Migmatite Dome of the Mongolian Altai – Petrostructural and Geochronological Arguments

Luc de Hoÿm de Marien[1][a], Pavla Štípská[1], Karel Schulmann[1], Andrew Kylander-Clark[2], Ondrej Lexa[3], Yingde Jiang[4], Petr Jeřábek[3], Martin Racek[3], David Buriánek[1]

[1] Centre for Lithospheric Research, Czech Geological Survey, [2] Department of Earth Science, University of California, Santa Barbara, [3] Institute of Petrology and Structural Geology, Charles University, [4] State Key Laboratory of Isotope Geochemistry, Guangzhou Institute of Geochemistry

Keywords: petrochronology, Barrovian metamorphism, contact metamorphism, lithosphere-scale extension

https://doi.org/10.2475/001c.155605

American Journal of Science

Vol. 326, 2026

The Paleozoic Altai orogenic belt results from a suprasubduction polycyclic metamorphism of a sedimentary accretionary wedge. In the Mongolian-Altai, a Barrovian-type metamorphic sequence marks the transition between exhumed lower- and upper-crustal domains. It is studied by field and petrological observations, phase equilibria modeling, U-Pb zircon LA-ICP-MS, and in-context monazite LASS geochronology. Prograde micaschist and retrogressed migmatite are juxtaposed by an extensional shear zone hosting variably deformed Permian dikes (*ca.* 295–290 Ma, U-Pb zircon) and a sharp metamorphic gradient (< 5 km from biotite to sillimanite zone). In the hangingwall micaschist, garnet and staurolite size increase in the neck zone of boudinaged quartz veins suggests syntectonic growth during the activity of the shear zone. Sequential growth of garnet 1-chlorite (M1), garnet 2-staurolite or garnet 2-staurolite-kyanite (M2) and sillimanite (M3) indicate M1 P–T increase (525–550 °C, 3–4 kbar to 550–575 °C, 5–6 kbar); M2 isobaric heating (~7 kbar, from 550–575 °C to 625–680 °C) and M3 decompression (<6 kbar). Microtextures indicate garnet 2, staurolite, and sillimanite crystallisation in the extension-related foliation. Monazite in garnet 1 is Carboniferous (*ca.* 350–340 Ma) while monazite related to garnet 2, staurolite and sillimanite is Permian (*ca.* 290–285 Ma). Migmatite contains Devonian zircon (*ca.* 375 Ma) and Permian monazite (*ca.* 285 Ma). Anhedral garnet core in a garnet-kyanite-sillimanite migmatite documents an undated early subsolidus metamorphism. Resorbed kyanite, euhedral sillimanite, and garnet rim document a suprasolidus isothermal decompression (9 to 4–7 kbar at ~750 °C). Melt crystallisation indicates subsequent cooling under the solidus (<700 °C). Formerly shallow-dipping migmatitic foliation is related to the decompression. Monazite crystals associated with either kyanite or sillimanite systematically indicate a Permian age, related to the decompression. Consequently, lower crustal rocks decompression was coeval with magmatism, shearing, and heating higher in the crust. The shear zone accommodated the exhumation of a migmatite dome and focused an intense magmatism, inducing the isobaric heating and related Barrovian metamorphism in the hangingwall micaschists. As such, the envelope of extensional domes appears a favourable site for the development of the Barrovian metamorphic sequence.

## 1. INTRODUCTION

Understanding how metamorphic facies across an orogen, or part of it, relates to the past tectonic history is fundamental for the application of metamorphic petrology to the study of tectonic processes (Miyashiro, 1961). Metamorphic facies series, also called field metamorphic gradients, correlate with the temperature peaks experienced by rocks from a crustal section (Spear et al., 1984). Skrzypek et al. (2016) pointed out that field metamorphic gradients are composite and diachronous features. Consequently, approaches integrating structural studies and recent developments in petrochronology represent an opportunity to decipher the significance of metamorphic gradients in terms of tectonic processes.

Among the facies series observed in nature, the Barrovian mineral sequence is defined in metapelites by the successive appearance of chlorite, biotite, garnet, staurolite,

a Corresponding author: luc.dehoym@gmail.com

kyanite, and sillimanite (Barrow, 1893). This sequence develops in crustal rocks undergoing metamorphism in the range 75–185 °C/kbar (Jamieson et al., 1998). Following the emergence of thermal-mechanical models of crustal thickening (e.g., England & Thompson, 1984; Vanderhaeghe, 2012), it was considered the metamorphic hallmark of thermal maturation during continent-continent collision. However, the Barrovian sequence results from dehydration reactions characterised by steep Clausius-Clapeyron slopes, consequently, its development is controlled by variations of temperature. In agreement, a review by Ryan and Dewey (2019) about tectonic settings accounting for the Barrovian metamorphism shows that the production, addition, and redistribution of heat in the middle- to lower-crust count among the main factors controlling the development of this type of metamorphism. Consequently, the Barrovian sequence is, in fact, not tied to a single tectonic environment and was indeed reported from tectonic settings as varied as convergent collisional (e.g., Himalayas: Kohn, 2014; Le Fort, 1975; Alps: Tagliaferri et al., 2023; Variscides: Burg et al., 1984; Štípská et al., 2015, 2020) and accretionary orogens (e.g., Superior Province: Pan & Fleet, 1999; Altai orogen: Aguilar et al., 2024; Jiang et al., 2019), or even domains undergoing extension (e.g., Štípská et al., 2023; Viete et al., 2010).

Barrovian metamorphism is widely reported in the Altai accretionary orogen (among many others: Jiang et al., 2015; Kozakov et al., 2011; Soejono et al., 2021; Sukhorukov et al., 2016; Wei et al., 2007), but the potential heat source(s) accounting for this metamorphism remain(s) largely overlooked. Yet it is an important question because the protolith of metasediments is dominated by immature greywacke (e.g., Buriánek et al., 2022), moderately depleted in K, Th and U compared to the average upper continental crust (Jiang et al., 2016), while numerical models require exceptional distribution and concentration of heat producing material for significant radiogenic heating to occur (Jamieson et al., 1998). Previous studies have focused on the relationships between magmatism and Buchan-type events (e.g., Burenjargal et al., 2014; Jiang et al., 2010). On the other hand, it is commonly accepted that the Barrovian metamorphism occurred during gaps in the magmatic record (Buriánek et al., 2022). In a petrological and geochronological study of the area of Tseel, Burenjargal et al. (2014) argued that Barrovian-type garnet-staurolite assemblages were overprinted by cordierite and sillimanite during the emplacement of granitoids. In this study, the Barrovian event is referred to as a "high-P and low-T metamorphism". While this makes the comparison with the subsequent lower-pressure and higher-temperature event efficient, it effectively excludes any discussion about potential heat sources for the Barrovian event. Alternatively, a recent study reported the discovery of late-Ordovician (*ca.* 455–445 Ma) igneous rocks intruding the AAW (Hanžl et al., 2024) and proposed a correlation with a late Ordovician (*ca.* 455 Ma) Barrovian metamorphism reported previously (Burenjargal et al., 2014; Soejono et al., 2021), but this hypothesis remains to be proven.

Another important question to be addressed is the tectonic setting and age(s) of the Barrovian metamorphism. Indeed, while Barrovian events are comprehended as relatively cold events intervening higher-temperature ones, garnet-staurolite-kyanite assemblages are commonly geographically associated with migmatite domes (e.g., Jiang et al., 2015; Sukhbaatar et al., 2022; Sukhorukov et al., 2016; Wei et al., 2007). Because staurolite and kyanite occur in the migmatite as xenomorphic relics, they are considered a record of the late Ordovician to Silurian metamorphism, which precedes the dome formation by tens of Myrs (e.g., Jiang et al., 2019, 2022). However, structural studies show that staurolite- and kyanite-bearing foliations in the metamorphic envelopes of the domes progressively grade into the migmatitic foliations in the cores of the domes (Kong et al., 2022; Sukhbaatar et al., 2022) and thus cast doubts about the timing and tectonics of the Barrovian metamorphism. Moreover, in both studies, the migmatitic foliation is interpreted as a result of extensional tectonics. Finally, further complexity regards the age of the domes, dated as Devonian (Kong et al., 2022, 2023) or Permian (Sukhbaatar et al., 2022). Consequently, it is essential to link the structures with the metamorphic minerals and to date the Barrovian assemblages from the dome envelopes *in-context*, directly in thin sections, to determine whether they are older or genetically related to the formation of the domes.

To this end, we re-examined a metamorphic sequence in the Gobi Altai grading from Barrovian schist to migmatite. We paid specific attention to the relative timing of structures, magmatism, and metamorphism. To do so, we combined field and structural data with metamorphic petrology, thermodynamic modeling, monazite U-Pb geochronology of metamorphic rocks, and zircon U-Pb of magmatic ones. The results distinguish three metamorphic events dated to the late Devonian, early Carboniferous, and Permian. The data suggest that the Barrovian-type metamorphism was genetically related to a short-lived magmatic event affecting an extensional shear zone during the formation of a Permian migmatite dome.

## 2. GEOLOGICAL SETTING

### 2.1. Geology of the Central Asian Orogenic Belt

The Central Asian Orogenic Belt (CAOB) is a vast late Proterozoic to Mesozoic accretionary orogen developed between the Baltica, Siberia, Tarim, and Sino-Korean cratons (e.g., Wilhem et al., 2012; Windley et al., 2007). In the Mongolian portion of the CAOB, the Mongolian Altai intervenes the Lake and Trans-Altai zones (fig. 1). The Lake zone is a composite unit of Neoproterozoic oceanic crust and arc complexes (e.g., Jian et al., 2014; Kepezhinskas et al., 1991; Khukhuudei et al., 2020) imbricated with Precambrian basement blocks (e.g., Buriánek et al., 2017; Štípská et al., 2010). The Trans-Altai Zone is dominantly an oceanic succession (e.g., Badarch et al., 2002) including Silurian deep marine to Devonian and early Carboniferous shallow water volcanic and sedimentary sequences (Hanžl et al., 2023; Lamb & Badarch, 1997; Nguyen et al., 2018).

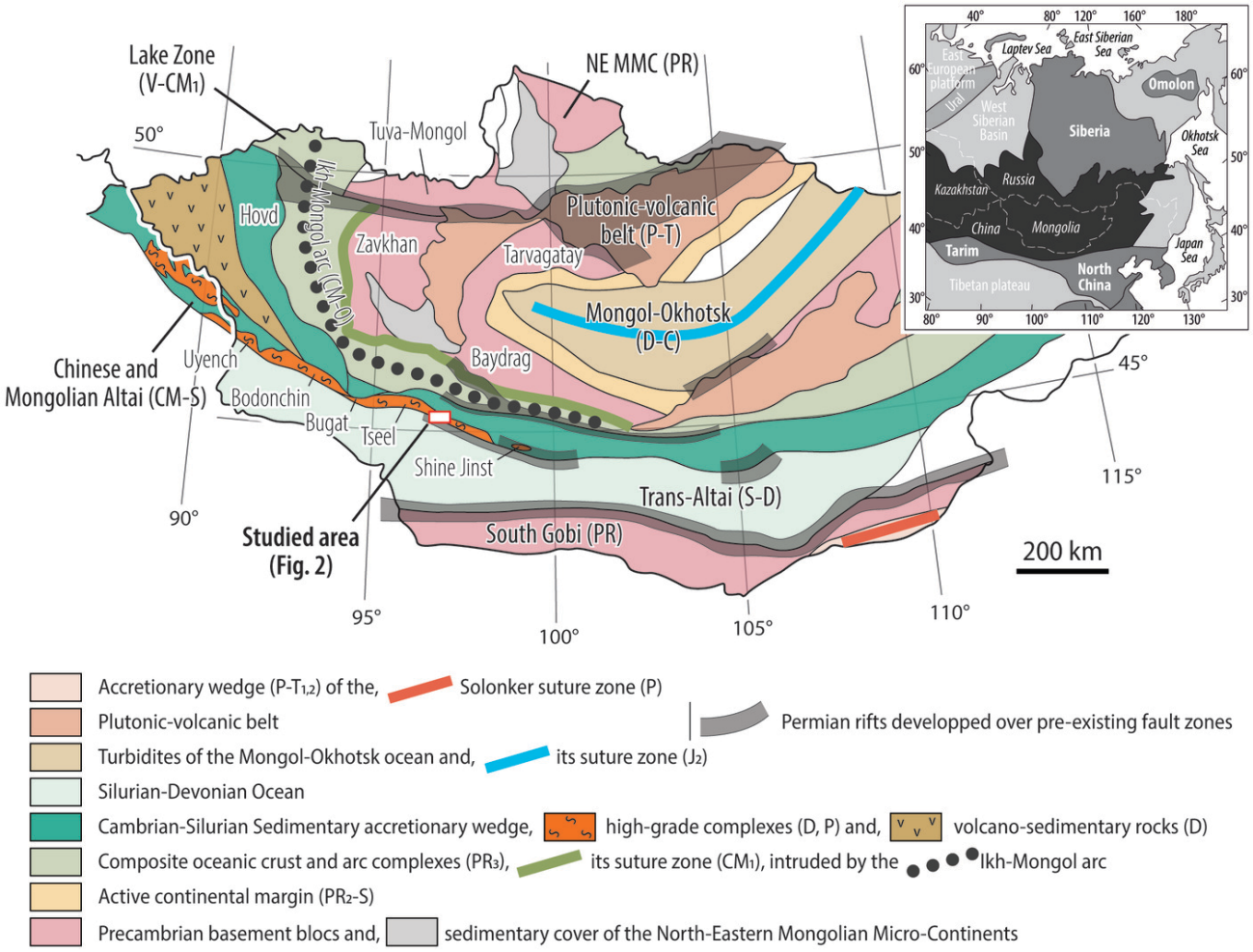


**Figure 1. Tectonic map of the Mongolian and Chinese Altai modified after Badarch et al. (2002) and Parfenov et al. (2003). The high-grade complexes and Devonian volcano-sedimentary rocks of the Mongolian Altai correspond to "Metamorphic rocks of uncertain affinity" and "Backarc/forearc basin" of Badarch et al. (2002), respectively. Position of the high-grade complexes of the Chinese Altai after Jiang et al. (2016). Approximate location of the Permian rift zones after Kovalenko and Chernov (2008). The inset shows the main geological blocks in NE Asia. From darker to lighter tones: Central Asian Orogenic Belt; Cratons; Ural orogenic belt, Mesozoic and Cenozoic belts.**

## 2.2. Geology of the Mongolian Altai

The Mongolian Altai exposes northern low- to medium-grade and southern high-grade metasedimentary units (Badarch et al., 2002). Similar U-Pb age patterns and Hf isotopic compositions of zircons from both units indicate a common origin of the sedimentary sequences (e.g., Jiang et al., 2011, 2017). The main constituent is a late Cambrian to late Ordovician – early Silurian immature sediment mixed with volcanogenic material (Buriánek et al., 2022). The whole package is interpreted as the erosion product of the Cambrian-Ordovician Ikh-Mongol Arc (*sensu* Janoušek et al., 2018) and its Precambrian basement, deposited in a fore-arc basin and referred to as the Altai Accretionary Wedge (AAW; Jiang et al., 2017; Soejono et al., 2017).

Metamorphism of the AAW grades from greenschist to amphibolite facies (Burenjargal et al., 2014; Jiang et al., 2012; Kozakov et al., 2009; Nakano et al., 2015) with local granulite (Kozakov, 2002). The dominant metamorphic field gradient involves chlorite, biotite, garnet, staurolite, kyanite, and sillimanite-migmatite zones and defines a Barrovian-type metamorphic sequence (Jiang et al., 2015; Kozakov et al., 2011, 2019). Minerals of the Buchan-type metamorphism, cordierite, andalusite, and sillimanite are also widespread in migmatite and paragneiss (Broussolle et al., 2015; Burenjargal et al., 2014; Jiang et al., 2015; Nakano et al., 2014). Overprint relationships are common, and the relative chronology is debated (e.g., Burenjargal et al., 2012; Sukhorukov et al., 2016). Yet, a review of available geochronological data from metamorphic rocks points to a polycyclic metamorphism ultimately controlled by the retreating and advancing mode of the subducting slab (Aguilar et al., 2024).

A first late Ordovician Barrovian metamorphism (Soejono et al., 2021) results from thickening of the sedimentary wedge (Buriánek et al., 2022). It coincides with the emplacement of minor late Ordovician granitoids in the Gobi Altai (*ca.* 445 Ma; Hanžl et al., 2024).

The main thermal event occurred in the Devonian, when sillimanite-migmatite (Jiang et al., 2012) and two-pyroxene granulites (e.g., Kozakov, 2002) are temporally associated with abundant mafic intrusions (Bibikova, 1992; Kozakov et al., 2019) and large granitic plutons (Burenjargal et al., 2012; Cai et al., 2015; Soejono et al., 2016). The sedimentary record varies laterally from marine proximal conglomerate and sandstone (Gibson et al., 2013) to distal marine flysch-type sediments associated with abundant mafic volcanism (Soejono et al., 2018). This event, favoured by lithospheric thinning, turned the accretionary wedge into a typical, vertically stratified continental crust (de Hoÿm de Marien et al., 2025; Hanžl et al., 2016; Jiang et al., 2016).

Late Devonian to early Carboniferous times are related to a slowdown of the magmatic activity (Buriánek et al., 2022). Petrological studies in the southern high-grade unit document isothermal pressure increase (Sukhorukov et al., 2016) and anticlockwise *P–T* paths (Nakano et al., 2015). In the northern unit, upright folding of the Devonian subhorizontal foliation points to the compressional nature of the Carboniferous event (Broussolle et al., 2015; Lehmann et al., 2017).

Permian times correspond to another major thermal event. It is documented by metamorphic ages from gneiss (Burenjargal et al., 2014; Nakano et al., 2014, 2015) and migmatite (Kröner et al., 2010). Supracrustal continental rifts (Buriánek et al., 2012; Hanžl & Aichler, 2007; Kröner et al., 2010) and migmatite domes in the high-grade domains (Lexa et al., 2025; Sukhbaatar et al., 2022) indicate an extensional setting. This extension was not limited to the Mongolian Altai as rift zones are superposed over most previous terrane boundaries in Mongolia (fig. 1; Kovalenko & Chernov, 2008). A summary of the data from magmatic rocks by Kozlovsky et al. (2015) further confirms the scale of the event, documented by widespread alkaline granite plutons and bimodal volcanics everywhere in the CAOB. Yet, the Permian tectonics is not well understood. On the one hand, the scale of the magmatism suggests a relation with the distant Tarim plume or to post-accretionary slab breakoff (Kozlovsky et al., 2015). On the other hand, geochemical studies of magmatic rocks from the Trans-Altai zone identified magmatic affinities typical of supra-subduction settings, characteristic of accretionary orogens (Hanžl et al., 2023).

Finally, a late Permian to Triassic N-S compressional event produced km-scale WNW-ESE trending upright folds and cleavage fronts reworking all the previous structures (Broussolle et al., 2019; Jiang et al., 2015; Lehmann et al., 2010; Sukhbaatar et al., 2022).

### 2.3. Field geology and sampling strategy

The studied section (fig. 1) follows the valley of the Gegetin-Gol River (fig. 2). Three domains distinguished by increasing metamorphic grade and abundance of magmatic rocks (fig. 2A) occur from north to south: the Northern Domain consists of low-grade metasediments (fig. 3A), the Central Domain of medium-grade metasediments intruded by abundant granitoid and minor diorite dikes (figs. 3C and 4A), and the Southern Domain of migmatites with abundant felsic and mafic metaigneous rocks (fig. 5A and E). The section is bounded to the south by the Trans-Altai shear zone.

The Northern Domain is dominantly composed of low-grade clastic sediments with beds of limestones, tuffs, and rhyolites. Zircon U-Pb data from a siltstone (460 Ma; Kröner et al., 2010) intruded by late Ordovician granitoids (*ca.* 455–445 Ma; Hanžl et al., 2024) constrain the sediment deposition to the Ordovician. The original sedimentary bedding is defined by a subhorizontal compositional layering ($S_{bed}$; fig. 3A). A spaced cleavage has a gentle and variable dip ($S_{cleav}$). To the south, a penetrative schistosity ($S_{schist}$) appears. It is folded by asymmetric folds with horizontal axes and axial planes gently dipping to the north ($F_{rec}$; fig. 3B). Further south, a sharp transition (~ 1 km) from phyllite to micaschist is marked by a grain-size increase.

The Central Domain is composed of micaschist and gneiss with amphibolite boudins and variably deformed granitoid and diorite dikes. In detail, a belt of micaschist and another of sillimanite-gneiss occur in the north and south, respectively. The contacts between the micaschist and intrusive granitoid sills (fig. 3C) are moderately dipping to the NE, parallel with the macroscopic schistosity ($S_{main}$). Relics of an older foliation are not observed in the micaschist, but low-strain domains in competent amphibolite display isoclinal folds ($F_{iso}$; fig. 3E) of an earlier fabric ($S_{relic}$). A strong grain-size reduction in the amphibolite ($S_{main\text{-}SZ}$) results in total transposition of the older foliation into a new mylonitic foliation (fig. 3E). Zircon U–Pb data from a foliated granite indicate that the deformation is younger than *ca.* 295 Ma (Kröner et al., 2010). The main foliation is locally crosscut by undeformed diorite dikes (fig. 3F).

In the micaschist, three metamorphic stages were distinguished (Sukhorukov et al., 2016). An initial LP-HT stage at *ca.* 550–575 °C, 3–4 kbar, was followed by a MP-MT event at *ca.* 540–575 °C, 6–8 kbar and a nearly isobaric increase of temperature to *ca.* 575–615 °C, 6–7.5 kbar. Based on microstructures, the same study concluded that staurolite related to the isobaric heating was post-tectonic. Our observations show that garnet and staurolite are typically mm-sized, and coarser cm-sized crystals occur in neck zones of boudinaged quartz-veins (fig. 3D), suggesting rather syn-tectonic growth with $S_{Main}$.

Further south occurs a sillimanite-gneiss (fig. 4B) containing folded leucosomes ($S_{relic\text{-}mig}$; fig. 4A) and layer-parallel granite sills (fig. 4C). Fine-grained sillimanite gneiss displays a rhythmic alternation of felsic and biotite-rich layers ($S_{main\text{-}SZ}$; fig. 4D). Abundant granitoid dikes are mostly parallel with the foliation ($S_{main}$) and locally crosscut the foliation. In some places the dikes are affected by recumbent folds ($F_{rec}$) within the foliation. The folds are strongly asymmetric and display subhorizontal hinges associated with subhorizontal to NE dipping axial planes (fig. 4E and F).

The Southern Domain is dominated by biotite-rich stromatic and nebulitic migmatites in the north (migmatite belt) and migmatitic orthogneiss (orthogneiss belt) in the

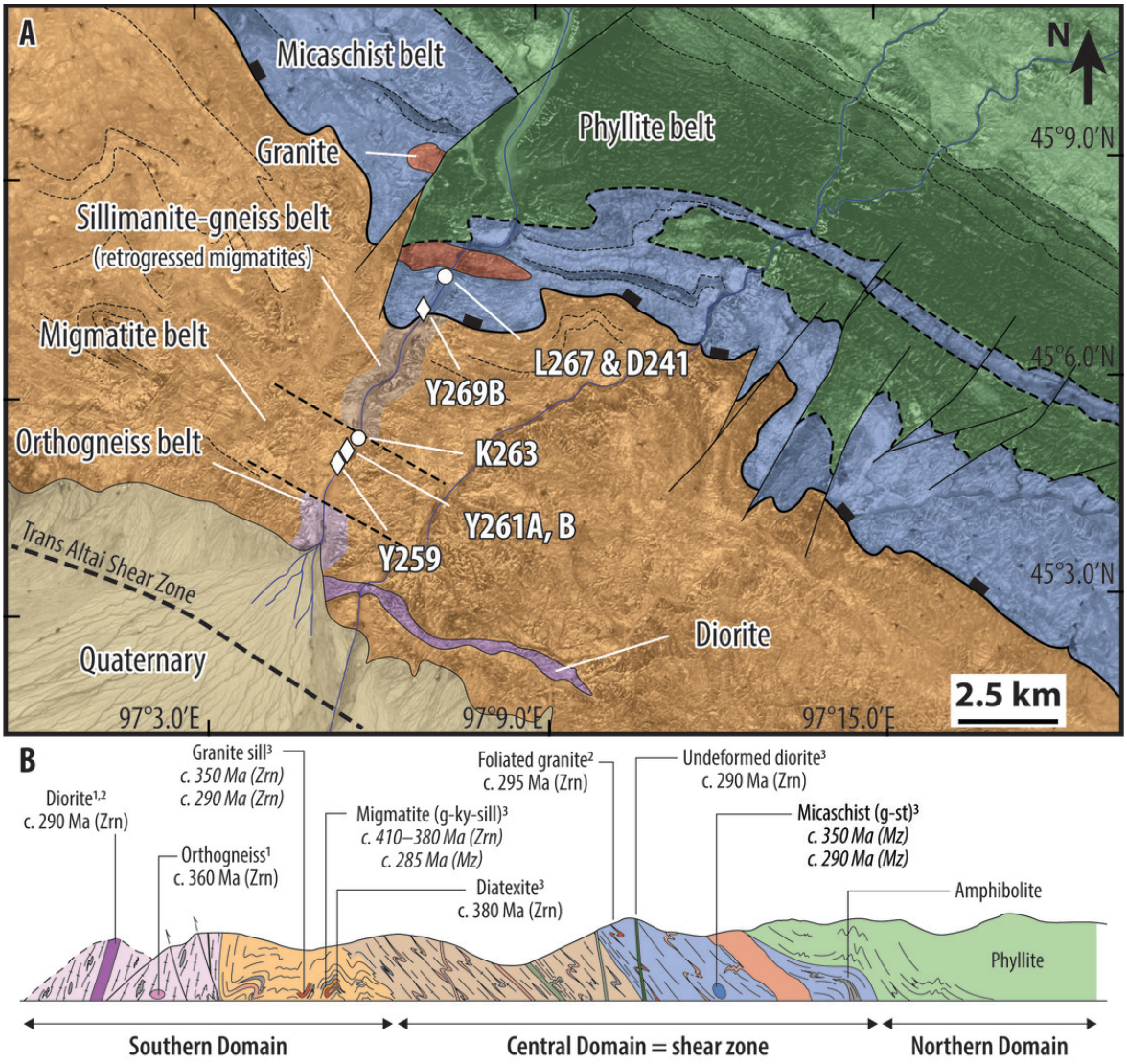


**Figure 2. Structural map and cross-section of the studied area. A) Map showing the main lithological groups recognized along the section and location of the samples. Note that details about the lithologies in the southern migmatitic domain are indicated along the studied valley, but their lateral continuity is uncertain. B) Cross section indicating the structural context of the dated samples and zircon U-Pb data from the literature. Magmatic ages are indicated in regular font and metamorphic ages in *italics*. Dated lithologies are highlighted and labeled above the profile; references: (1) Helo et al. (2006); (2) Kröner et al. (2010); (3) this study. The domains indicated below the profile were discriminated according to the principal lithologies and structures.**

south (fig. 2). Alternation of stromatic migmatite, nebulitic migmatite, amphibolite, orthogneiss and granitoid sills define a prominent lithological layering (fig. 5A). Sillimanite and garnet are common in stromatic migmatite (fig. 5B). The migmatitic foliation defined by an alternation of leucosome and mesosome ($S_{main\text{-}mig}$) is parallel with the lithological layering. The migmatitic fabric contains intrafolial isoclinal folds ($F_{iso\text{-}mig}$; fig. 5C and D) and is affected by two sets of later folds ($F_{up}$ and $F_{rec}$; fig. 5A).

The orthogneiss belt is composed of mesocratic metagranitoid associated with abundant amphibolite boudins. A migmatitic foliation ($S_{relic\text{-}mig}$; fig. 5E) is preserved in the amphibolite boudins. $S_{relic\text{-}mig}$ is oriented at high angle with the main foliation of the host migmatitic orthogneiss ($S_{main\text{-}mig}$; fig. 5E). The main fabric is folded by upright folds with steeply inclined axial planes and subhorizontal axes ($F_{up}$; fig. 5F). Zircon from a partially molten tonalite gneiss (*ca.* 385 Ma, U–Pb LA-ICP-MS; Kozakov et al., 2023) and from a granitic orthogneiss (*ca.* 360 Ma, Pb-Pb evaporation; Helo et al., 2006) document a Devonian thermal event. Another Permian thermal event is indicated by *ca.* 290 Ma zircon ages from a granodiorite (Pb-Pb evaporation; Helo et al., 2006) and a foliated diorite (SHRIMP U-Pb; Kröner et al., 2010).

We gathered metamorphic and magmatic samples from the micaschist belt of the Central Domain and the migmatite belt of the Southern Domain (fig. 2). In the Central Domain, a garnet-staurolite and a garnet-staurolite-kyanite micaschists L267B and D241C were sampled to constrain the metamorphic *P–T–t* evolution. An undeformed

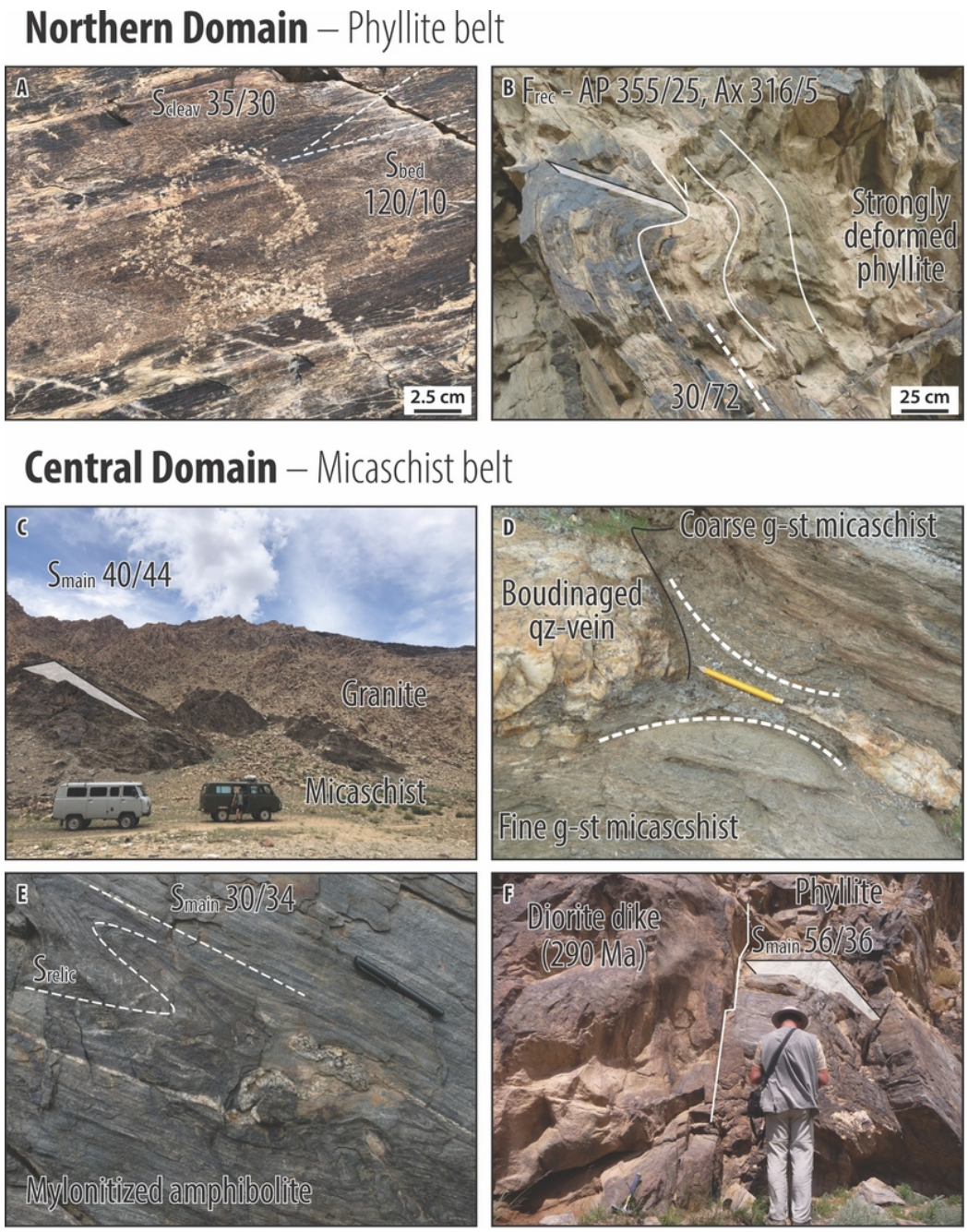


**Figure 3. Field photographs of the phyllite and micaschist belts. A) Sedimentary bedding and cleavage in phyllites. B) Passive fold in a strongly deformed phyllite close to the contact with the micaschist. C) Outcrop of the micaschists L267 and D241 in contact with a thick granite sheet. D) Increase of garnet and staurolite porphyroblast size in the neck zone of a boudinaged quartz vein. E) folded and transposed foliation in an amphibolite, the granitic vein shows a clear grain-size reduction. F) Diorite dike cutting across the main foliation of phyllite.**

diorite dike (Y269B) cutting across all the structures was taken to approximate the upper age limit of $S_{Main}$. In the Southern Domain, two garnet-kyanite-sillimanite migmatite samples, K263 and Y261B, a nebulitic migmatite (Y261A), and a tonalite sill (Y259) defining the main lithological layering were sampled for U-Pb monazite and zircon dating to document the age(s) of thermal events in the migmatite belt. The garnet-kyanite-sillimanite migmatite (K263) was selected for further petrological investigation to determine the *P–T* evolution of this domain.

## 3. METHODS

### 3.1. Mineral chemistry

Mineral analyses and compositional maps of garnet were performed with a Jeol JXA-8530F field emission gun Electron Probe MicroAnalyzer (EPMA) at the Institute of Petrology and Structural Geology of Charles University in Prague (Czech Republic). Quantitative analyses were performed with 15 kV accelerating voltage and 20 nA beam current,


**Figure 4. Field photographs of the sillimanite gneiss belt. A) Outcrop view of the abundant granitoid dikes in the gneiss. B) Close-up view of the gneiss showing the main foliation marked by biotite and abundant sillimanite needles; sillimanite is sometimes associated with quartz in discrete bands. C) Folded granitic vein in a deformed gneiss. D) Mylonitic foliation in the sillimanite gneiss. E) Folded granitoid dike in the sillimanite gneiss. F) Passive fold in the sillimanite gneiss.**

with 1 µm beam, except for feldspars and micas, which were analyzed with a beam defocused to 5 µm. Kα lines of the characteristic X-rays were used for the detection of all the elements except for Ba and Y, which were detected on Lα lines. A ZAF correction method was used for the correction of the matrix effects. Chemical maps of garnet were made at 15 kV, 70 nA, and 40 ms per pixel. $Al_2SiO_5$ polymorphs were discriminated at Charles University using the Electron Back Scattered Diffraction (EBSD) mode of a Scanning Electron Microscope (SEM) TESCAN Vega equipped with a detector NordlysNano, Oxford Instruments. Calculated mineral endmembers (expressed in mole %) and compositional variables are: almandine, Alm = Fe/(Fe+Mg+Ca+Mn); pyrope, Prp = Mg/(Fe+Mg+Ca+Mn); grossular, Grs = Ca/(Fe+Mg+Ca+Mn); spessartine, Sps = Mn/(Fe+Mg+Ca+Mn); anorthite, An = Ca/(Ca+Na+K); $X_{Fe}$ = Fe/(Fe+Mg), $X_{Na}$ = Na/(Ca+Na+K); and apfu: atom per formula unit. Chemical zoning is expressed from core to rim by the symbol: $X_{Core} \rightarrow X_{Rim}$. Representative mineral analyses are available as supplementary material (table S1).

## 3.2. Pseudosection modeling

Bulk chemical compositions were estimated at Charles University by scanning areas of thin sections using the Energy Dispersive Spectroscopy (EDS) mode of the SEM equipped with a detector X-Max 50 from Oxford Instruments.

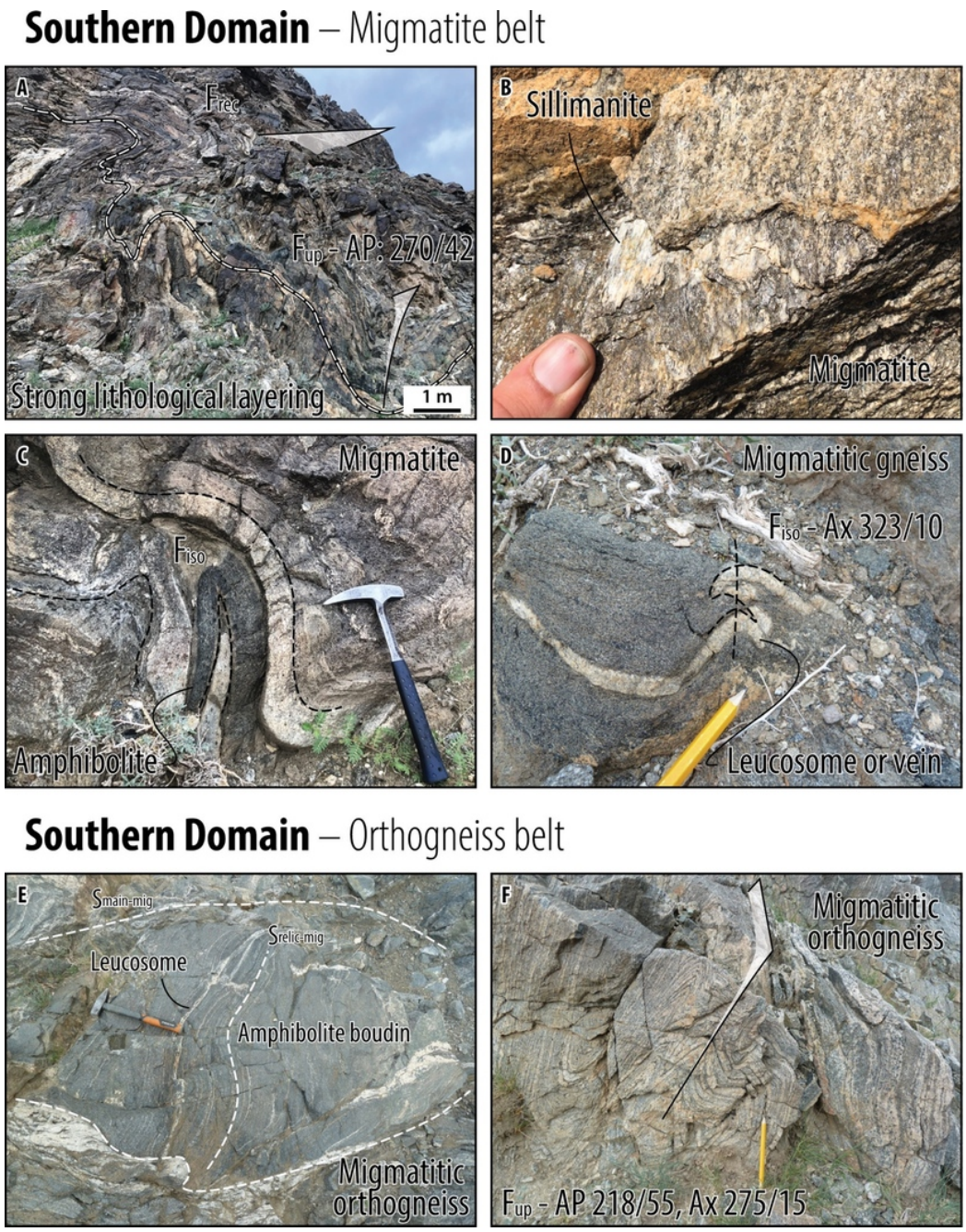


**Figure 5. Field pictures of the Southern Domain. A) folded lithological layering marked by migmatite, granitoids, and amphibolite. B) Sillimanite in migmatite. C) isoclinal fold hinge within the main lithological layering. D) Isoclinal fold in a leucosome or vein from a migmatitic gneiss. E) Amphibolite boudin containing leucosomes oblique with the migmatitic foliation of the enclosing orthogneiss. F) Upright folds in the migmatitic orthogneiss.**

Scanned zones (~90 to ~200 $mm^2$) evaluated to be representative of the composition of the equilibrium volume during the prograde metamorphism encompass the complete rock assemblages and the modelled garnet crystals (i.e., using compositional isopleths) in the pseudosections. Bulk compositions are indicated in mol% as insets in pseudosections. All the samples contain ilmenite and lack magnetite, suggesting a low amount of $Fe^{3+}$ (Connolly & Cesare, 1993); an arbitrary low amount of $Fe^{3+}$ (1 mol%) was set accordingly, effectively preventing magnetite in the models.

Pseudosections were calculated with THERMOCALC (Powell & Holland, 1988) version 3.5 (December 2020 upgrade), using the x-eos set for metapelites (White, Powell, Holland, et al., 2014, January 2022 update), in the system MnNCKFMASHTO. THERMOCALC was run through the *pypsbuilder* interface (Lexa, 2017). The dataset includes the models for chlorite (chl), chloritoid (ctd), cordierite (cd), garnet (g), ilmenite (ilm), melt, orthopyroxene (opx), sapphirine (spr), staurolite (st) from White, Powell, Holland et al. (2014); biotite (bi; White, Powell, & Johnson, 2014); epidote (ep; Holland & Powell, 2011); plagioclase (pl) and K-

feldspar (ksp; Holland et al., 2022); magnetite (mt; White et al., 2000) and spinel (spl; White et al., 2002). Effective bulk compositions were estimated using the *print bulk info* script of THERMOCALC, removing a single garnet composition estimated from the model. Melt loss in migmatite was accounted for using the *print bulk info* script by reincorporating a single melt batch at peak *P–T* conditions, i.e., coinciding with the maximum melt content along the inferred *P–T* path. Melt was reincorporated after the procedure described in Štípská et al. (2008), modified to fit the observed assemblage of the studied sample. Enough melt was reincorporated to reach water saturation at the solidus on a probable prograde *P–T* path, and further $H_2O$ was subsequently added to model the subsolidus evolution assuming water-saturated conditions.

### 3.3. Monazite U-Pb and trace element analyses

Before isotopic and trace element analyses, the monazite grains were identified in thin section using the Back Scattered Electron (BSE) mode of the SEM at Charles University. High-contrast BSE images of monazite grains with suitable size (> 20 µm) were acquired, and representative grains were then mapped for Y, Th, La, and U using the EPMA hosted at Charles University.

Monazite U-Pb isotopes and trace-elements analyses were performed *in situ* on a single spot and directly in thin section by Laser-Ablation Split stream inductively coupled plasma-mass Spectrometry (LASS) at the Department of Earth Science of the University of California in Santa Barbara (USA). The analyses were carried out using an 8 µm beam size with a 3 Hz repetition rate and ~1 J/cm$^2$ fluence. The data were corrected for U-Pb and Th-Pb fractionation and mass bias by standard bracketing with repeated measurements of the 44069 monazite (Aleinikoff et al., 2006) as U-Pb primary reference material and Trebilcock (Tomascak et al., 1996) as trace-element primary reference material. Details on the analytical procedure and data processing can be found in Kylander-Clark et al. (2013). Reference material data table, calculated ages, and the original data table can be found in table S2. Errors in the data tables are reported as 2SE. Secondary reference materials yield long-term reproducibility of ~2%, and as such, ages of monazite reported herein should be compared with those of other methods using a 2% uncertainty. To this end, age uncertainties reported in the text are presented by the 2SE internal uncertainty, followed by that propagated with the long-term 2SD (i.e., 2%) in brackets.

### 3.4. Zircon U-Pb dating

U-Pb isotopes of the mounted zircon crystals were measured using a Nu Plasma HR MC-ICP-MS, coupled with an ArF excimer 193 nm laser ablation system (Resolution M-50) at the Department of Earth Sciences, the University of Hong Kong (China), following the analytical procedure of Xia et al. (2011). The raw data were corrected for U-Pb and Th-Pb fractionation and mass bias by standard bracketing with repeated measurements of the GJ1 zircon (Jackson et al., 2004) as primary reference material. Raw data as well as the calculated data for both reference material and the dated samples can be found in table S3. Long-term reproducibility of secondary reference material also yields a long-term reproducibility of 2%. Accordingly, zircon dates reported in the text are also presented by the 2SE internal uncertainty, followed by that propagated with the long-term 2SD (i.e., 2%) in brackets.

### 3.5. Plot of the U-Pb data

U-Pb dates and diagrams were generated with IsoplotR (Vermeesch, 2018). External uncertainties related to the decay constants were propagated to the calculated dates. Zircon U-Pb data are mostly concordant; they were consequently plotted in Wetherill plots, and multi-grain concordia dates were calculated from the data points. Monazite U-Pb data are moderately discordant for two samples (L267 and D241), but discordance is correlated with 204 cps (count per second), and the data yield a single tie line between an isotopic Pb composition and a lower intercept in Tera-Wasserburg diagrams, indicating that the discordance is due to small amounts of common Pb. Lower intercept dates were calculated accordingly. When possible, discordia lines calculated in Tera Wasserburg plots were not anchored to a fixed $^{207}Pb/^{206}Pb$ value, and the isotopic $^{206}Pb/^{207}Pb$ composition indicated by the upper intercept was compared to the terrestrial Pb isotopes model of Stacey and Kramers (1975). Weighted Mean Average (WMA) dates were calculated using the dates corrected for the incorporation of common Pb when necessary (i.e., for positively discordant analyses); these are corrected assuming an upper intercept $^{207}Pb/^{206}Pb$ of Stacey and Kramers. The calculated Mean Square Weighted Deviates (MSWD) in U-Pb diagrams is given as $MSWD_{C+E}$, taking both concordance and equivalence into account (see Ludwig, 1998); or corresponds to the isochron fit and age homogeneity for lower intercept and WMA dates, respectively.

## 4. RESULTS

### 4.1. Petrography and mineral chemistry

#### *4.1.1. L267 garnet-staurolite-sillimanite and D241 garnet-staurolite-kyanite-sillimanite micaschists*

The micaschist samples display many petrographic similarities and are described together; the description stands for both samples, and differences are indicated in the text or parentheses. On the outcrop, the samples are fine-grained micaschists with small garnet (up to 1 mm) and staurolite (2–3 mm) wrapped in a penetrative foliation marked by a compositional layering. Under the microscope, L267 is composed of garnet (~5–10 %), staurolite (~5–10 %) and sillimanite (<1%), in a matrix of muscovite (~20%), biotite (~25%), plagioclase (~10 %) and quartz (~30 %), with accessory rutile, ilmenite, monazite, zircon and apatite. In contrast, D241 contains less staurolite (~2–3 %), contains kyanite (~1%), and more sillimanite (~3–5 %), while other minerals occur in similar proportions. The compositional layering is marked by an alternation of quartz-plagioclase-

and biotite-muscovite-dominated layers of comparable thickness (100–250 µm; fig. 6A, E).

In both samples, two garnet generations can be identified optically (fig. 6B, C, and H). Commonly, garnet 1 is euhedral (up to 450 µm) and separated from garnet 2 (up to 100 µm thick) by a so-called "mineral ring" about 20–50 µm in thickness. Sometimes, the two garnets are in crystallographic continuity through a transitional cloudy garnet containing numerous tiny (1–5 µm) inclusions (fig. 6B, D, and F). Garnet 1 contains ilmenite, quartz, and monazite inclusions (fig. 6C, H), and in addition, rutile also occurs in D241. The mineral ring contains biotite, quartz, ilmenite, apatite (fig. 6C, H), and rutile in L267. The cloudy garnet zone contains biotite, quartz, apatite inclusions, as well as chlorite in L267 (fig. 6D). Garnet is abundant in the matrix, flanked by quartz in pressure shadows. It is also included in staurolite, where garnet 2 displays sharp grain boundaries against staurolite (black arrows in fig. 6A, B, and F).

In L267, staurolite is xenoblastic but in sharp contact with the matrix minerals (white arrow in fig. 6A). Staurolite contains abundant inclusions of quartz with subordinate biotite and ilmenite, as well as garnet flanked by pressure shadows, all marking an internal fabric in continuity with the matrix foliation (fig. 6A). The external foliation, locally marked by sillimanite (fig. 6A), wraps around the garnet and staurolite porphyroblasts (fig. 6A and B). In D241, staurolite occurs as mm-sized anhedral crystals surrounded by an aggregate of biotite and quartz, all enclosed in a 500 µm thick corona of fibrolitic sillimanite (fig. 6E and F). Sillimanite aligns parallel with the matrix micas (fig. 6E) and contains rare anhedral crystals of kyanite (~200 µm; fig. 6G; identified by EBSD) and garnet (fig. 6G).

In both samples, garnet is zoned; several maps and profiles of continuous and discontinuous garnet crystals from the different textural positions were performed, and a representative garnet was selected for description in each sample (fig. 7A and D). The garnet selected in L267 has garnet 1 and garnet 2 in optical continuity, and the transition is marked by the cloudy appearance of the inner garnet 2. The garnet selected in D241 has a mineral ring between garnet 1 and garnet 2 (fig. 7B, E, and F). Based on sharp variations of grossular, garnet 1 (L267: Grs4 %; D241: Grs3–4 %) is further distinguished from an inner garnet 2 (L267: Grs7–10 %; D241: Grs8–10 %) and an outer garnet 2 (L267: Grs 4–5 %; D241: Grs3–5%). Across the three zones, garnet displays a rimward decrease of XFe and spessartine followed by slight increase at the edge of the crystal (core→rim→edge; L267: XFe0.90→0.84→0.85; Sps26→6→8 %; D241: XFe0.87→0.85→0.87; Sps25→7→9 %), associated with a rimward increase of pyrope and almandine followed by slight decrease at the very edge of garnet 2 (L267: Prp7→14→13 %; Alm62→75→74 %; D241: Prp10→14→11 %; Alm60→76→75 %). In both samples, the cloudy garnet has a composition similar to the inner garnet 2 from crystals with a mineral ring separating garnet 1 and garnet 2 (not shown).

The other minerals are fairly homogeneous across the thin section. Staurolite has XFe=77–78; Zn=0.015–0.025 apfu in L267 and XFe=75–78 and Zn=0.05–0.07 apfu in D241. Plagioclase is oligoclase (L267: An21–24 %; D241: An23–25 %). Muscovite contains a limited amount of paragonite (L267: XNa0.18–0.19; D241: XNa0.17–0.20) and low Si (L267: Si=3.05–3.07 apfu; D241: Si=3.06–3.09 apfu). Biotite has XFe=42–46 and Ti=0.11–0.22 apfu in L267; and XFe=46–47 and Ti=0.16–0.24 apfu in D241.

The following crystallisation sequence is deduced from petrographic and textural relations. Inclusion relationships indicate that garnet 1 crystallised with ilmenite in both samples, and additionally with rutile in D241. The inner garnet 2 crystallised in the presence of ilmenite, and also with rutile in D241 and chlorite in L267. Sharp grain contact between the outer garnet 2 and staurolite is interpreted as textural equilibrium, and therefore also as a proxy for chemical equilibrium. In D241, kyanite and staurolite occur in a similar position, suggesting a former chemical equilibrium. Staurolite preserves a foliation continuous with the matrix foliation that also wraps around staurolite crystals, indicating syntectonic growth. Sillimanite around subhedral to xenomorphic staurolite is interpreted as a replacement texture. Sillimanite oriented in the main foliation is also considered syntectonic.

#### *4.1.2. K263 – Garnet-kyanite-sillimanite migmatite*

On the outcrop, the rock is a medium-grained migmatite composed of biotite-garnet-sillimanite and quartz-feldspar aggregates. Sillimanite marks a mineral lineation on the foliation plane (fig. 8B). Under the microscope, the sample shows a variable proportion of dark- (20–40 %) and light-colored (60–80 %) minerals. It contains garnet, kyanite, sillimanite, biotite, plagioclase, quartz, chlorite, and accessory ilmenite, rutile, zircon, monazite, xenotime, and apatite. Garnet porphyroblasts (1–5 mm) display an anhedral inclusion-rich core and a thin (50–300 µm) discontinuous inclusion-free rim (fig. 8C and D). Small inclusions (5 µm, but up to 50 µm) in garnet core encompass quartz, plagioclase, biotite, ilmenite, rutile, chlorite, apatite, as well as minor zircon and monazite. Rutile and ilmenite in the garnet core occur close to each other, and they are randomly distributed (fig. 8E).

The matrix contains plagioclase, quartz, biotite, and minor sillimanite crystals. The crystal-size distribution of quartz, plagioclase and biotite is bimodal, with a majority of mm-sized crystals (~95 %), and minor small interstitial crystals (~5 %, ~100 µm in size; fig. 8F). The coarse plagioclase and quartz contain small round crystals of biotite or kyanite identified by EBSD (100–300 µm; fig. 8G), plagioclase also contains round quartz inclusions. Coarse biotite (up to 3 mm) from the matrix is associated with prismatic sillimanite (~100 µm; fig. 8B). Biotite and garnet are locally chloritized.

Garnet is zoned (fig. 8C and G). From core to rim, XFe, spessartine, and grossular contents decrease, except next to the very edge, where the inverse trend of XFe and spessartine is observed (XFe85→75→81; Sps19→8→18 %; Grs11→5→5 %). Pyrope and almandine increase from core to rim and decrease at the very edge (Prp11→21→15 %; Alm58→65→62 %). The coarse matrix plagioclase displays increasing anorthite content from core to rim (An18→32

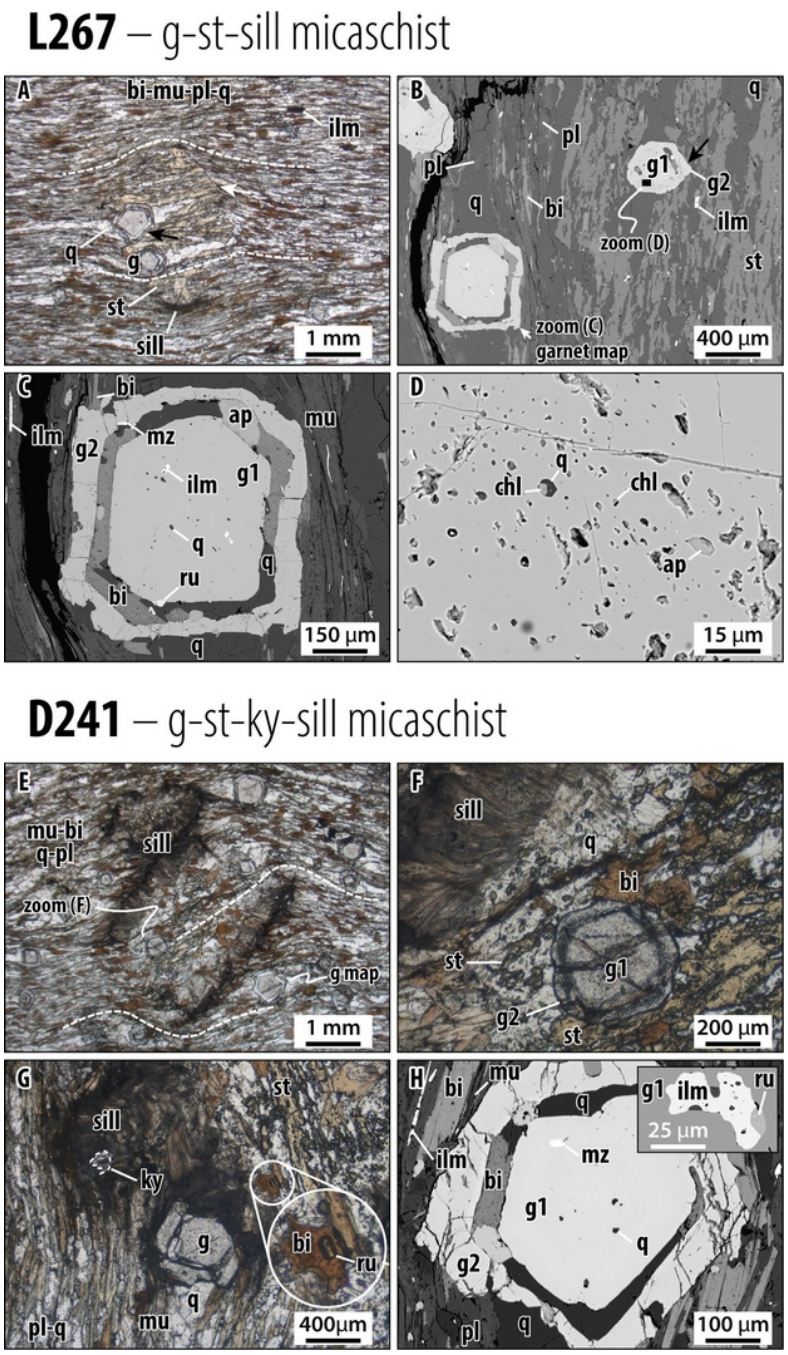


**Figure 6. Photomicrograph and back-scattered electron (BSE) images of the main textural features in the micaschists. L267 – A) Staurolite porphyroblast wrapped by the main foliation. Staurolite contains garnet inclusions and inclusion trails in continuity with the matrix. Staurolite has franc crystal faces against garnet (black arrow) and quartz (white arrow). Scarce sillimanite is seen in the vicinity of staurolite. B) Inclusions of garnet, ilmenite, and quartz in staurolite. Quartz inclusions are parallel to the matrix fabric. C) Garnet with a ring of coarse inclusions. Ilmenite in garnet 1 and the matrix, and rutile in the ring of coarse inclusions. D) Small inclusions of chlorite in the transitional cloudy zone marking the contact between garnet 1 and garnet 2. D241 – E) Xenomorphic staurolite surrounded by a spaced corona of fibrolitic sillimanite. The matrix fabric wraps around garnet, flanked by quartz in pressure shadows and the rotated xenomorphic staurolite porphyroblasts. Sillimanite is radially disposed around staurolite and at a high angle to the matrix fabric. F) Garnet in contact with staurolite relic. The transition between garnet 1 and garnet 2 is marked optically by a cloudy zone in garnet. Garnet 2 shares a franc crystal face with staurolite. G) Xenomorphic garnet and kyanite in sillimanite corona around staurolite. The zoom (white circle) shows rutile included in biotite next to staurolite. H) Garnet 1 and garnet 2 are separated by a ring of coarse inclusions. The inset shows anhedral inclusions of ilmenite and rutile in garnet 1.**

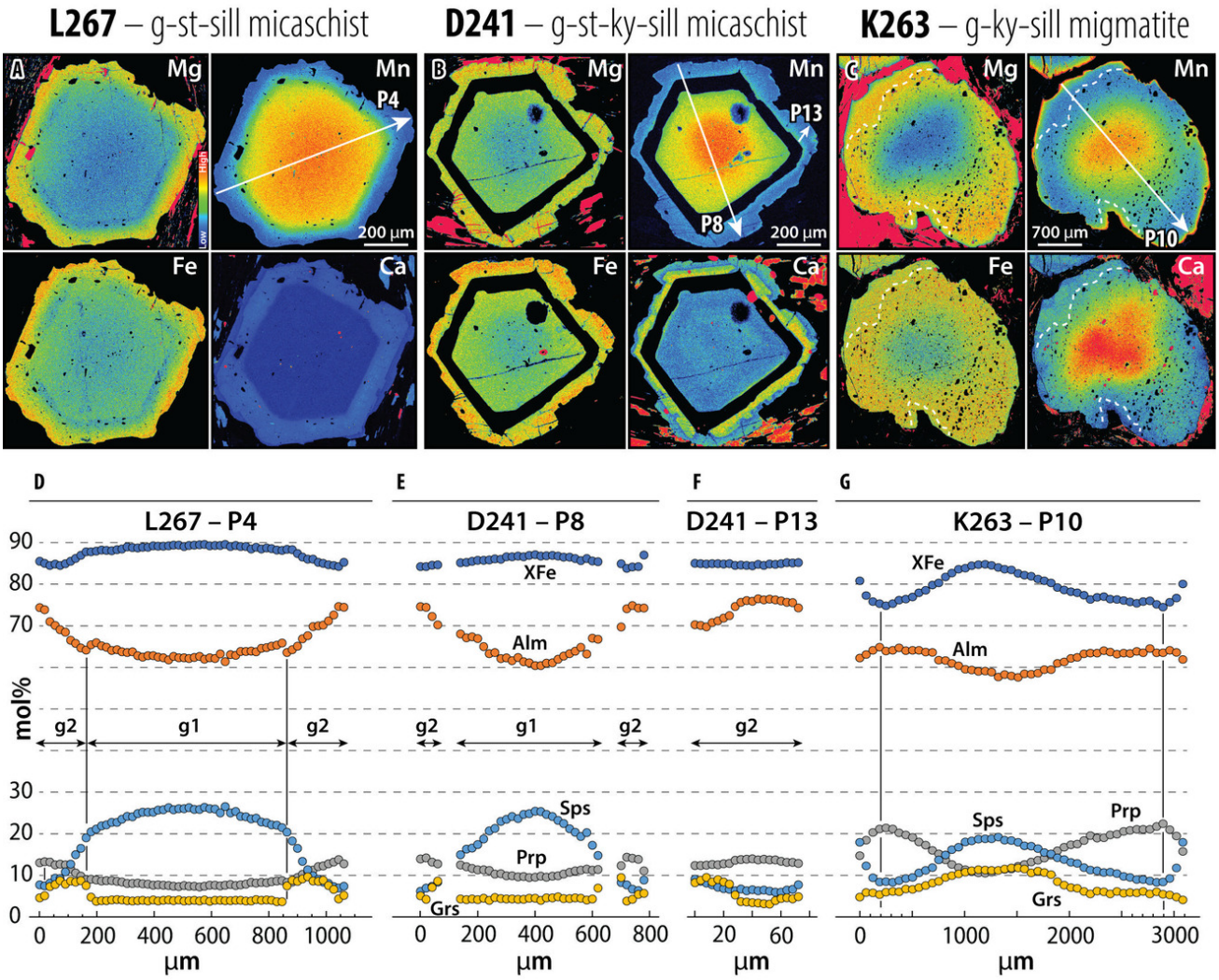


**Figure 7. X-ray maps (A–C) and chemical zoning profile (D–G) in garnets. The position and orientation of the profiles are shown on the X-ray maps.**

%), the small interstitial crystals compare to the rim composition (An28–29 %), and the most calcic crystals (An36 %) occur in garnet. Biotite in garnet shows lower XFe (32–39) and Ti (0.20–0.23 apfu) than most matrix crystals (XFe44–50; Ti0.26–0.36 apfu).

The petrographic features are interpreted in terms of the following crystallisation sequence. Inclusion relationships indicate that garnet core crystallised in the assemblage quartz, plagioclase, biotite, ilmenite, and rutile. Chlorite included in garnet could be primary or formed during retrogression. The xenomorphic shape of the garnet core possibly indicates a period of resorption. The garnet rim and the matrix assemblage represent later crystallisation events. Kyanite, preserved as inclusions, and sillimanite, ubiquitous in the matrix, belong to different metamorphic stages. Assigning rutile and ilmenite from the matrix is uncertain, but metastable rutile could be preserved from the kyanite-bearing stage. Small interstitial quartz, plagioclase, and biotite are interpreted as crystallised from a melt. Accordingly, we infer that garnet rim, kyanite, and rutile are part of the peak pressure assemblage, while sillimanite and ilmenite belong to the assemblage of a high-temperature overprint. Both stages potentially occurred at suprasolidus conditions. Chlorite after biotite and garnet represents later retrogression.

## 4.2. Phase equilibria modeling

### *4.2.1. L267 – garnet-staurolite-sillimanite micaschist*

The pseudosection shown in figure 9 was constructed to model the conditions of garnet 1 growth. The observed assemblage, garnet 1, ilmenite, and quartz, is compatible with the modelled field g-bi-chl-mu-ilm. Modelled compositional isopleths for the garnet 1 core (Sps26, Alm62, Grs4) overlap around 4–5 kbar, 525–550 °C, and those for the garnet 1 rim (Sps20, Alm64–65, Grs4–6) around 5–6 kbar, 550–575 °C, indicating a prograde path within the modelled g-bi-chl-mu-ilm field.

The composition of garnet 1 modelled at 5 kbar and 550 °C was used to determine a fractionated composition to construct the pseudosection in figure 10 and model garnet 2 growth. The topology of the new pseudosection is comparable to the unfractionated one, except for the signifi-

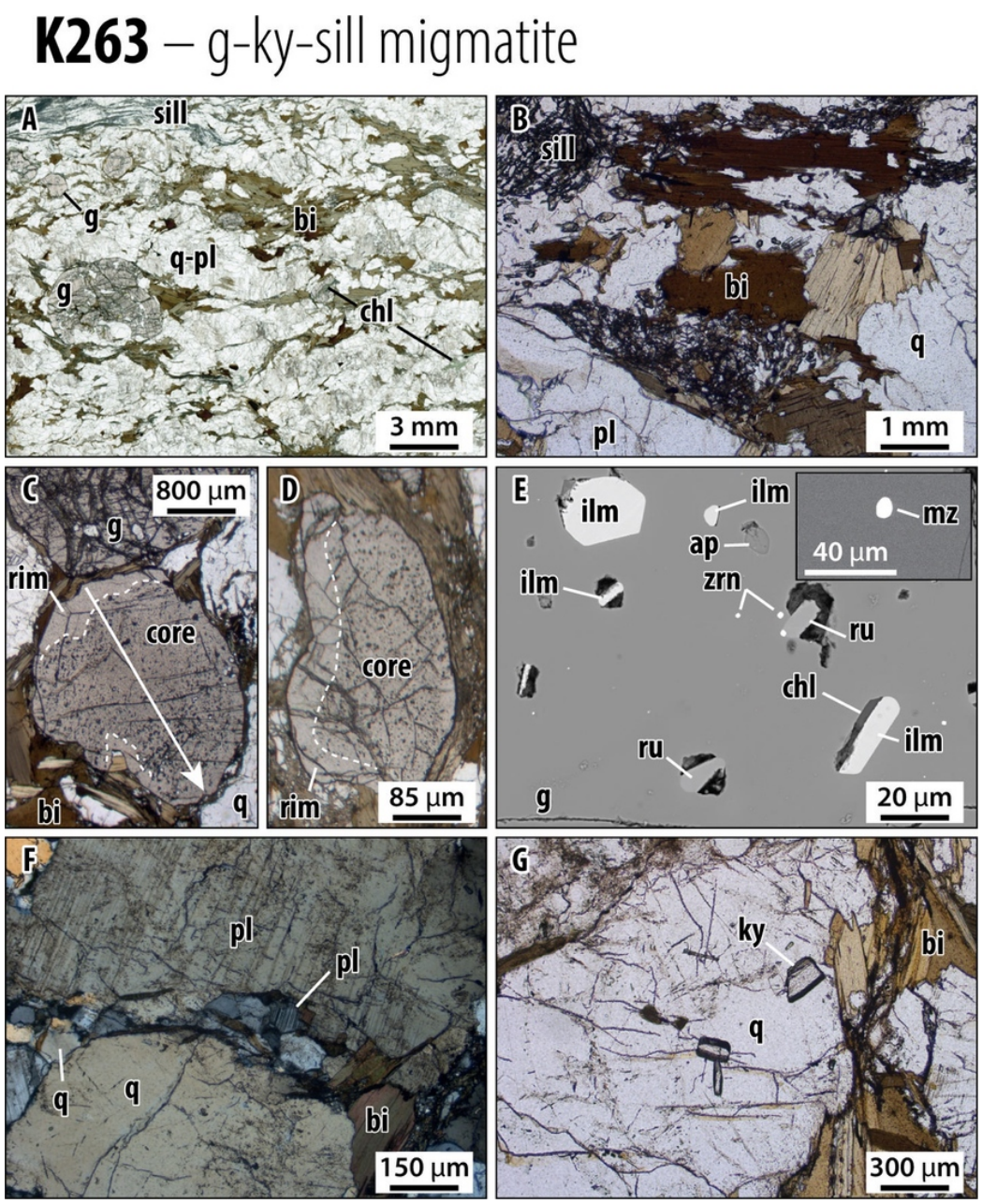


**Figure 8. Photomicrographs and BSE images of the main textural features in the migmatite. A) Matrix assemblage of garnet-sillimanite-biotite-quartz-plagioclase. Sillimanite forms planar segregations associated with quartz, and chlorite is sometimes present after biotite. B) Sillimanite is associated with biotite in the melanosome. C-D) Fine-grained inclusions in garnet cores and inclusion-free rims. E) Inclusions of rutile and ilmenite, sometimes associated with chlorite, in the garnet core. The inset shows the typical small size of monazite in garnet. F) Fine-grained interstitial crystals of quartz-plagioclase-biotite in between coarse quartz and plagioclase. G) Anhedral inclusions of kyanite in quartz from the leucosome.**

cantly reduced stability field of garnet toward higher pressure, above 4.5–7 kbar.

The observed assemblage of inner garnet 2, chlorite, biotite, quartz, rutile, and ilmenite is fully reproduced, together with matrix plagioclase, in the field g-bi-chl-pl-ilm-ru (label 12 in fig. 10) modelled at 6–7.5 kbar, 525–575 °C. The partial assemblage of outer garnet 2, staurolite, and rutile is reproduced at higher temperature in the field g-st-bi-pl-ru, at 600–675 °C and 6.5–8.5 kbar. The compositional isopleths for the inner (Sps11–20, Alm64–72, Grs7–10) and outer (Sps6, Alm75, Grs4–5) garnet 2 intersect in the fields g-bi-chl-pl-ilm-ru and g-st-bi-pl-ru, respectively, suggesting a roughly isobaric prograde *P–T* path.

Sillimanite and abundant ilmenite of the matrix are reproduced in the field g-sill-bi-pl-ilm (label 1 in fig. 10A) below 6.5 kbar and at 625–675 °C. The modelled change in garnet composition from the field g-st-bi-pl-ru to g-sill-bi-pl-ilm is consistent with the slight increase of spessartine and decrease of almandine observed at the edge of the outer garnet 2 crystals. Hence, the sillimanite overprint indicates a decompression.

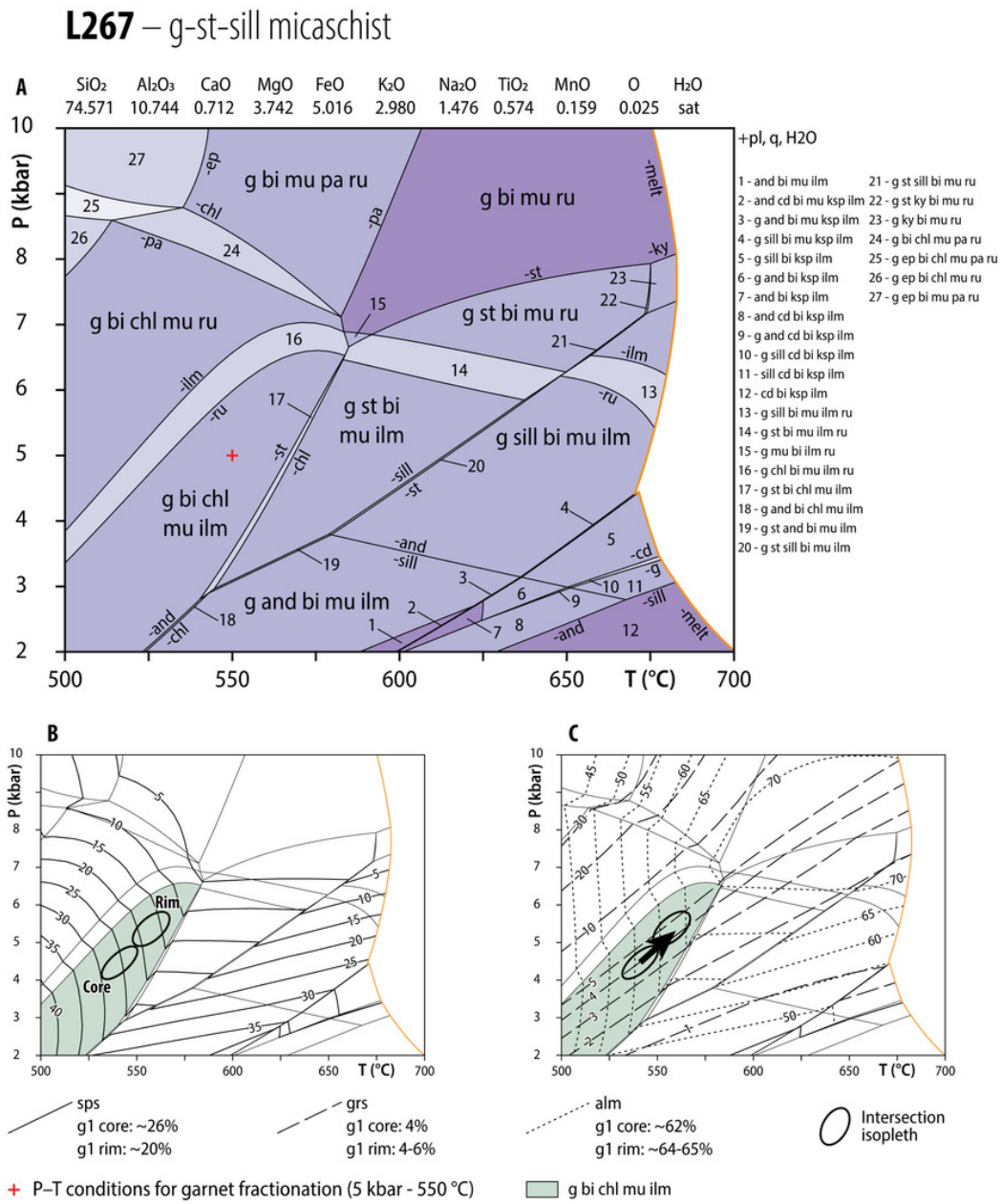


**Figure 9. A) *P–T* pseudosection constructed for the SEM-measured bulk composition of the sample L267. B–C) compositional isopleths for garnet.**

*4.2.2. D241 – Garnet-staurolite-kyanite-sillimanite micaschist*

A pseudosection was constructed to model the growth of garnet 1 (fig. 11). The observed assemblage garnet 1, biotite, quartz, ilmenite and rare (i.e., one) rutile is reproduced in the field g-bi-chl-mu-ilm-ru (label 20 in fig. 11). However, the modelled compositional isopleths for the measured composition of garnet 1 core (Sps25, Alm60, Grs3–4) and rim (Sps15, Alm68, Grs4–7) both intersect in the modelled field g-bi-chl-mu-ilm, i.e., at 3–4 kbar, 525–550 °C and 5–6 kbar, 550–575 °C, respectively; far from the ilmenite-rutile-bearing fields. Rutile may be of a detrital origin or formed at lower *P–T* conditions at greenschist facies, as suggested by the low temperature position of the ilm-ru transition (field labeled 20 in fig. 11); thus, rutile may not be characteristic of the assemblage stable with garnet 1. In such a case, the pseudosection points to a prograde growth of garnet 1 from 3–4 kbar, 525–550 °C to 5–6 kbar, 550–575 °C.

The pseudosection presented in figure 12 was constructed for a fractionated bulk composition using the modelled composition of garnet 1 at 5 kbar and 560 °C (fig. 11). In the fractionated pseudosection, the garnet stability field is significantly reduced above >5–7 kbar. The isopleths for the inner garnet 2 (Sps7–9, Alm70–72, Grs8–10) intersect in the field g-bi-chl-ilm around 7 kbar, 570 °C, which is compatible with the observed assemblage of inner garnet 2, biotite, ilmenite, plagioclase, and quartz, despite chlorite not observed in this sample. The inferred assemblage garnet-staurolite-kyanite is modelled in a narrow temperature window around 675 °C and between 7 and 9 kbar in the

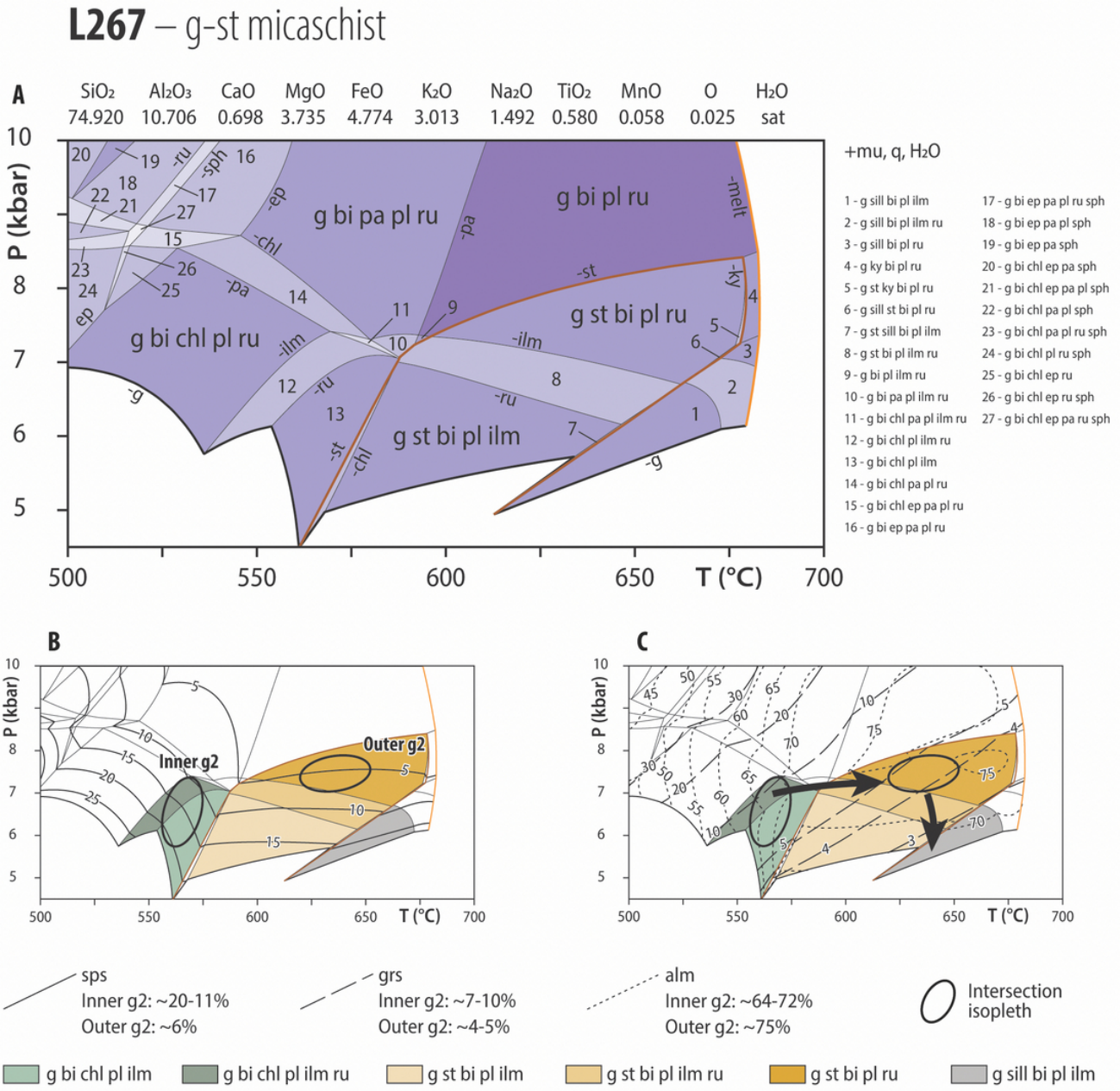


**Figure 10. A) *P–T* pseudosection constructed for the calculated composition of L267 accounting for garnet 1 fractionation. B–C) compositional isopleths for garnet.**

field g-st-ky-bi-ru (labeled 5 in fig. 12). The isopleths for the outer garnet 2 (Sps6–8, Alm74–76, Grs3–6) intersect in the field g-st-ky-bi-ru around 7–8 kbar, 675 °C in agreement with the inferred and calculated assemblages. Hence, garnet 2 growth is modelled along a roughly isobaric heating.

Sillimanite is modelled at 5–7 kbar and 625–680 °C. The observed local resorption of garnet in the vicinity of sillimanite may be accounted for by the modelled decrease of garnet mode (not shown) from the kyanite to the sillimanite stability fields. Similarly, the increase of spessartine and decrease of almandine contents at the edge of garnet 2 can be explained by the trend of garnet compositional isopleths during such decompression.

*4.2.3. K263 – Garnet-kyanite-sillimanite migmatite*

A pseudosection for K263 was constructed using the measured bulk composition (fig. 13). According to the absence of textural evidence for retrograde back-reactions such as biotite replacement of garnet (e.g., Waters, 2001) or muscovite in the rock assemblage (e.g., Štípská et al., 2008), most of the melt must have been extracted before cooling below the solidus. Accordingly, $H_2O$ was set to reproduce $H_2O$-undersaturated conditions when the rock crossed the solidus according to a TX($H_2O$) pseudosection (not shown). The possible range of $H_2O$ content is bracketed by the presence of K-feldspar (conspicuously absent in thin section) occurring at subsolidus conditions below 3.85 mol% of $H_2O$, and by the saturation of the rock with an aqueous fluid above 4.20 mol% of $H_2O$. This defines a narrow range of

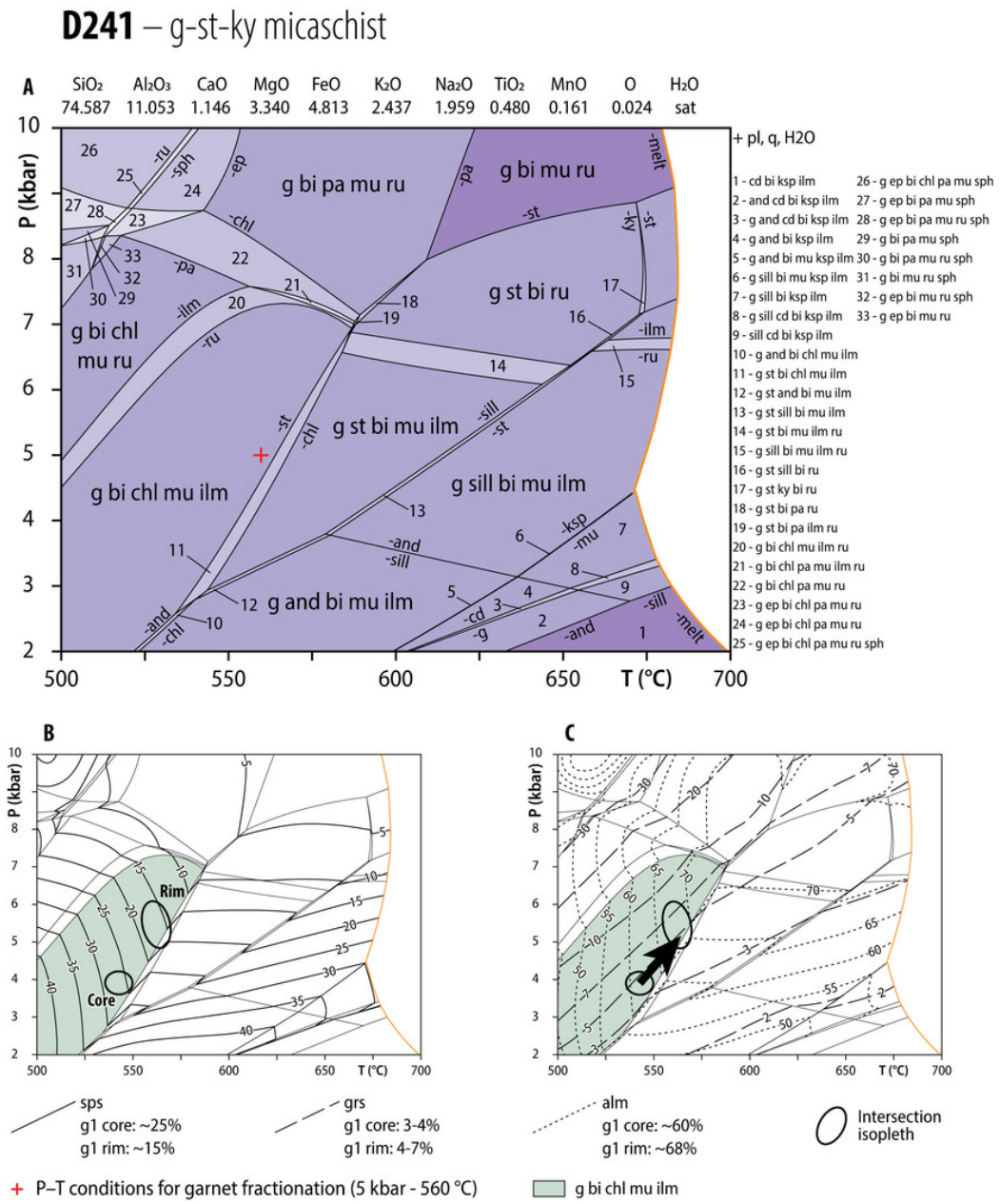


**Figure 11. A) *P–T* pseudosection constructed for the SEM-measured bulk composition of the sample D241. B–C) compositional isopleths for garnet.**

possible $H_2O$ content, and we used the value of 4.05 mol% for the calculation of the pseudosection.

The observed assemblage garnet-kyanite-rutile-biotite-plagioclase-quartz is best correlated to the field melt-g-ky-bi-ksp-ru (label 10 in fig. 13) at 8–10 kbar, 750–775 °C. Compositional isopleths for spessartine, almandine, and grossular for the spessartine-poor inner rim of garnet (Sps8, Grs5, Alm65) also intersect this field. K-feldspar, modelled in low proportion (<5%, not shown), is lacking in the observed assemblage, which could be explained by K-feldspar breakdown during decompression above the solidus. The assemblage sillimanite-ilmenite-rutile observed in the matrix is modelled in the very narrow fields g-sill-bi-ilm-ru±melt (labeled 17 & 18 in fig. 13). It is therefore unlikely that the rock equilibrated in these fields. Rutile is most likely a metastable remnant of the kyanite-bearing assemblage. Hence, sillimanite most likely documents an intermediate pressure overprint in the field melt-g-sill-bi-ilm around 5–6 kbar and 700–775 °C. The isopleths for garnet rim (Grs4, Alm61–63, Sps15–20) do not precisely intersect in the pseudosection, but the high spessartine content of garnet rim suggests significant cooling in agreement with chlorite observed in garnet fractures (not modelled).

An effective bulk composition was calculated, following a melt reincorporation procedure (see Methods), to assess the prograde, subsolidus *P–T* conditions of the rock (fig. 14). Garnet core contains the assemblage chlorite-biotite-plagioclase-quartz-ilmenite-rutile reproduced in the field g-bi-chl-mu-ru-ilm. Even if chlorite possibly formed during the retrograde *P–T* path, the isopleths corresponding to the measured composition of the garnet core (Sps19, Alm58,

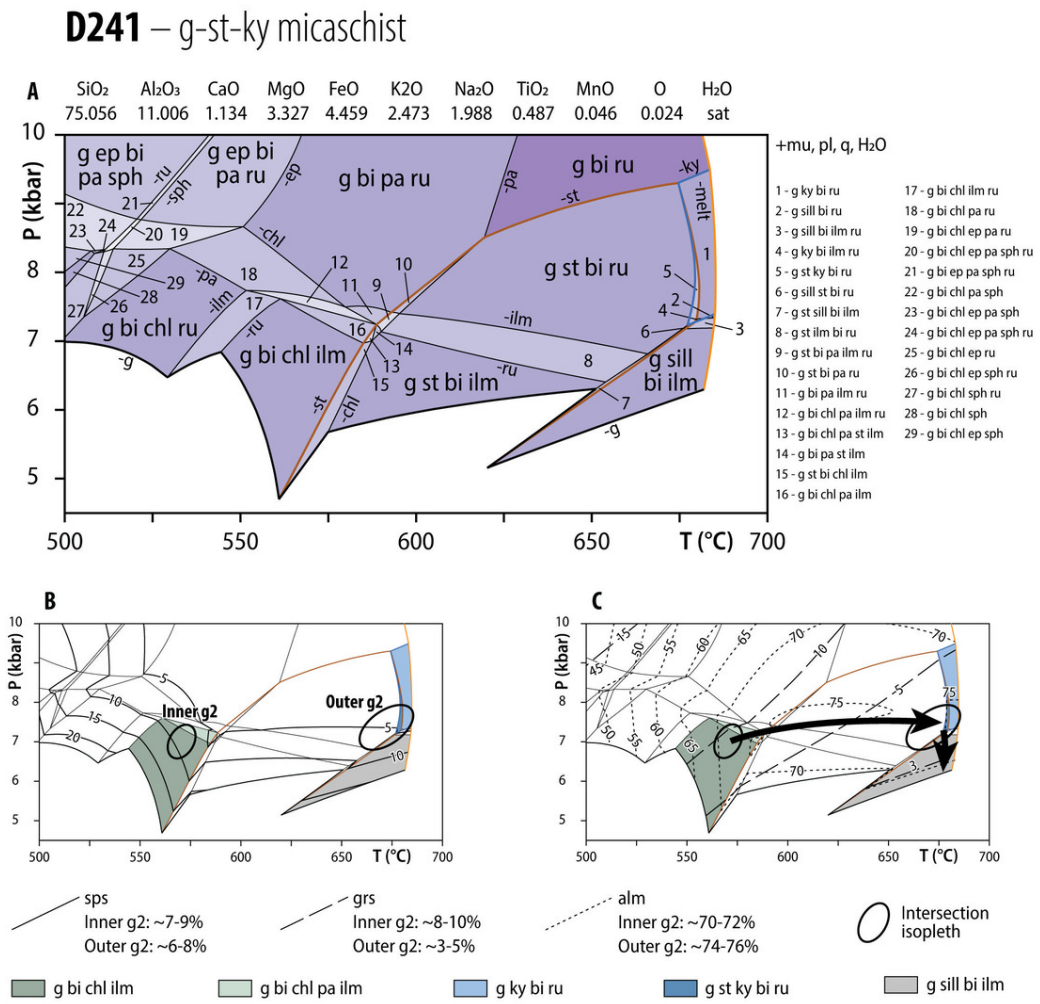


**Figure 12. A) *P–T* pseudosection constructed for the calculated composition of D241 accounting for garnet 1 fractionation. B–C) compositional isopleths for garnet.**

Grs11) closely overlap this field and the neighbouring field g-bi-chl-mu-ru between 550–575 °C, 5–6 kbar. The possible resorption of garnet core before garnet rim growth would imply a metamorphic evolution more complicated than a single prograde metamorphism, and the *P–T* path is thus indicated as a dotted line in the figure.

## 4.3. Monazite petrography, geochronology, and trace-element data

### *4.3.1. L267 – garnet-staurolite-sillimanite micaschist*

Monazite was carefully examined in thin section and crystals with suitable size (≥10 µm) for LASS analyses have been identified in garnet 1, fully or partially included in garnet 2, epitaxial on micas, fully included in matrix quartz, and staurolite (fig. 15). Compositional maps of the largest crystals reveal a patchy zoning (fig. 15H). Eighty-five spots were measured in 52 monazite crystals from various textural positions. Only one spot could be analyzed in garnet 1.

Textural control on the distribution of trace-elements in monazite crystals was investigated in REE-spider plots; $Gd_N/Yb_N$-vs-date and Y-vs-date binary plots (fig. 16A to C). Monazite included in garnet 1 shows a moderate slope of the heavy rare earth elements (HREE; $Gd_N/Yb_N$ ~$0.15x10^3$) and moderate Y-content (~$8x10^3$ ppm). The remaining spots but one have similar HREE and Y-content, display homogeneous REE-spider plots, and tightly cluster in the $Gd_N/Yb_N$-vs-date and Y-vs-date plots ($Gd_N/Yb_N$ ~$0.18x10^3$; Y ~$7x10^3$ ppm).

In the Tera Wasserburg diagram, the U-Pb data are mainly subconcordant to slightly discordant (fig. 17A). The only spot in garnet 1 is slightly discordant. Linear regression through eighty-two data points determines a discordia with a lower intercept date of 286.5 ± 1.5[6] Ma (MSWD = 1.6; L267) and an initial $^{207}Pb/^{206}Pb$ value of 1.32 ± 0.5. Despite the large uncertainty, the calculated initial isotopic Pb composition agrees with the terrestrial Pb evolution model of Stacey and Kramers (1975). An equivalent mean $^{206}Pb/^{238}U$ date of 285.5 ± 1[6] Ma with a similar MSWD value of 1.6 can be calculated using the same data points after correction for the incorporation of common Pb (fig. 17D).

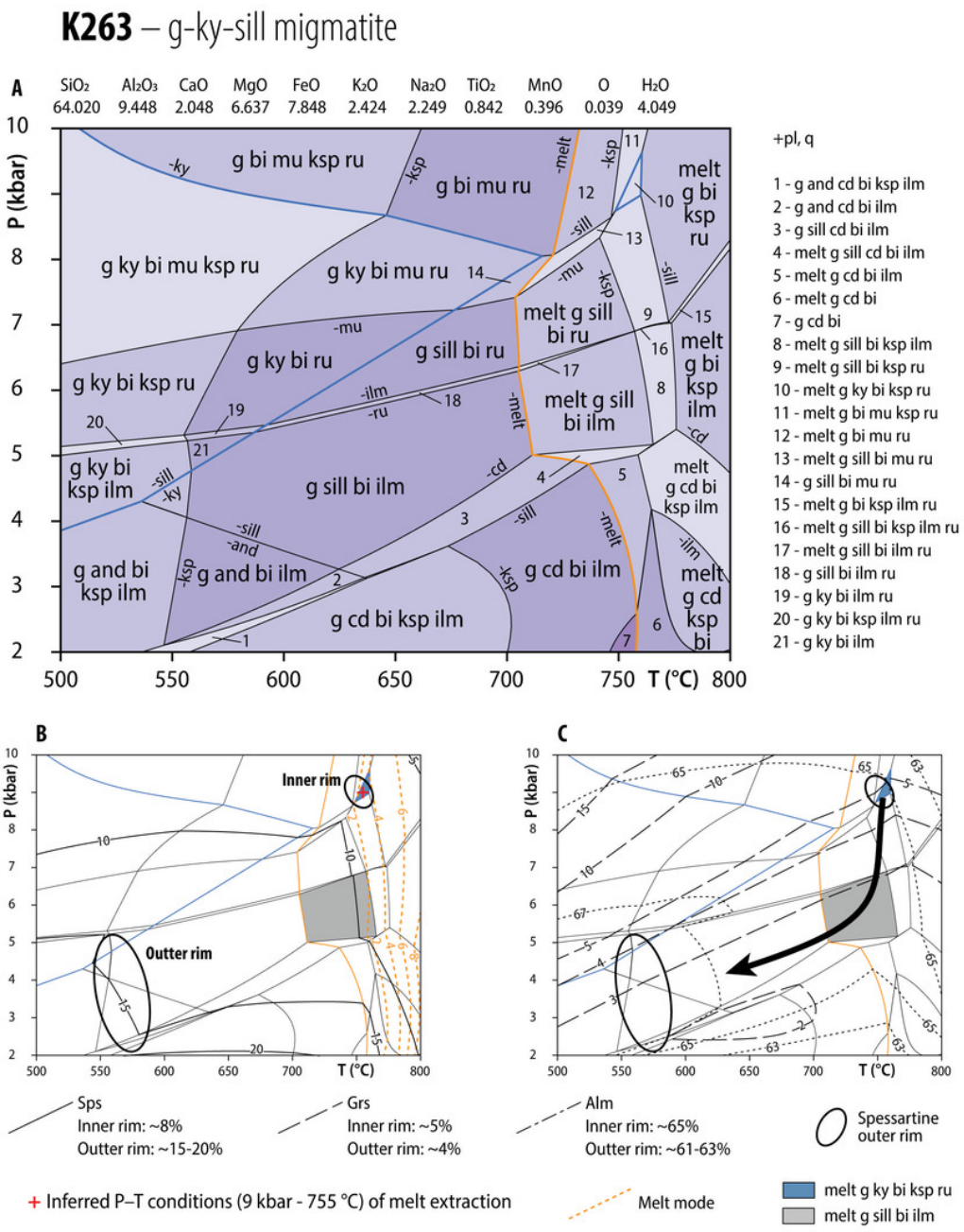


**Figure 13. A) *P–T* pseudosection constructed with the SEM-measured bulk composition of the sample K263 and $H_2O$ undersaturated conditions (see text for details). B–C) Modal isopleths for the melt and compositional isopleths for garnet. The maximum amount of melt is modelled at the estimated peak *P–T* conditions, and the composition of the melt modelled at these conditions was used for the reintegration procedure (see text for details).**

*4.3.2. D241 – Garnet-staurolite-kyanite-sillimanite micaschist*

Monazite crystals occur in garnet 1, fully or half included in garnet 2, along grain boundaries, epitaxial with micas, in sillimanite coronas around staurolite; and fully included in matrix quartz or plagioclase (fig. 18). Small monazite (~10 µm) inclusions in garnet 1 systematically occur in a Y-rich zone of the garnet crystal (fig. 18A). Monazite outside garnet 1 tends to be larger (up to 50 µm), the largest ones were mapped, no core-rim relationships could be detected, but a patchy zoning is illustrated by Y and Th maps (fig. 16H). A total of 65 spots in 53 monazite crystals were analyzed. Individual spots show a strong correlation between the textural position of the analyzed crystal in the thin section and the date, but no obvious relationship between the internal chemical zoning analyzed and the date.

In the trace elements plots for monazite, only 5 spots from the monazite included in garnet 1 are displayed because of the small crystal size and resulting contamination with garnet during ablation. Monazite in garnet 1 shows a moderate slope of the HREE ($Gd_N/Yb_N$ 0.4–0.9x$10^3$) and moderate Y-content (~ 10x$10^3$ppm), while monazite in the

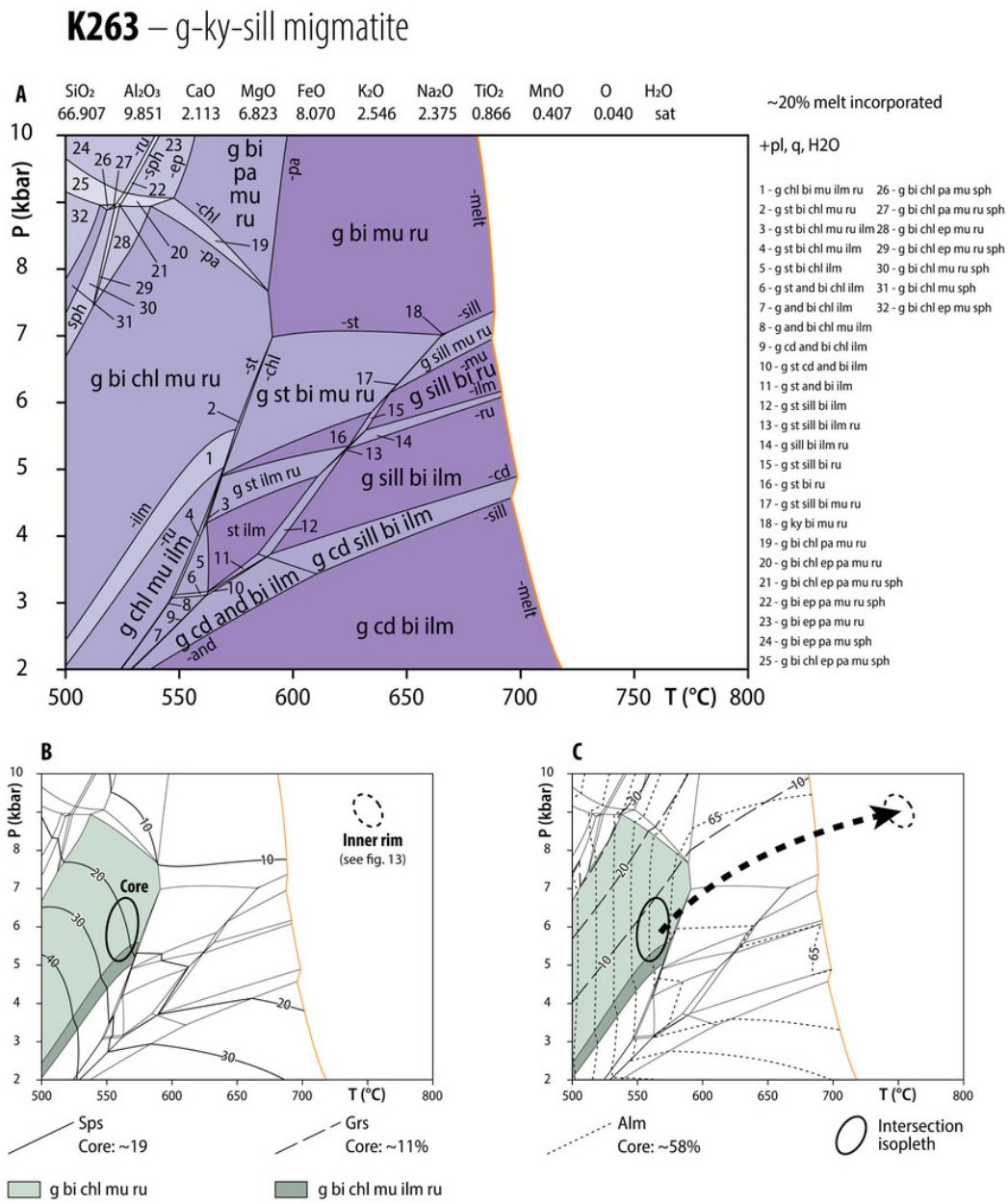


**Figure 14. A) *P–T* pseudosection constructed for the calculated initial composition of K263 estimated following the melt re-integration procedure detailed in the text. B–C) compositional isopleths for garnet.**

other textural positions shows a wider range of the $Gd_N/Yb_N$ ratio (0.5–1.3x$10^3$) and lower Y content (~ 1–7x$10^3$ ppm). Among the early Permian crystals, those opened to the matrix display higher values of the $Gd_N/Yb_N$ ratio (up to 1.3x$10^3$), compared to the crystals fully included in garnet, quartz, or plagioclase ($Gd_N/Yb_N \leqslant$ 0.6x$10^3$), and the $Gd_N/Yb_N$ ratio is negatively correlated with Y-content.

In the Tera Wasserburg diagram, the crystals included in garnet 1 yield lower Carboniferous dates (*ca.* 350–330 Ma) while those in other textural positions are mostly early Permian (*ca.* 300–280 Ma). Both groups are characterised by subconcordant to moderately discordant spots (fig. 17B), indicating a limited incorporation of common Pb. Nine out of the eleven analyses from crystals in garnet 1 and one spot half included in garnet 2 yield a discordia with a lower intercept date of 339.5 ± 6.5[9.5] Ma. Because of the limited discordance of the spots, the calculated upper intercept was meaningless, thus, the intercept was fixed for a $^{207}Pb/^{206}Pb$ (0.8583) value after Stacey and Kramers (1975). The resulting discordia have quite a large MSWD value related to a moderate spread of the most concordant spots and the small number of data points. Following a correction for the common Pb, a similar mean $^{206}Pb/^{238}U$ date of 339 ± 6.5[9.5] Ma (MSWD = 3.2; D241) can be calculated using the same group of spots (fig. 17D). The younger group, mostly from crystals outside of garnet 1, fifty-three spots display a range of dates between 300 and 280 Ma. Due to the limited discordance of the spots, we assumed a fixed $^{207}Pb/^{206}Pb$ (of 0.8545) after Stacey and Kramers (1975) to calculate a discordia, which yields a lower intercept date of 288 ± 1.5[6] Ma. The discordia has a moderate MSWD value of 1.7, in-

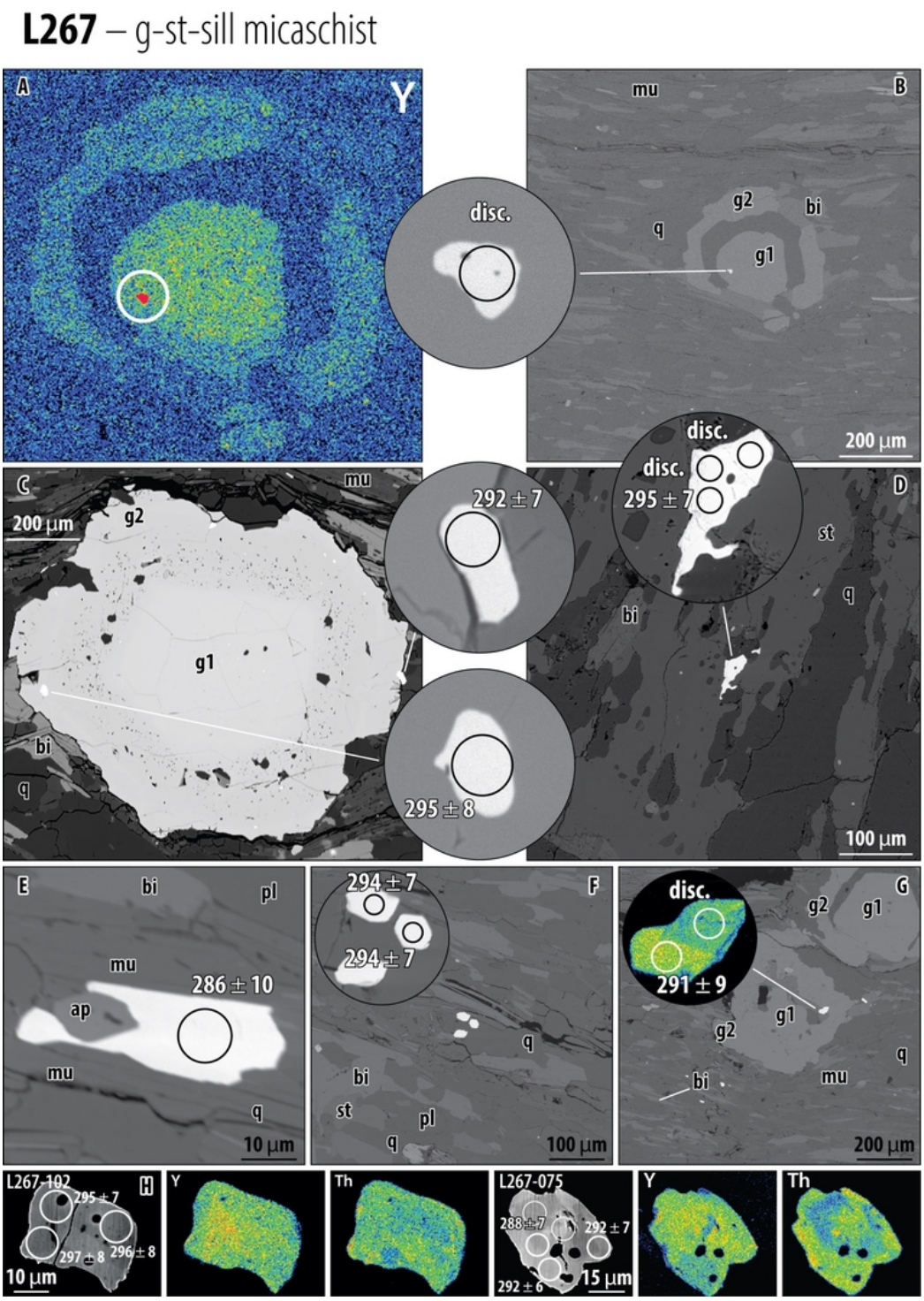


**Figure 15. Monazite in L267 – A) X-ray map of Y showing a monazite inclusion in garnet 1 and (B) BSE image of the same monazite. C) BSE image of monazite in garnet 2. D) BSE image of monazite in staurolite. E) BSE image of monazite along the cleavage of muscovite. F) BSE image of monazite inclusions in quartz. G) BSE image of monazite half included in garnet 2. H) Two sets of high contrast BSE, and Y and Th X-ray maps showing a patchy zoning in monazite. The circles in BSE images highlight the position and apparent age of LASS spots**

dicating a limited dispersion. The lower intercept date is equivalent to a mean $^{206}Pb/^{238}U$ date of 287.5 ± 1.5[6] Ma (MSWD = 1.6; D241) calculated using common Pb corrected dates from the same spots.

*4.3.3. K263 – Garnet-kyanite-sillimanite migmatite*

Monazite is observed along the cleavage of biotite and grain boundaries; included in large quartz and plagioclase; and included in garnet, usually as small inclusions (~5 µm) and once as a larger inclusion (~50 µm) together with plagioclase (fig. 19). Monazite contains inclusions of apatite,

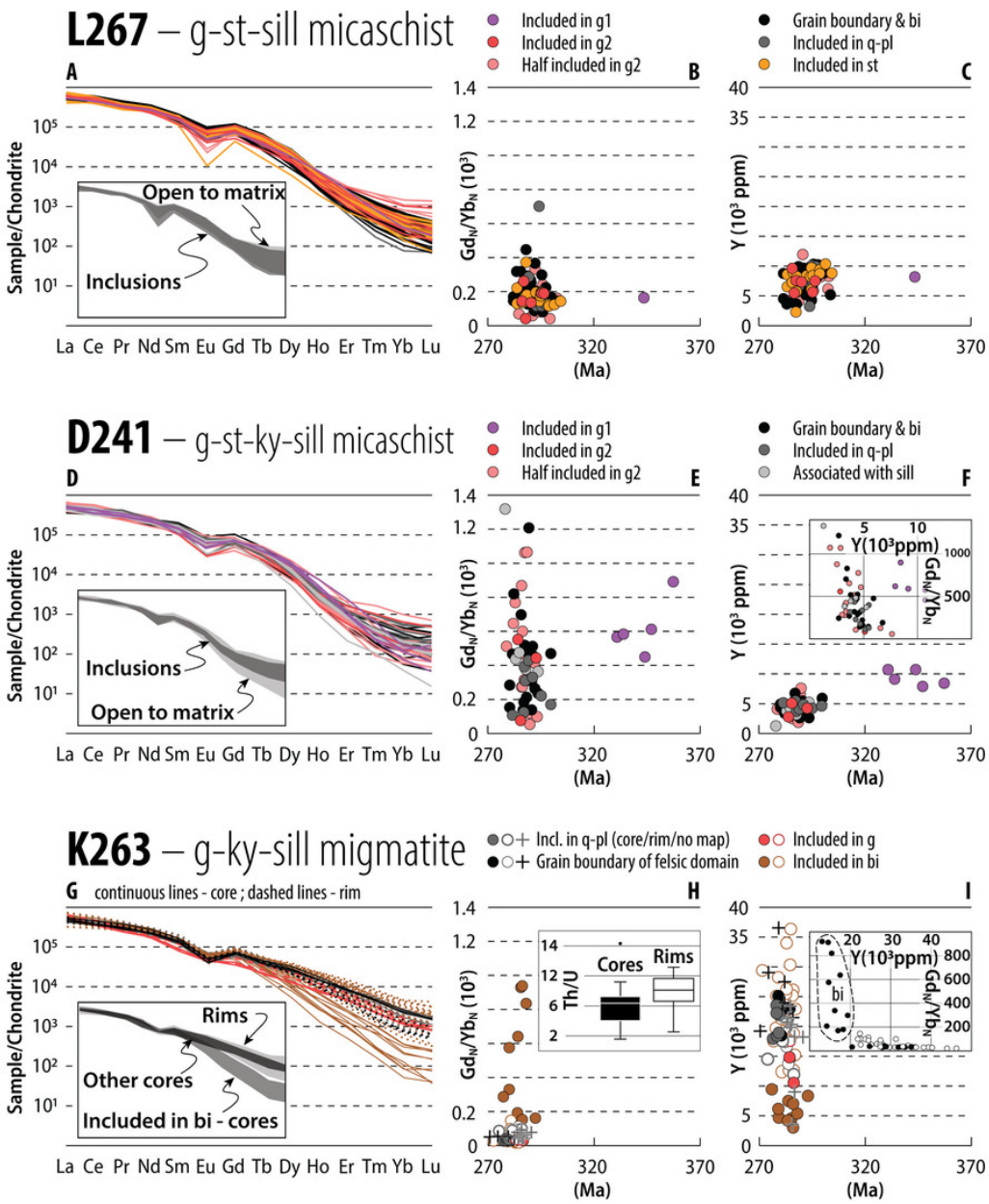


**Figure 16. Trace element in monazite – chondrite normalized REE patterns, Age vs GdN/YbN and Age vs Y binary plots for monazite from (A–C) D241, (D–F) L267, and (G–I) K263. Insets in (A), (D) and (G) – textural control on the REE distribution in monazite. Such a control is visible in D241 and K263, but not in L267. Insets in (F) and (I) – textural control on the Y content and the ratio GdN/YbN in D241 and K263. Inset in (H) – Th/U ratio of monazite cores and rims in K263.**

quartz, biotite and zircon. The crystals tend to be large (50–100 µm), and most of them were mapped. These maps show a core-rim relationship (fig. 19), indicating in most cases that at the scale of a single crystal, the rims are enriched in Y and Th relative to the cores. Yttrium in the cores defines either distinctly enriched bands (fig. 19B and D) or a patchy zoning (fig. 19G). Both Y and Th commonly show a patchy zoning in the rims (fig. 19G). None of the 83 spots performed in 14 crystals from each textural position (i.e., in thin section) allow for the discrimination of a textural control on the dates, as both cores and rims yield equivalent early Permian dates.

Trace element plots from the mapped crystals unravel a textural control on the incorporation of the trace elements (fig. 16G to I). The cores of monazite associated with biotite in the melanosome display a steeper slope of the HREE (0.2–0.9 $10^3$) and average lower Y content (Y: 3–8.3x$10^3$ ppm) than the cores in the leucosome (Y: 7–28x$10^3$ ppm; $Gd_N/Yb_N$ < 2 $10^3$). The rims display a restricted range of $Gd_N/Yb_N$ (< 2 $10^3$) and a large scatter of the Y-content (3–36x$10^3$ ppm) without apparent relationship with the textural position.

In the Tera Wasserburg diagram, all the data are concordant (fig. 17C). All the spots are used to calculate a concordia date of 283.5 ± 1[6] Ma ($MSWD_{C+E}$ = 1.2; K263) and an identical mean $^{206}Pb/^{238}U$ date with MSWD = 1.1 (fig. 17D).

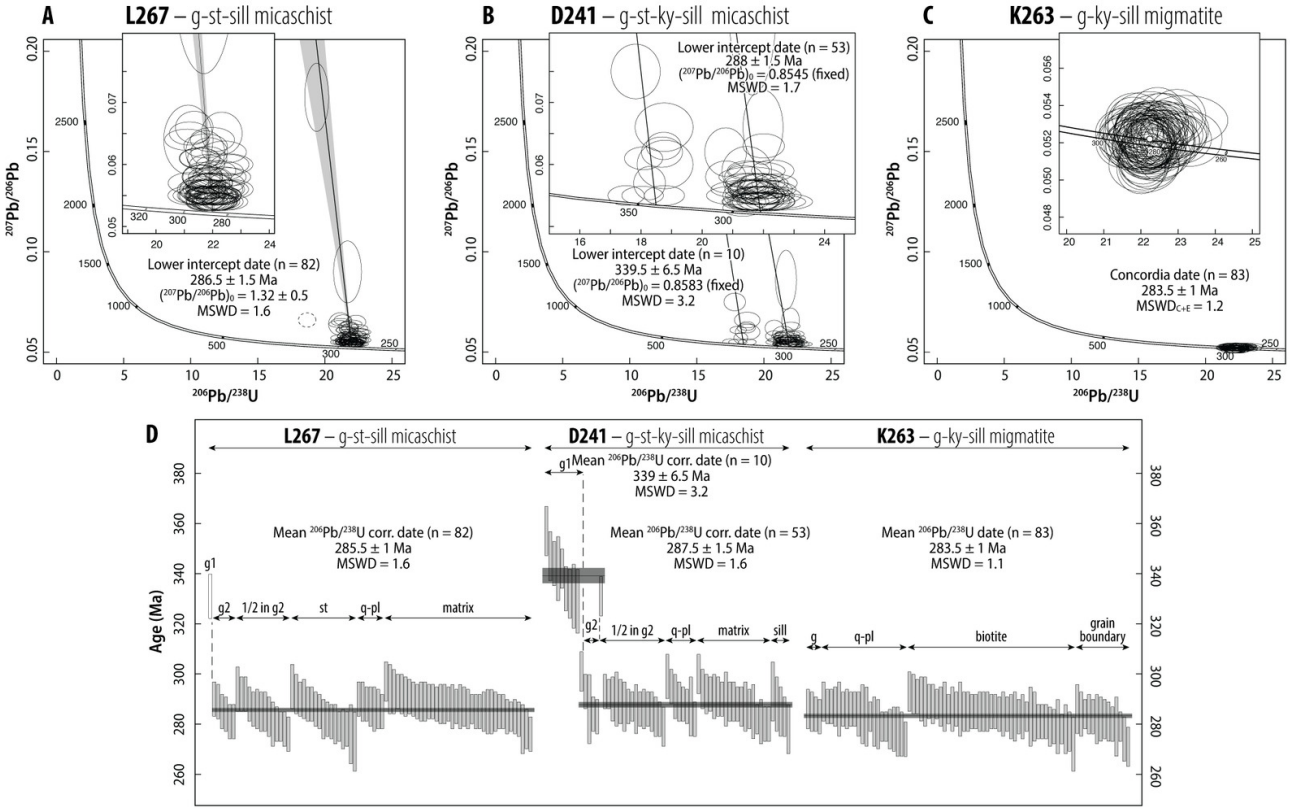


**Figure 17. U-(Th-)Pb geochronology of monazite. Terra-Wasserburg plots of monazite U–Pb data for (A) L267, (B) D241 and (C) K263. D) Weighted mean U–Pb plots with indication of the textural position of the analyzed crystals. The dashed ellipse in (A) and the empty bar in (D) were rejected from the age calculations.**

## 4.4. Zircon geochronology

This section provides a short description and summary of the U-Pb isotopic results of zircons from magmatic rocks. Field and petrographic pictures of the related samples are available in the supplementary figure S1.

### *4.4.1. Y269B – Diorite dike*

Y269B is an undeformed diorite dike cutting across the main foliation of the Central Domain. It is composed of plagioclase (~65 %), green biotite (~15%), greenish to blueish amphibole (~10 %), titanite (up to a few per cent), and accessory epidote (~1 %), apatite, and zircon.

Zircon crystal fragments from the sample are usually quite large (up to 700 µm). The fragments normally display broad, striped zonation in CL images, and some grains show homogeneous domains (fig. 20A). Twelve analyses conducted on different grains, yield mostly concordant results, and all but one have Th/U > 0.2 (fig. 20A). Nine concordant analyses define a concordia date of 290 ± 2[6] Ma (MSWD = 1.3; Y269B). One concordant spot plots at *ca.* 410 Ma. The *ca.* 410 Ma grain could be a xenocryst from the country rocks, while the *ca.* 290 Ma date is interpreted as the emplacement age of the dike.

### *4.4.2. Y261A – Nebulitic migmatite*

The sample Y261A is a nebulitic migmatite composed of plagioclase (~70 %), quartz (~10–20 %), biotite (<10 %), K-feldspar (< 5 %), garnet (~1 %), and accessory ilmenite, apatite, and zircon.

Zircon crystals are dominantly euhedral, 100–300 µm in length, and with a length/width ratio from 1:1 to 1:3. These grains display well-developed oscillatory zoning in the CL images (fig. 20B), suggesting an igneous origin. Twenty-five analyses were conducted, yielding concordant to slightly discordant results (fig. 20B) with high Th/U ratios of 0.22–1.55. Sixteen concordant to discordant spots form a main cluster with a weighted mean $^{206}Pb/^{238}U$ age of 376 ± 1.5[7.5] Ma (MSWD = 1.2; Y261A). The seven concordant spots from this cluster yield an equivalent concordia date of 377 ± 2[8] Ma (MSWD = 1.4). A subordinate group defined by four (sub)concordant spots plots in the range of *ca.* 460–440 Ma, and one remaining concordant analysis plots at *ca.* 510 Ma. Three discordant data points probably result from limited Pb-loss. The main *ca.* 376 Ma age population can be interpreted either as a maximum depositional age of the sedimentary protolith, or as an igneous age related to the crystallisation of melt in the migmatite. The older concordant Ordovician grains may be detrital crystals inherited from the sedimentary protolith.

### *4.4.3. Y261B – Garnet-kyanite-sillimanite migmatite*

The sample is a garnet-kyanite-sillimanite migmatite comparable to K263, with plagioclase (~40 %), quartz (~30 %), biotite (~20 %), K-feldspar (< 5 %), and accessory ilmenite, rutile, monazite, apatite, and zircon.

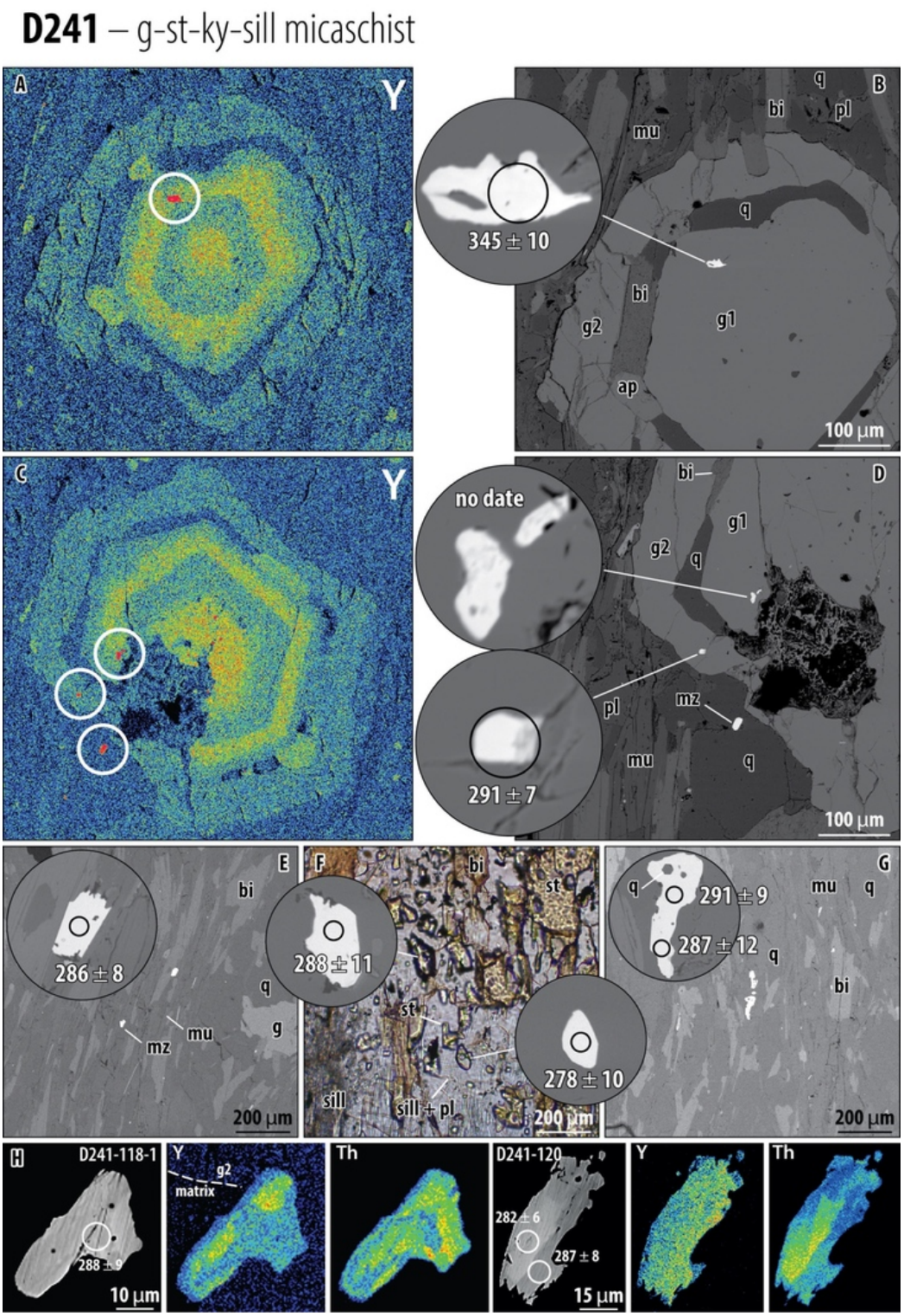


**Figure 18. Monazite in D241 – A) X-ray map of Y in garnet with a monazite inclusion and (B) BSE image of the same monazite. C) X-ray map of Y in garnet with monazite crystals included in garnet 1, in garnet 2 and in quartz. D) BSE image of the same monazite crystals. Note that monazite crystals in garnet 1 occur in a Y-rich zone. E) BSE image of monazite along the cleavage of muscovite. F) Plain-polarized image of monazite crystals associated with sillimanite next to staurolite G) BSE image of monazite included in matrix quartz. H) two sets of high contrast BSE, and Y and Th X-ray maps showing a patchy zoning in monazite. The circles in BSE images highlight the position and apparent age of LASS spots.**

Zircon crystals are subhedral or rounded, 100–200 µm in size and display a length/width ratio between 1:2 and 1:3. The CL images usually show a blurred oscillatory zoning, locally interrupted by a thin (~10 µm) bright rim (fig. 20C). The oscillatory zoning suggests an initial magmatic crystallisation, the rounded feature of the crystals point to

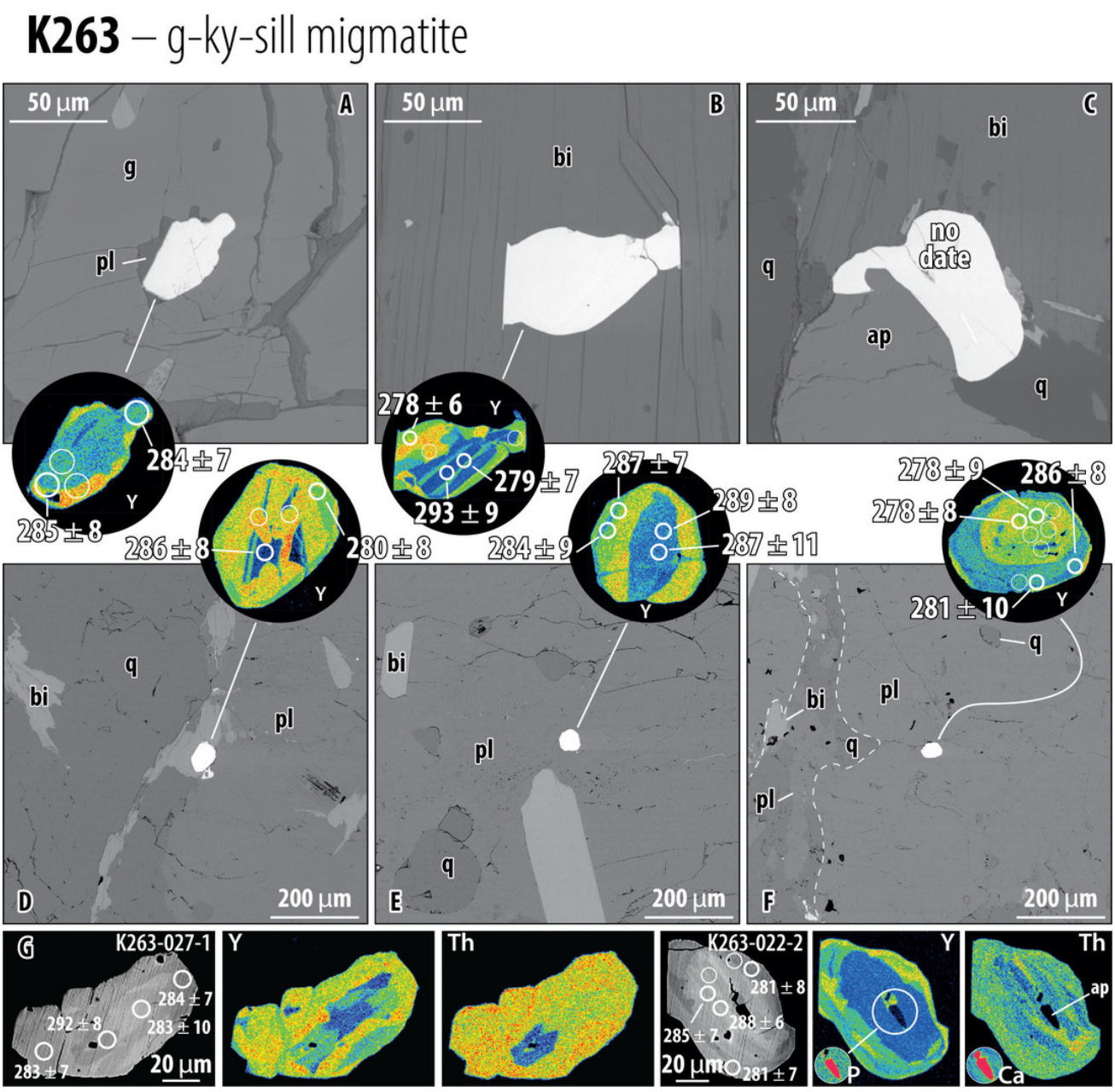


**Figure 19. Monazite in K263 – BSE images and Y maps of monazite (A) included in garnet, (B) along biotite cleavage, (C) partially inlcuding apatite, (D) along the grain boundary in the leucosome, (E–F) included in coarse plagioclase in the leucosome. G) Two sets of high contrast BSE and Y and Th X-ray maps of monazite crystals. The position of LASS spots and apparent ages are indicated. Note the apatite inclusion in monazite in (G).**

subsequent sedimentary reworking and the blurred texture points to a metamorphic overprint. Fifty spots analysed in the blurred oscillatory zoned crystals yield mostly concordant results with high Th/U in the range 0.28–1.1. In the Wetherill diagram, most crystals plot between *ca.* 520 and 380 Ma (fig. 20C). Because of the spread along the concordia curve, the data are also shown in a 'relative density plot' where nineteen spots define a peak at *ca.* 410 Ma corresponding to a weighted mean $^{206}Pb/^{238}U$ date of 412.5 ± 2[8.5] Ma (MSWD = 1.2; Y261B). Nine younger spots range between *ca.* 410 and 380 Ma. The *ca.* 520–420 Ma dates can be considered as the age of detrital zircons, but it is unclear whether the Devonian cluster of *ca.* 410–380 Ma represents a maximum depositional age or the crystallisation age of the melt in the migmatite.

*4.4.4. Y259 – Tourmaline tonalite sill*

The sample Y259 is a weakly deformed tonalite sill parallel with the lithological layering ($S_{Main}$) in the migmatite. It is composed of plagioclase (~60 %), quartz (~20 %), biotite (~10%), K-feldspar (< 5 %), tourmaline (2%), and accessory ilmenite, apatite, and zircon.

Zircon crystals are subhedral, typically 200 µm in size with length/width ratio between 1:1 and 1:4. CL images of most crystals show a dark homogeneous core with faint outer brighter zones and rare ones display a brighter core

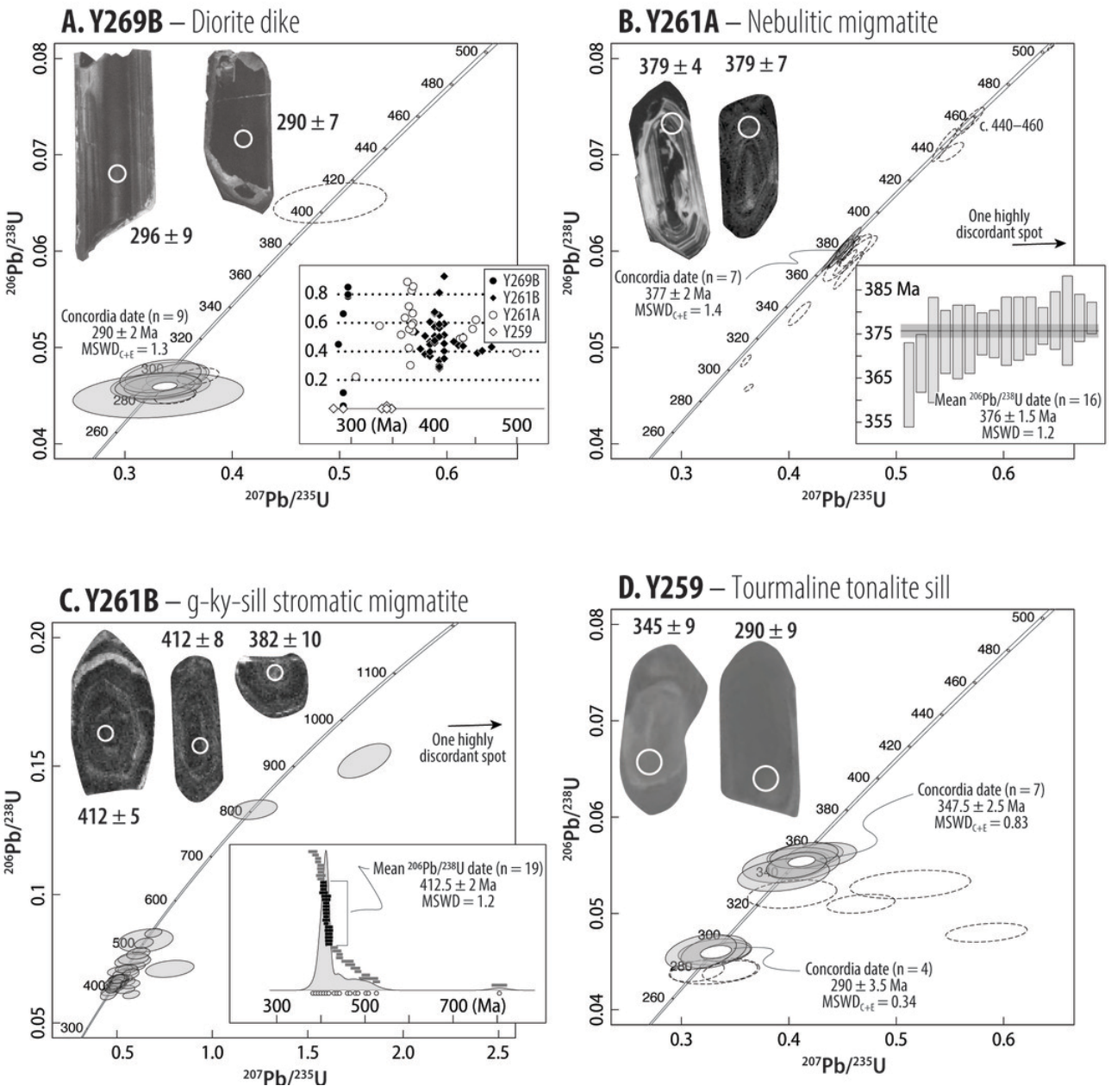


**Figure 20. Wetherill plot of U–Pb data and CL images of zircon for (A) Y269B, (B) Y261A, (C) Y261B, (D) Y259. The white circles on the CL images show the location of LASS spots and their U–Pb apparent ages. Inset in (A) Th/U ratios the zircons from all the samples. Inset in (B) Weighted Mean Average plot for Y261A. Inset in (C) Relative probability plot for Y261B.**

with a blurred zoning pattern (fig. 20D). Most of the data are concordant, plot as two clusters at *ca.* 350 Ma and *ca.* 290 Ma (fig. 20D). All the spots display a very low Th/U < 0.005 regardless of the date. Seven analyses, including the spots from the cores, define a main cluster with a concordia date of 347.5 ± 3[7.5] Ma (MSWD = 0.83; Y259). Four analyses form a secondary cluster with a concordia date of 290 ± 4[7] Ma (MSWD = 0.34). Despite the very low Th/U ratio suggesting a metamorphic nature of the zircons, the magmatic protolith of the deformed sill indicates that a magmatic origin of the Carboniferous zircon and a metamorphic nature of the Permian one are most likely.

## 5. INTERPRETATION

### 5.1. *P–T* evolution

In this section, the *P–T* evolution is summarised (fig. 21) and discussed to assess the uncertainty relative to each segment of the *P–T* path. The micaschists display many petrographic similarities and are consequently discussed together.

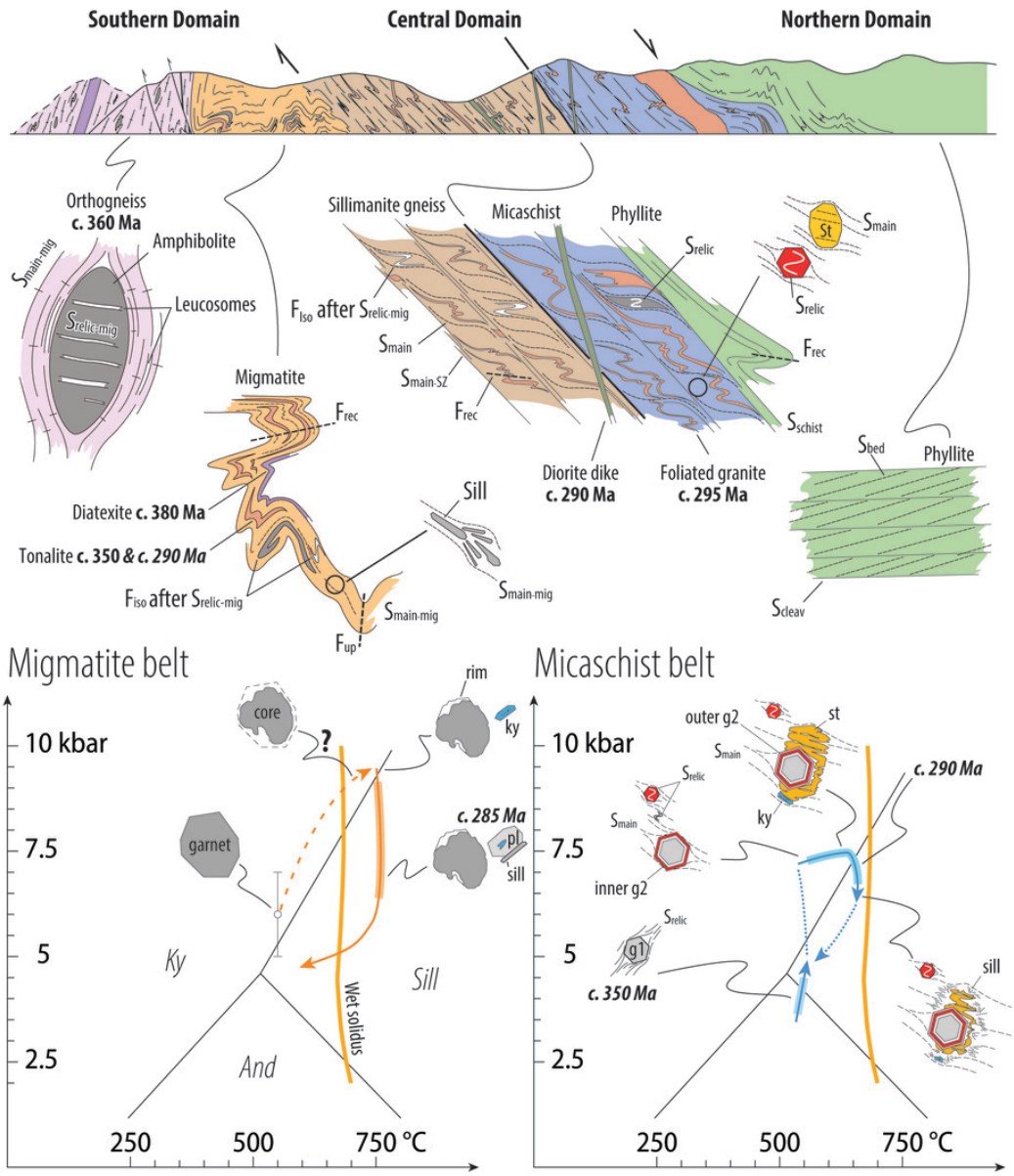


**Figure 21. Summary of the main field and petrographic observations, pseudosection modeling, and U(-Th)-Pb results.**

*5.1.1. Garnet-staurolite-sillimanite and garnet-staurolite-kyanite-sillimanite micaschist*

The *P–T* paths determined in the micaschists involve three metamorphic stages, M1, M2, and M3. In general, the consistency of the *P–T* estimations between the two samples and those of Sukhorukov et al. (2016) suggests the robustness of the results.

M1 corresponds to an initial increase of *P* and *T* from ~3–4 kbar, 525–550 °C to ~5–6 kbar, 550–600 °C, documented by partial assemblages in garnet 1 and its compositional zoning. Garnet 1 in the g-st-ky-sill micaschist D241 displays a high-Y annuli, a feature previously correlated with the crossing of the staurolite isograd (see Corrie & Kohn, 2008). In agreement, the isopleths for garnet 1 overlap the staurolite-in line, yet the pseudosection modeling indicates that most of M1 occurred in the chlorite stability field.

Between M1 and M2, a pressure increase to 6–7 kbar is suggested by the compositional difference between garnet 1 rim and the inner garnet 2, as well as by rutile in the mineral ring of garnet from the g-st-sill micaschist L267. The atoll morphology of garnet can be accounted for by several mechanisms (Godet et al., 2022; Kulhánek et al., 2021; Robyr et al., 2014; Štípská et al., 2014, and references therein). A detailed discussion of these mechanisms is outside the scope of this study. Yet, even if significant dissolution of garnet core is often involved in the formation of atoll garnets (e.g., Kulhánek et al., 2021), it does not need to be so (e.g., Godet et al., 2022). The latter study suggested that an interruption of garnet growth along a segment of the P–T path can result in the formation of the atoll morphology. In the present case, garnet 1 is systematically euhedral, and garnet 2 has low Mn-content, which does not support significant dissolution of the garnet core. On the

other hand, garnet growth interruption can be accounted for by a P–T path with limited cooling along the line '-g' in figure 10 and figure 12.

M2 corresponds to an isobaric heating documented by the destabilisation of chlorite included in the inner garnet 2 (g-st-sill micaschist L267; fig. 6D), and by the appearance of staurolite in textural equilibrium with the outer garnet 2. As mentioned previously, while it is possible that the g-st-ky-sill micaschist D241 reached the staurolite isograd during M1, the systematic textural equilibrium observed between staurolite and garnet 2 suggests that M2 was the main staurolite-bearing metamorphic stage. The assemblages and outer garnet 2 compositions of both samples indicate identical conditions of the pressure peak of ~7–8 kbar but support different peak temperatures of ~625–650 °C (g-st-sill micaschist L267) and ~650–675 °C (g-st-ky-sill micaschist D241).

M3 was related to a decompression below 6–7 kbar, indicated by the growth of sillimanite and the slight XFe and spessartine increase observed at the very rim of the garnet crystals.

#### *5.1.2. Garnet-kyanite-sillimanite migmatite*

The *P–T* evolution of the g-ky-sill migmatite K263 is characterised by M1, M2, and M3. M1 is documented by the composition and inclusion content of garnet core, pointing to ~550 °C and ~6 kbar. The anhedral shape of the inclusion-rich garnet core (fig. 8C) potentially indicates resorption before the growth of the inclusion-free garnet rim. Given the high-temperature character of the sample, the observed smooth compositional zoning across the sharp optical interface could result from diffusional relaxation (e.g., Ague & Baxter, 2007). In this condition, significant modification of garnet core composition is likely. Yet the compositional isopleth for spessartine and grossular shows that even if Mn and Ca diffused toward the rim, garnet would have crystallised at even higher pressure and lower temperature. Thus, exact *P–T* conditions are inaccessible, but garnet core composition and small inclusions remain compatible with a prograde subsolidus origin.

Due to diffusion, garnet zoning cannot be used to constrain the detailed shape of the *P–T* path between M1 and M2 (dashed line in fig. 21). Furthermore, diffusion limits our ability to determine the composition fractionated by garnet and thus to estimate the effective bulk composition, especially during M2. In this case, we used the measured bulk composition modified with a limited amount of $H_2O$, which remains the most unbiased approximation. M2, documented by the inferred former presence of melt, kyanite inclusions, rutile, and garnet 2 correspond to the peak *P–T* conditions modelled around ~750 °C and ~9 kbar. This suggests partial melting of the lower crust. Even if garnet fractionation could be accounted for, it would most likely not modify the topology of the pseudosection to a point that it becomes incompatible with this conclusion, which may, therefore, be considered robust.

M3, marked by the conspicuous replacement of kyanite in the matrix and the inferred appearance of ilmenite, occurred during decompression. The absence of textures indicating fluid-driven back-reactions (e.g., Waters, 2001) suggests that melt was lost at the peak conditions. Therefore, the efficient replacement of kyanite by sillimanite in the matrix suggests that M3 initially occurred while melt was still present and implies an isothermal decompression down to 700–775 °C and 5–6 kbar before cooling. Cooling is documented by the crystallisation of melt, later appearance of chlorite, and slight XFe and spessartine increase in garnet rim (e.g., Florence & Spear, 1991).

### 5.2. *P–T–t* evolution

#### *5.2.1. Garnet-staurolite-sillimanite and garnet-staurolite-kyanite-sillimanite micaschist*

The results of monazite dating in both micaschist samples are consistent and disclose a first-order textural control on the U-Pb results. In both cases, monazite included in garnet 1 is Carboniferous (*ca.* 350–330 Ma) while those in other textural positions are early Permian (*ca.* 290–275 Ma).

In g-st-ky-sill micaschist D241, monazite crystals are not randomly distributed in garnet 1 but systematically associated with the high-Y annuli (fig. 18A, C). Previous studies reported a similar mode of occurrence of monazite in garnet (Kohn & Malloy, 2004), which was interpreted as the result of prograde metamorphic reaction(s) (Corrie & Kohn, 2008). Recent studies showed that monazite can remain largely inert during metamorphism, which can hamper the direct attribution of a monazite date to the growth of its garnet host (e.g., March et al., 2024; Thiessen et al., 2019). However, these studies addressed the response of monazite in $H_2O$-undersaturated granulite-facies rocks while countless studies of subsolidus prograde metapelites conclude that monazite grows or recrystallises, likely in the presence of a fluid, during the prograde P–T path (Štípská et al., 2015 and references therein). Monazite in garnet 1 is accordingly interpreted as the crystallisation product of prograde metamorphic reactions during $M_{1\text{-mic}}$. In g-st-sill micaschist L267, the single monazite analysis in garnet 1 ($^{207}$Pb-corrected $^{238}U/^{206}Pb$ date of *ca.* 330 Ma) cannot be interpreted as a metamorphic age. In g-st-ky-sill D241, the perceptible spread of the U–Pb data and the relatively high MSWD of 3.2 suggest partial reopening of the U-Pb isotopic system, possibly related to the subsequent Permian metamorphism. Consequently, the Carboniferous *ca.* 340 Ma date from g-st-ky-sill micaschist D241 is interpreted as the minimum crystallisation age of the monazite during $M_{1\text{-mic}}$.

The U-Pb dates from crystals in other textural positions spread from *ca.* 300 Ma to *ca.* 275 Ma but do not reveal a clear textural control (fig. 19). Nevertheless, monazite crystals included in garnet 2 and staurolite are texturally related to M2, whereas those associated with sillimanite are texturally associated with M3, indicating that monazite could be affected by both events. In agreement, monazite crystals show a patchy zoning typical for recrystallised monazite (see Bosse & Villa, 2019, and references therein). The larger spread of the $Gd_N/Yb_N$ in D241 than in L267 is correlated with the amount of sillimanite, suggesting that monazite effectively reacted during M3. In agreement, in

D241, the spread $Gd_N/Yb_N$ is limited in monazite crystals fully enclosed in M2-porphyroblasts but prominent in crystals opened to the matrix. Furthermore, in the same sample, $Gd_N/Yb_N$ is negatively correlated to Y-content, suggesting that garnet was a competitor for HREE and Y (Skrzypek et al., 2018 and references therein). In this context, the trace element and textural data can be reconciled if monazite inclusions (re)crystallised early during M2 and progressively recrystallised or were modified later, when more garnet was present in the rock, during M3. Importantly, garnet resorption observed in the vicinity of sillimanite during M3 (fig. 6G) is a rare feature, only observed once, suggesting that release of HREE and Y during M3 did not significantly affect the bulk rock trace element budget. Finally, the moderately high MSWDs of 1.5–1.7 for the calculated dates are compatible with a limited overdispersion and progressive monazite recrystallisation. Hence, the geochronological data suggest a Permian (*ca.* 285–280 Ma) quick metamorphic continuum between M2 and M3.

*5.2.2. Garnet-kyanite-sillimanite migmatite*

Monazite in the sample K263 is found in several textural positions. It is included in coarse quartz and plagioclase (fig. 17E and F), which contain kyanite inclusions (fig. 7G). Monazite is also included in biotite, marking the main foliation with sillimanite. In biotite, the shape of the Y-rich rim of monazite is texturally controlled by biotite cleavage (fig. 17B), suggesting contemporaneous growth. Finally, monazite is common along grain boundaries (fig. 17D) where interstitial melts crystallised. These positions suggest monazite existed at the peak-pressure conditions and during decompression. In a range of *P* and *T* relevant for our study, a significant monazite amount can effectively survive partial melting in metagreywacke (Yakymchuk & Brown, 2014). Furthermore, monazite contains inclusions of apatite or overgrows apatite crystals (fig. 19C, G), thus apatite dissolution possibly favoured the preservation of monazite above the solidus (e.g., Wolf & London, 1995; Wolfram et al., 2017). Trace element data from the core of monazite crystals included in biotite show, like in the micaschist sample D241, a negative correlation between $Gd_N/Yb_N$ and Y, suggesting a prograde origin during garnet growth. Lower $Gd_N/Yb_N$ and higher Y of the core of monazite in the leucosome suggest that the effect of garnet fractionation was less important in the leucosome. Compared to the monazite core, higher Th/U in the rim is compatible with (re)crystallisation of the rim at higher temperature (e.g., Williams et al., 2022). Furthermore, the low $Gd_N/Yb_N$ and high-Y of monazite rim may be tentatively explained by interaction with a melt enriched in Y and HREE due to garnet dissolution (e.g., Závada et al., 2021), which may be accounted for by the isothermal decompression M3.

Monazite core-rim chemical zoning indicates two genetic periods apparently at odds with the homogeneous U-Pb results. The rim usually displays a patchy texture (fig. 17), which could result from coupled dissolution-precipitation in the presence of melt (e.g., Varga et al., 2020). According to the same study, recrystallisation can result in a decoupled behavior of U-Pb and trace elements, but the variable reincorporation of components from the dissolved crystal would result in the preservation of an inherited isotopic signature. In nature, this usually results in a spread of the isotopic data (e.g., Didier et al., 2014; Weinberg et al., 2020), which is not observed here. Therefore, the tightly clustered U-Pb results obtained in monazite core and rim (fig. 19) suggest a close spacing in time of the two (re)crystallisation events, at a scale unresolvable by the dating method.

In agreement, the concordia U-Pb date 283.5 ±1[6] Ma ($MSWD_{C+E}$ = 1.4) and the equivalent mean $^{206}Pb/^{238}U$ date (283.5 ± 1[6] Ma; MSWD = 1.1) are interpreted as the age of decompression between M2 and M3. The tight cluster of U-Pb data obtained in the monazite core and rim is somewhat in agreement with the isothermal decrease of pressure between M2 and M3, suggesting a rapid decompression.

## 6. DISCUSSION

Along the studied section, the prograde and retrograde character of the micaschist and sillimanite-gneiss, respectively, indicate the location of a major structural boundary. The prograde metamorphic evolution of the micaschist is tracked relatively clearly by mineralogical changes and garnet zoning. On the other hand, a polyphase metamorphism in the migmatite complicates the relationships between the structures, metamorphism, and ages. The discussion is introduced with a summary on the development of migmatite domes in the Mongolian Altai. In this frame, we then discuss the geological evolution of the micaschists and migmatite, and finally propose a petrological model for the development of the Barrovian metamorphic sequence.

### 6.1. Devonian-Carboniferous and Permian orogenic cycles affecting the Altai Wedge

A main geological feature of the Altai Belt is the contrast between low- to medium-grade metasediments in the north and migmatite with abundant igneous rocks in the south (e.g., Badarch et al., 2002). Commonly, the metamorphic envelope of the high-grade complex exposes “Barrovian” garnet-staurolite micaschist (Jiang et al., 2015; Kong et al., 2022; Sukhbaatar et al., 2022), and the sillimanite and cordierite migmatite core features xenomorphic kyanite and/or staurolite inclusions (e.g., Burenjargal et al., 2014; Jiang et al., 2015).

In the Chinese Altai, the study of high-grade dome structures by Wang et al. (2021) and Kong et al. (2022) documented an originally subhorizontal migmatitic foliation S1 variably folded and transposed into a vertical cordierite-bearing foliation S2. Xenomorphic inclusions of staurolite and kyanite are interpreted as part of an older Ordovician or Silurian metamorphism (Jiang et al., 2019, 2022). Geochronological results of migmatites and granites cogenetic with the different structures indicate that S1 is *ca.* 410 Ma old, S2 is *ca.* 405 Ma and cross-cutting dikes are *ca.* 380 Ma, thus indicating a purely Devonian age for the dome formation. Similar structures occur in the Chandman Massif of the Mongolian Altai (Broussolle et al., 2015), but there, the

age of horizontal fabric is constrained at *ca.* 360 Ma while the vertical transposition D2 was dated at *ca.* 350–345 Ma by syntectonic granite sheets (Lehmann et al., 2017). The age difference between these two locations is understood as the eastward propagation of a single tectonic event (Aguilar et al., 2024; Kong et al., 2022).

In contrast to the monocyclic Devonian to Carboniferous formation of domes, the study of Sukhbaatar et al. (2022) documents two partial melting events preserved in a single migmatite dome. The main migmatitic foliation was originally subhorizontal and was subsequently folded by upright folds with a horizontal axis. Rare low-strain domains in nebulitic migmatites preserve an older folded migmatite fabric, indicating two partial melting events. Zircon from a paragneiss sampled in the migmatitic core yields Devonian (*ca.* 420–375 Ma) and Permian (*ca.* 270 Ma) ages, documenting a strong Permian reworking of the Devonian migmatite. During the Permian, a renewed extensional event resulted in local extensive remobilisation of the Devonian infrastructure (Sukhbaatar et al., 2022). The latter study indicates that the Permian migmatite fabric was folded by upright folds during the late Permian to Triassic. In essence, the two superposed Devonian-Carboniferous and Permian extensional and contractional cycles resulted in similar structures and metamorphism.

## 6.2. Deformation, metamorphism, and temporal evolution of the Gegetin Gol section

Phyllite of the Northern Domain grades into micaschist of the Central Domain, suggesting their derivation from the same Ordovician (*ca.* 460 Ma) sedimentary protolith (Kröner et al., 2010). A major tectonic boundary is identified at the contact between the micaschist and sillimanite gneiss (fig. 21).

### *6.2.1. Devonian-Carboniferous metamorphism and deformation*

In the studied micaschist, $M_{1\text{-mic}}$ corresponds to an increase of pressure initially associated with temperature increase, and then, either isothermal or related to a slight cooling (fig. 21). Furthermore, garnet 1 crystallised at low pressure and moderate temperature, indicating an elevated thermal state at the onset of $M_{1\text{-mic}}$. Monazite included in garnet 1 indicates the minimum Carboniferous age of this metamorphic event (*ca.* 340 Ma; fig. 19). Isothermal pressure increase can be tentatively explained by magma loading, whereby rapid magma over-accretion buries underlying rocks (Brown & Walker, 1993; Connop et al., 2024; Wells, 1980). However, the age of metamorphism, *ca.* 340 Ma or slightly older, correlates with the end rather than the peak of a major magmatic event in the Mongolian Altai (410–350 Ma, e.g., Cai et al., 2015). In addition, the 3–4 kbar pressure increase would require the emplacement of large batholiths, which are absent higher in the studied section.

In the Mongolian Altai, several authors reported an upright folding of high-temperature horizontal fabrics related to an early Carboniferous compression (Broussolle et al., 2015; Lehmann et al., 2017). In the studied section, Devonian migmatites (Y261A) may also evidence a thermal event shortly preceding the Carboniferous compression. In the context of a weak crust, crustal shortening results at broad distances in distributed thickening (e.g., Cagnard et al., 2006; Pitra et al., 2010; Schulmann et al., 2002). Therefore, the $M_{1\text{-Mic}}$ pressure increase could be explained by magma loading, homogeneous thickening of the crust, or a combination of both.

In this study, the fabrics associated with the Carboniferous compressional event were not observed in the micaschist, neither at the macro- nor at the micro-scale. However, an early metamorphic fabric in the micaschist preserved as sigmoidal inclusion trails in garnet 2 was reported by Sukhorukov et al. (2016), and here referred to as $S_{relic}$. The inclusion trails most likely represent the folded remnants of $S_{relic}$ trapped at the onset of the main deformation during the growth of garnet 2. These findings agree with the preservation of the early foliation deformed by recumbent folds in low-strain domains in otherwise mylonitic amphibolites (fig. 4D). The lack of relics of $S_{relic}$ fabric in the micaschist possibly results from grain coarsening of the matrix crystals during the prograde metamorphism, leading to complete obliteration of previous fabrics.

### *6.2.2. The Central Domain - Permian extensional shear zones*

In the micaschist samples, coarser garnet and staurolite porphyroblasts grew in the neck zones boudins during D2. Although Sukhorukov et al. (2016) showed a picture of staurolite porphyroblasts containing inclusion trails at high angle with the external fabric, our samples show the continuity of the internal and external foliation of staurolite (fig. 6A and E). Macroscopic field and microstructural observations are thus compatible with syn-tectonic growth of the Barrovian assemblages.

$M_{2\text{-Mic}}$ indicates an isobaric heating (fig. 21; Sukhorukov et al., 2016), a *P–T* path compatible with syn-metamorphic intrusions (e.g., Spear et al., 1984). Numerous granitoid sills are either parallel with the main metamorphic foliation $S_{main}$ (fig. 4A), boudinaged or folded, suggesting their syn-tectonic emplacement. Monazite included in syn-D2 garnet 2 and staurolite yield an early Permian U-Pb age (288 ±1.5 [6] Ma) similar to that of a foliated granite sheet of the Central Domain (296 ± 2 [6] Ma; Kröner et al., 2010), confirming the close temporal relationship between magmatism and short-lived metamorphism.

Sillimanite overprint typifies subsequent M3 decompression. Monazite located in domains recrystallised during M3 ages undistinguishable from that related to M2, emphasising the close progressive and short-lived nature of M2 and M3. This is also compatible with the zircon U-Pb age of *ca.* 290 Ma dike cutting the D2 fabric (fig. 20D).

In contrast to the prograde character of $S_{main}$ in the micaschist, $S_{main}$ in the sillimanite gneiss transposes a former migmatitic foliation (fig. 4D), indicating a major boundary between the two domains. In general, important grain-size variations occur in the micaschist and the sillimanite-gneiss. The grain-size variation is correlated to the intensity of $D_2$ transposition (compare fig. 4C and D), sug-

gesting important deformation gradients typical for strain partitioning (Bell, 1981). Strain gradients are generally concentrated in simple shear-dominated mylonite zones reworking the Central Domain ($S_{main\text{-}SZ}$ in fig. 21), as also mentioned by Sukhorukov et al. (2016). Recumbent folds ($F_{rec}$) preserved in low-strain domains (fig. 4E) are compatible with a dominant vertical shortening component. Field and microstructural observations can be collectively interpreted as $D_2$ deformation partitioning between low-strain pure shear-dominated domains and zones of intense simple shear (Bell & Rubenach, 1983). Altogether, the Central Domain can be interpreted as a highly partitioned normal shear zone where heat was presumably advected by magmatic pulse(s).

In general, spatial length and time scales of a thermal anomaly correlate well. For a typical crustal thermal diffusivity value ($10^{-6}$ $m^2s^{-1}$), a thermal anomaly smaller than the size of a normal crustal thickness (~30 km) lasts less than 10 Myr, and the resulting metamorphism may be regarded as 'short-lived' metamorphism (Viete & Lister, 2017). In the studied area several observations are compatible with local and short-lived thermal perturbation related to magmatic intrusions: 1) the sharp (3–5 km) metamorphic gradient between the fine-grained bi-phyllite and coarse sill-gneiss; 2) the correlation between the staurolite-kyanite and sillimanite isograds and the locations of intrusions (fig. 2); 3) the geochronological data for M2, M3 and syn- to post-tectonic indicating a 10 Myr maximum thermal event, between *ca.* 295–285 Ma. This is compatible with the preservation of compositional breaks at a scale of <50 µm in garnet (fig. 8), also suggesting that near-peak metamorphism was short-lived (likely <5–10 My; Caddick et al., 2010). Altogether, the data indicate a short-lived metamorphism largely driven by the thermal anomaly induced by the intrusions of multiple magmatic sheets and dikes in the extensional shear zone.

#### *6.2.3. Evolution of the Southern Domain*

The Southern Domain located in the footwall of the extensional shear zone underwent a polyphase evolution evidenced by distinct sets of leucosomes (fig. 5E), isoclinal folding of the migmatitic foliation (fig. 5D) and the variety of ages obtained in zircons with igneous textures (fig. 20). It is unclear whether the protolith of the g-ky-sill stromatic migmatites K263 and Y261B was an early Paleozoic or a Devonian sediment, for example the *ca.* 410 Ma age peak from zircon core in Y261B may represent the maximum depositional age of the protolith or the age of a partial melting during metamorphism. As such, the inclusion-rich garnet 1 documents an undated prograde metamorphism. The sharp optical discontinuity between garnet core and rim can be interpreted in terms of resorption, in which case the prograde metamorphism could be much older than the main Permian event M2.

The *ca.* 380–375 Ma thermal event documented by the diatexite Y261A corresponds to the protolith age of orthogneiss (*ca.* 360 Ma; Helo et al., 2006) and a partially molten tonalite gneiss (*ca.* 385 Ma; Kozakov et al., 2023). Carboniferous zircon core from the tonalite sill Y259 documents a subsequent thermal event, possibly magmatic. Such Devonian to early Carboniferous magmatic ages are typical for the Mongolian Altai (e.g., Burenjargal et al., 2012; Cai et al., 2015; de Hoÿm de Marien et al., 2025; Jiang et al., 2012).

The nature of the Permian metamorphism is documented by the g-ky-sill migmatite K263 sample indicating a suprasolidus nearly isothermal decompression from 9 to 4–7 kbar at 700–750 °C, followed by cooling below the solidus (fig. 21). The homogeneous Permian *ca.* 285 Ma date obtained in monazite related to kyanite, and syn-folial sillimanite and biotite indicate the age of the decompression and the development of a shallow-dipping foliation (fig. 21). Subsequent horizontal shortening is documented by upright folds with horizontal hinges (fig. 5A) while rare recumbent folds have an unclear origin.

### 6.3. Tectonic interpretation

Sukhorukov et al. (2016) previously interpreted the *P–T* path of the micaschists in terms of overthrusting without the addition of heat. This interpretation has a theoretical background (see England & Thompson, 1984), however, the isobaric heating in these numerical models results from a 20 Myr period of thermal relaxation before erosion begins. Ryan and Dewey (2019) quoted this initial condition as an important caveat of the model. Our data (fig. 21) indicate that isobaric heating is related to the emplacement of magma in a shear zone that accommodated the exhumation of migmatite. Exhumation of migmatite by a normal shear zone focusing the magmatic activity is a typical characteristic of metamorphic core complexes (Vanderhaeghe et al., 1999). In this context and agreement with the study of Sukhbaatar et al. (2022) and Lexa et al. (2025), our *P–T* data suggest that the studied location corresponds to a moderately deep section (10–20km) of a metamorphic core complex.

While the general tectonic context of this extension is not fully understood (see Hanžl et al., 2023; Kozlovsky et al., 2015 for contrasting interpretations), a Permian metamorphic core complex is compatible with the widespread occurrence of rift zones in Mongolia (Kovalenko & Chernov, 2008; fig. 1). The basins are filled with volcanoclastic series including bimodal volcanics (Kozlovsky et al., 2005) and continental sediments (e.g., Buriánek et al., 2012). All these elements argue in favour of a late Carboniferous to early Permian lithospheric extension localised along pre-existing tectonic boundaries (Kovalenko & Chernov, 2008) and partially molten domains (Lexa et al., 2025; Sukhbaatar et al., 2022). Late Carboniferous (*ca.* 320 Ma) mantle-derived gabbroic plutons near the study area suggest a contribution of the mantle to the Permian thermal event (Buriánek et al., 2016).

### 6.4. Metamorphic core complex, regional extension, and Barrovian metamorphism

A seminal study by Viete et al. (2010) demonstrated that lithospheric extension associated with magmatism can account for the regional Barrovian metamorphism of the

Scottish Highlands. According to the same study, the Barrovian sequence is located in the footwall of a detachment. This position contrasts with the structural position of the Barrovian metamorphic sequence studied here, located within the detachment zone, close to the hangingwall low-grade rocks. Below, we propose a new petrological and tectonic model to account for our observations.

Field studies in collapsed orogens indicate two successive regimes of extension, with the initial development of metamorphic core complexes evolving later into a wide rift system (Coney, 1987; Gautier et al., 1999). During the core complex stage, extension is controlled by a main detachment fault rooted in the ductile crust (e.g., Brun et al., 2018; Brun & van den Driessche, 1994). It remains so as long as the flow of the ductile crust towards the growing core complex accommodates the horizontal stretching (Tirel et al., 2006). In this context, the ductile crust is exhumed below the detachment, whereas little vertical movement occurs in the hangingwall. As the extension proceeds, active thinning of the crust above the Moho (Tirel et al., 2008) promotes decompression melting of the mantle (e.g., Sonder et al., 1987), inducing widespread crustal melting and magmatism (Poujol et al., 2016; Vanderhaeghe et al., 1999; Wernicke et al., 1987). The growth of a metamorphic core complex results in rapid exhumation of a large volume of hot lower crust to the upper crust (Teyssier & Whitney, 2002), inducing isothermal decompression and heat advection in shallow crustal levels (Rey et al., 2009a, 2009b). The combined effect of exhumation of the hot lower crust and syntectonic magma intrusions in the detachment during the growth of the dome can effectively advect heat vertically and laterally and influence the thermal evolution of the metamorphic envelope. To construct the petrological model of development of the Barrovian metamorphism in an extensional shear zone, we overlaid our *P–T* data on the model of asymmetric growth of a core complex resulting from a rolling hinge process of Brun and van den Driessche (1994).

At the initial stage (fig. 22A), *P–T* conditions for the micaschists (blue arrow in *P–T* diagram) and migmatite (orange arrow) align along an apparent thermal gradient of 20–25 °C/km. The micaschists (blue dot in tectonic sketches) belong to the ductile middle crust, and the migmatite (orange dot) to the partially molten lower crust. A normal fault initiates at 60° in the upper crust and progressively flattens in the ductile middle crust down to a *décollement* layer located at the boundary with the lower crust. Upward motion of the footwall causes an equivalent uplift of migmatite juxtaposed to the hangingwall ductile middle crust of the hangingwall, where heat can be transferred laterally by conduction. During this stage, the migmatite cools down while the middle crust heats up. The shear zone localises the flow of magma, as shown by the abundant granitoid dikes and sheets observed in the Central Domain (fig. 21). Structurally and magmatically induced advection of heat results in upward and lateral migration of the temperature isograd, and formation of an abnormally hot, thermally perturbed wedge in the hangingwall of the fault (fig. 22A).

As extension proceeds (fig. 22B), rollunder occurs in the footwall and causes a rotation of the fault to a lower angle (e.g., Buck, 1988; Wernicke & Axen, 1988). The segment of the fault that becomes flat no longer accommodates extension, and a new fault is created in the hangingwall (Brun & van den Driessche, 1994; Buck, 1988). Slices of rocks from the hangingwall are thus transferred in the normal shear zone; in turn, the thermally perturbed wedge progresses in the hangingwall undergoing isobaric heating. At this stage, the magma emplaced in the shear zone certainly plays a critical role in heating the hangingwall. Meanwhile, partially molten rocks flow towards the dome where melts crystallise in the dome apex.

Continued extension causes further exhumation of migmatite and further migration of the active shear zone (fig. 22C). Slices of the brittle and ductile crust from the hangingwall are incorporated into the footwall of the shear zone, resulting in exhumation of the ductile crust that was previously heated. Eventually, the dome migmatites and shear zone micaschists are juxtaposed (fig. 22D).

The inset in figure 22D shows an idealised geological section reproducing our observations at the final stage of the model. The high-strain zone controlled the position of the magmatic intrusions, which, in turn, controlled the location of the metamorphic gradient developed between the phyllites (in green) and the variably deformed migmatites (orange and brown). The core of the shear zone hosts the micaschists (in blue) that exhibit the relics of a Barrovian sequence formed during the earlier extensional stages.

## 7. CONCLUSION

In the valley of the Gegetin Gol river in the Mongolian Altai, a sharp partial Barrovian-type field metamorphic gradient intervenes between low-grade phyllite and high-grade migmatite zones. The Barrovian assemblages in micaschists do not result from a long-term thermal relaxation during thickening, but instead from 50–100 °C isobaric heating marked by a transition from garnet-chlorite to garnet-staurolite or garnet-staurolite-kyanite assemblages. Heating and subsequent decompression in the field of sillimanite were coeval with the activity of a normal shear zone which focused numerous granitoid syntectonic sheets and dikes. The shear zone accommodated the exhumation of lower crustal rocks typified by the decomposition of kyanite to sillimanite in migmatite. Monazite from the metamorphic rocks and zircon from the magmatic ones indicate the early Permian age (*ca.* 295–285 Ma) of extension and support a short-lived (~10 Myr) thermal event in the micaschists. The main tectonic contact located between retrogressed migmatite and prograde micaschist indicates that the micaschist initially belonged to the hangingwall of the shear zone, was subsequently incorporated into it, and consequently partially exhumed. This sequence can be explained by the progressive development of a detachment related to the formation of a metamorphic core complex. This study suggests that envelopes of metamorphic core complexes are prone to develop syn-extensional Barrovian metamorphic sequences.

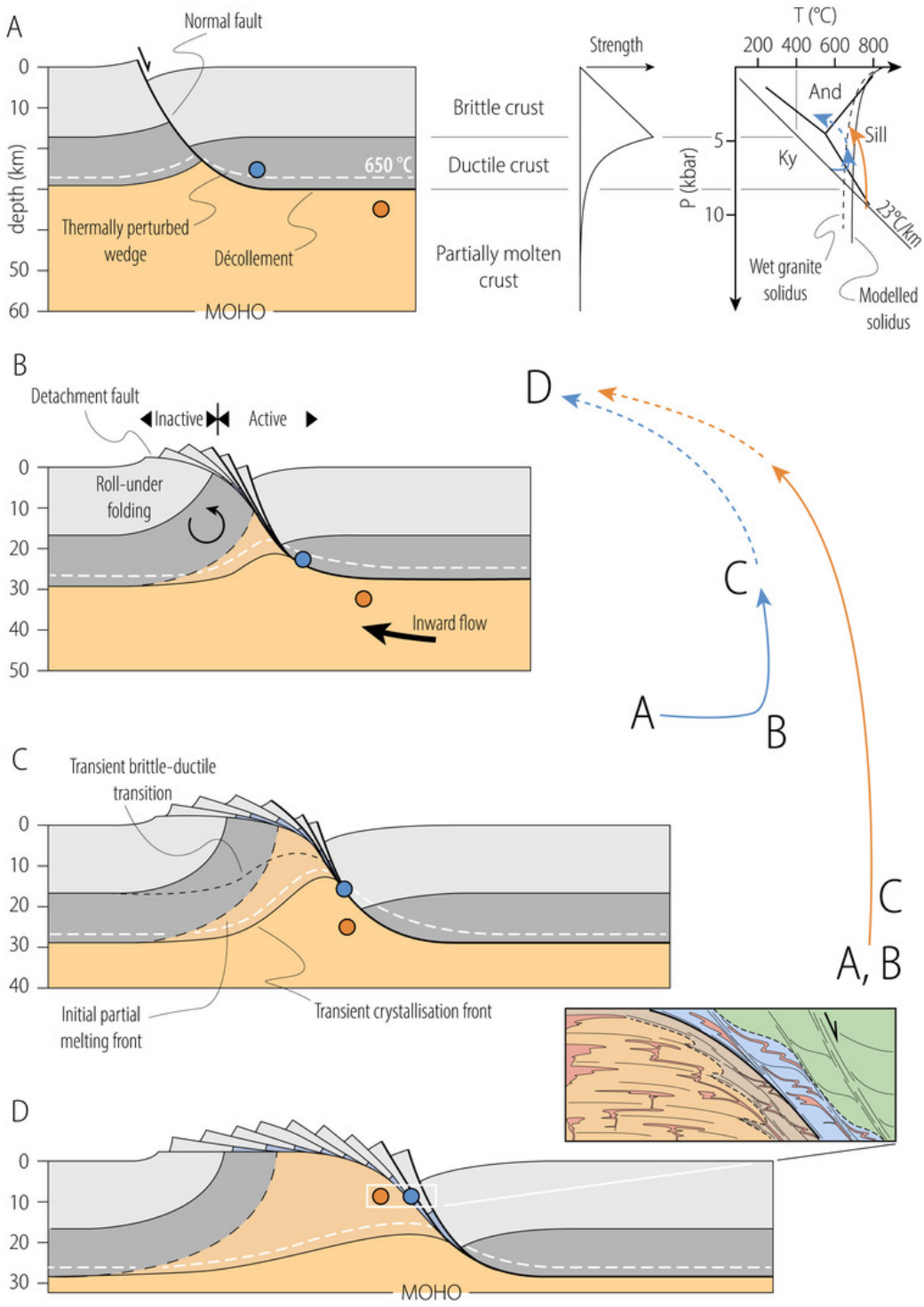


**Figure 22. Petrological model for the development of a Barrovian metamorphic sequence in a hangingwall of a detachment above a growing metamorphic core complex. Structural model after Brun and van den Driessche (1994). The brittle-ductile transition in the model corresponds to the isotherm 400 °C. The isotherm 650 °C is shown for reference, the partial melting front roughly corresponds to the 680 °C isotherm. Note that the inevitable rheological changes related to the evolution of the thermal structure are not taken into account. The large arrows are enlargements of the arrows in the P–T diagram. The colors of the zoomed-in sketch in (D) match those of the previous figure.**

ACKNOWLEDGMENTS

L. de Hoÿm de Marien dedicates this article to the memory of J. P. Brun, with whom a simple question was always the pretext for a rich discussion. This has proven invaluable

during the redaction of this article. The implication of P. Pitra, J. van den Driessche, and E. Moulas through discussion is sincerely acknowledged. We thank warmly D. Viete and A. Smye for constructive reviews, as well as M. Brandon and J. Ague for careful editorial handling. This work was supported by the Czech Science Foundation (GACR EXPRO 19-27682X), internal grant of the Czech Geological Survey, Czechia (number 329805), and the International Partnership Program of the Chinese Academy of Sciences (Grant/Award Number: 132744KYSB20190039).

## AUTHOR CONTRIBUTIONS

**Luc de Hoÿm de Marien** – Data collection, modeling, visualization, original draft, review & editing. **Pavla Štípská** – Methodology, supervision, modeling, original draft, review & editing. **Karel Schulmann** – Funding acquisition, conceptualisation, supervision, original draft, review & editing. **Andrew Kylander-Clark** – Data collection, review & editing. **Ondrej Lexa** – Funding acquisition, conceptualisation, review & editing. **Yingde Jiang** – Data collection, review & editing. **Petr Jeřábek** – Data collection, review & editing. **Martin Racek** – Data collection, review & editing. **David Buriánek** – Data collection, review & editing.

## DATA AND SUPPLEMENTARY INFORMATION

https://data.mendeley.com/datasets/5pjt9gdbyv/1

**Figure S1.** FigS1_Petrography_SamplesZrc_small.jpg – Field photographs and thin section photomicrographs of geochronological samples dated by U–Pb zircon LA–ICP–MS method.

**Table S1.** TableS1_MineralChemistry.xlsx – Representative mineral chemical analyses.

**Table S2.** TableS2_U-Th-Pb_TE_Mz.xlsx – Monazite U–Th–Pb and Trace Element data.

**Table S3.** TableS3_U-Pb_Zrn.xlsx – Zircon U–Pb data.

**Editor: Mark T. Brandon, Associate Editor: Jay J. Ague**

Submitted: August 07, 2024 EST. Accepted: December 31, 2025 EST. Published: February 09, 2026 EST.

# REFERENCES


Ague, J. J., & Baxter, E. F. (2007). Brief thermal pulses during mountain building recorded by Sr diffusion in apatite and multicomponent diffusion in garnet. *Earth and Planetary Science Letters*, *261*(3–4), 500–516. https://doi.org/10.1016/j.epsl.2007.07.017

Aguilar, C., Štípská, P., Schulmann, K., Kylander-Clark, A. R. C., Lexa, O., Sukhbaatar, T., Peřestý, V., Jiang, Y., & Hanžl, P. (2024). Carboniferous Barrovian to Permian Buchan-type metamorphic cycles in the Mongolian Altai Zone: Implication for pressure cycles in accretionary orogens. *Journal of Metamorphic Geology*, *42*(7), 979–1033. https://doi.org/10.1111/jmg.12777

Aleinikoff, J. N., Schenck, W. S., Plank, M. O., Srogi, L., Fanning, C. M., Kamo, S. L., & Bosbyshell, H. (2006). Deciphering igneous and metamorphic events in high-grade rocks of the Wilmington Complex, Delaware: Morphology, cathodoluminescence and backscattered electron zoning, and SHRIMP U-Pb geochronology of zircon and monazite. *Geological Society of America Bulletin*, *118*(1–2), 39–64. https://doi.org/10.1130/B25659.1

Badarch, G., Dickson Cunningham, W., & Windley, B. F. (2002). A new terrane subdivision for Mongolia: Implications for the Phanerozoic crustal growth of Central Asia. *Journal of Asian Earth Sciences*, *21*(1), 87–110. https://doi.org/10.1016/S1367-9120(02)00017-2

Barrow, G. (1893). On an Intrusion of Muscovite-biotite Gneiss in the South-eastern Highlands of Scotland, and its accompanying Metamorphism. *Quarterly Journal of the Geological Society of London*, *49*(1–4), 330–358. https://doi.org/10.1144/GSL.JGS.1893.049.01-04.52

Bell, T. H. (1981). Foliation development—The contribution, geometry and significance of progressive, bulk, inhomogeneous shortening. *Tectonophysics*, *75*(3–4), 273–296. https://doi.org/10.1016/0040-1951(81)90278-X

Bell, T. H., & Rubenach, M. J. (1983). Sequential porphyroblast growth and crenulation cleavage development during progressive deformation. *Tectonophysics*, *92*(1–3), 171–194. https://doi.org/10.1016/0040-1951(83)90089-6

Bibikova, E. V. (1992). U-Pb ages for polymetamorphic complexes on the southern flank of the Mongolian and Gobi Altai. *Geotectonics*, *26*, 166–172.

Bosse, V., & Villa, I. M. (2019). Petrochronology and hygrochronology of tectono-metamorphic events. *Gondwana Research*, *71*, 76–90. https://doi.org/10.1016/j.gr.2018.12.014

Broussolle, A., Štípská, P., Lehmann, J., Schulmann, K., Hacker, B. R., Holder, R., Kylander-Clark, A. R. C., Hanžl, P., Racek, M., Hasalová, P., Lexa, O., Hrdličková, K., & Buriánek, D. (2015). P–T–t–D record of crustal-scale horizontal flow and magma-assisted doming in the SW Mongolian Altai. *Journal of Metamorphic Geology*, *33*(4), 359–383. https://doi.org/10.1111/jmg.12124

Broussolle, A., Sun, M., Schulmann, K., Guy, A., Aguilar, C., Štípská, P., Jiang, Y., Yu, Y., & Xiao, W. (2019). Are the Chinese Altai "terranes" the result of juxtaposition of different crustal levels during Late Devonian and Permian orogenesis? *Gondwana Research*, *66*, 183–206. https://doi.org/10.1016/j.gr.2018.11.003

Brown, E. H., & Walker, N. W. (1993). A magma-loading model for Barrovian metamorphism in the southeast Coast Plutonic Complex,British Columbia and Washington. *Geological Society of America Bulletin*, *105*(4), 479–500. https://doi.org/10.1130/0016-7606(1993)105

Brun, J.-P., Sokoutis, D., Tirel, C., Gueydan, F., Van den Driessche, J., & Beslier, M.-O. (2018). Crustal versus mantle core complexes. *Tectonophysics*, *746*, 22–45. https://doi.org/10.1016/j.tecto.2017.09.017

Brun, J.-P., & van den Driessche, J. (1994). Extensional gneiss domes and detachment fault systems; structure and kinematics. *Bulletin de La Société Géologique de France*, *165*(6), 519–530.

Buck, W. R. (1988). Flexural rotation of normal faults. *Tectonics*, *7*(5), 959–973. https://doi.org/10.1029/TC007i005p00959

Burenjargal, U., Okamoto, A., Kuwatani, T., Sakata, S., Hirata, T., & Tsuchiya, N. (2014). Thermal evolution of the Tseel terrane, SW Mongolia and its relation to granitoid intrusions in the Central Asian Orogenic Belt. *Journal of Metamorphic Geology*, *32*(7), 765–790. https://doi.org/10.1111/jmg.12090

Burenjargal, U., Okamoto, A., Meguro, Y., & Tsuchiya, N. (2012). An exhumation pressure–temperature path and fluid activities during metamorphism in the Tseel terrane, SW Mongolia: Constraints from aluminosilicate-bearing quartz veins and garnet zonings in metapelites. *Journal of Asian Earth Sciences*, *54–55*, 214–229. https://doi.org/10.1016/j.jseaes.2012.04.017

Burg, J. P., Leyreloup, A., Marchand, J., & Matte, P. (1984). Inverted metamorphic zonation and large-scale thrusting in the Variscan Belt: An example in the French Massif Central. *Geological Society, London, Special Publications*, *14*(1), 47–61. https://doi.org/10.1144/GSL.SP.1984.014.01.05

Buriánek, D., Hanžl, P., Budil, P., & Gerdes, A. (2012). Evolution of the Early Permian volcanic-plutonic complex in the western part of the Permian Gobi-Altay Rift (Khar Argalant Mts., SW Mongolia). *Journal of Geosciences*, *57*(2), 105–126. https://doi.org/10.3190/jgeosci.116

Buriánek, D., Janoušek, V., Hanžl, P., Jiang, Y., Schulmann, K., Lexa, O., & Altanbaatar, B. (2016). Petrogenesis of the Late Carboniferous Sagsai Pluton in the SE Mongolian Altai. *Journal of Geosciences*, *61*(1), 67–92. https://doi.org/10.3190/jgeosci.207

Buriánek, D., Schulmann, K., Hrdličková, K., Hanžl, P., Janoušek, V., Gerdes, A., & Lexa, O. (2017). Geochemical and geochronological constraints on distinct Early-Neoproterozoic and Cambrian accretionary events along southern margin of the Baydrag Continent in western Mongolia. *Gondwana Research*, *47*, 200–227. https://doi.org/10.1016/j.gr.2016.09.008

Buriánek, D., Soejono, I., Schulmann, K., Janoušek, V., Hanžl, P., Čáp, P., Bold, U., Svojtka, M., Collett, S., & Žáček, V. (2022). Subduction-controlled temporal and spatial variations in early Palaeozoic sedimentary and volcanic record of the Mongol-Altai Domain. *Journal of Asian Earth Sciences*, *230*, 105182. https://doi.org/10.1016/j.jseaes.2022.105182

Caddick, M. J., Konopásek, J., & Thompson, A. B. (2010). Preservation of Garnet Growth Zoning and the Duration of Prograde Metamorphism. *Journal of Petrology*, *51*(11), 2327–2347. https://doi.org/10.1093/petrology/egq059

Cagnard, F., Durrieu, N., Gapais, D., Brun, J.-P., & Ehlers, C. (2006). Crustal thickening and lateral flow during compression of hot lithospheres, with particular reference to Precambrian times. *Terra Nova*, *18*(1), 72–78. https://doi.org/10.1111/j.1365-3121.2005.00665.x

Cai, K., Sun, M., Jahn, B. -m., Xiao, W., Yuan, C., Long, X., Chen, H., & Tumurkhuu, D. (2015). A synthesis of zircon U–Pb ages and Hf isotopic compositions of granitoids from Southwest Mongolia: Implications for crustal nature and tectonic evolution of the Altai Superterrane. *Lithos*, *232*, 131–142. https://doi.org/10.1016/j.lithos.2015.06.014

Coney, P. J. (1987). The regional tectonic setting and possible causes of Cenozoic extension in the North American Cordillera. *Geological Society, London, Special Publications*, *28*(1), 177–186. https://doi.org/10.1144/GSL.SP.1987.028.01.13

Connolly, J. A. D., & Cesare, B. (1993). C-O-H-S fluid composition and oxygen fugacity in graphitic metapelites. *Journal of Metamorphic Geology*, *11*(3), 379–388. https://doi.org/10.1111/j.1525-1314.1993.tb00155.x

Connop, C. H., Smye, A. J., Garber, J. M., Moser, A. C., Caddick, M. J., & Vervoort, J. D. (2024). Assembly of lower continental crust: A garnet Lu-Hf petrochronological investigation of the Ivrea-Verbano Zone, Italy. *Earth and Planetary Science Letters*, *634*, 118677. https://doi.org/10.1016/j.epsl.2024.118677

Corrie, S. L., & Kohn, M. J. (2008). Trace-element distributions in silicates during prograde metamorphic reactions: Implications for monazite formation. *Journal of Metamorphic Geology*, *26*(4), 451–464. https://doi.org/10.1111/j.1525-1314.2008.00769.x

de Hoÿm de Marien, L., Janoušek, V., Schulmann, K., Hanžl, P., Míková, J., Hora, J. M., Racek, M., Lexa, O., Sukhbaatar, T., Buriánek, D., & Aguilar, C. (2025). Middle Devonian–Carboniferous crustal differentiation promoted by hydrous plume-related magmatism along the Paleo-Pacific active margin: A case study of the Gashun Nuur Complex in the Mongolian Altai. *Gondwana Research*, *147*, 36–62. https://doi.org/10.1016/j.gr.2025.05.025

Didier, A., Bosse, V., Cherneva, Z., Gautier, P., Georgieva, M., Paquette, J. L., & Gerdjikov, I. (2014). Syn-deformation fluid-assisted growth of monazite during renewed high-grade metamorphism in metapelites of the Central Rhodope (Bulgaria, Greece). *Chemical Geology*, *381*, 206–222. https://doi.org/10.1016/j.chemgeo.2014.05.020

England, P. C., & Thompson, A. B. (1984). Pressure—Temperature—Time Paths of Regional Metamorphism I. Heat Transfer during the Evolution of Regions of Thickened Continental Crust. *Journal of Petrology*, *25*(4), 894–928. https://doi.org/10.1093/petrology/25.4.894

Florence, F. P., & Spear, F. S. (1991). Effects of diffusional modification of garnet growth zoning on P-T path calculations. *Contributions to Mineralogy and Petrology*, *107*(4), 487–500. https://doi.org/10.1007/BF00310683

Gautier, P., Brun, J.-P., Moriceau, R., Sokoutis, D., Martinod, J., & Jolivet, L. (1999). Timing, kinematics and cause of Aegean extension: A scenario based on a comparison with simple analogue experiments. *Tectonophysics*, *315*(1–4), 31–72. https://doi.org/10.1016/S0040-1951(99)00281-4

Gibson, T. M., Myrow, P. M., Macdonald, F. A., Minjin, C., & Gehrels, G. E. (2013). Depositional history, tectonics, and detrital zircon geochronology of Ordovician and Devonian strata in southwestern Mongolia. *Geological Society of America Bulletin*, *125*(5–6), 877–893. https://doi.org/10.1130/B30746.1

Godet, A., Raimondo, T., & Guilmette, C. (2022). Atoll garnet: Insights from LA-ICP-MS trace element mapping. *Contributions to Mineralogy and Petrology*, *177*(6), 57. https://doi.org/10.1007/s00410-022-01924-7

Hanžl, P., & Aichler, J. (2007). *Geological Survey of the Mongolian Altay at a scale 1: 50,000 (Zamtyn Nuruu – 50). Final report of the International Development Cooperation project of the Czech Republic*. Czech Geological Survey, Brno & MRPAM, Ulaanbaatar.

Hanžl, P., Janoušek, V., Hrdličková, K., Buriánek, D., Gerel, O., Altanbaatar, B., Hora, J. M., & Čoupek, P. (2023). From magmatic arc to a post-accretionary setting: Late Palaeozoic granitoid plutons in the northwestern Trans-Altai Zone, Mongolia. *Journal of Geosciences*, *68*(1), 25–66. https://doi.org/10.3190/jgeosci.366

Hanžl, P., Schulmann, K., anoušek, V., Lexa, O., Hrdličková, K., Jiang, Y., Buriánek, D., Altanbaatar, B., Ganchuluun, T., & Erban, V. (2016). Making continental crust: Origin of Devonian orthogneisses from SE Mongolian Altai. *Journal of Geosciences*, *61*(1), 25–50. https://doi.org/10.3190/jgeosci.206

Hanžl, P., Uhrová, L., Hrdličková, K., Schulmann, K., Buriánek, D., Gansukh, O., & Míková, J. (2024). Late Ordovician magmatic pulse in the Tugrug Group, the Gobi Altai Zone, SW Mongolia. *Journal of Geosciences*, *69*(1), 31–19. https://doi.org/10.3190/jgeosci.385

Helo, C., Hegner, E., Kröner, A., Badarch, G., Tomurtogoo, O., Windley, B. F., & Dulski, P. (2006). Geochemical signature of Paleozoic accretionary complexes of the Central Asian Orogenic Belt in South Mongolia: Constraints on arc environments and crustal growth. *Chemical Geology*, *227*(3–4), 236–257. https://doi.org/10.1016/j.chemgeo.2005.10.003

Holland, T. J. B., Green, E. C. R., & Powell, R. (2022). A thermodynamic model for feldspars in $KAlSi_3O_8$–$NaAlSi_3O_8$–$CaAl_2Si_2O_8$ for mineral equilibrium calculations. *Journal of Metamorphic Geology*, *40*(4), 587–600. https://doi.org/10.1111/jmg.12639

Holland, T. J. B., & Powell, R. (2011). An improved and extended internally consistent thermodynamic dataset for phases of petrological interest, involving a new equation of state for solids. *Journal of Metamorphic Geology*, *29*(3), 333–383. https://doi.org/10.1111/j.1525-1314.2010.00923.x

Jackson, S. E., Pearson, N. J., Griffin, W. L., & Belousova, E. A. (2004). The application of laser ablation-inductively coupled plasma-mass spectrometry to in situ U–Pb zircon geochronology. *Chemical Geology*, *211*(1–2), 47–69. https://doi.org/10.1016/j.chemgeo.2004.06.017

Jamieson, R. A., Beaumont, C., Fullsack, P., & Lee, B. (1998). Barrovian regional metamorphism: Where's the heat? *Geological Society, London, Special Publications*, *138*(1), 23–51. https://doi.org/10.1144/GSL.SP.1996.138.01.03

Janoušek, V., Jiang, Y., Buriánek, D., Schulmann, K., Hanžl, P., Soejono, I., Kröner, A., Altanbaatar, B., Erban, V., Lexa, O., Ganchuluun, T., & Košler, J. (2018). Cambrian–Ordovician magmatism of the Ikh-Mongol Arc System exemplified by the Khantaishir Magmatic Complex (Lake Zone, south–central Mongolia). *Gondwana Research*, *54*, 122–149. https://doi.org/10.1016/j.gr.2017.10.003

Jian, P., Kröner, A., Jahn, B. -m., Windley, B. F., Shi, Y., Zhang, W., Zhang, F., Miao, L., Tomurhuu, D., & Liu, D. (2014). Zircon dating of Neoproterozoic and Cambrian ophiolites in West Mongolia and implications for the timing of orogenic processes in the central part of the Central Asian Orogenic Belt. *Earth-Science Reviews*, *133*, 62–93. https://doi.org/10.1016/j.earscirev.2014.02.006

Jiang, Y., Schulmann, K., Kröner, A., Sun, M., Lexa, O., Janoušek, V., Buriánek, D., Yuan, C., & Hanžl, P. (2017). Neoproterozoic-Early Paleozoic Peri-Pacific Accretionary Evolution of the Mongolian Collage System: Insights From Geochemical and U-Pb Zircon Data From the Ordovician Sedimentary Wedge in the Mongolian Altai. *Tectonics*, *36*(11), 2305–2331. https://doi.org/10.1002/2017TC004533

Jiang, Y., Schulmann, K., Sun, M., Štípská, P., Guy, A., Janoušek, V., Lexa, O., & Yuan, C. (2016). Anatexis of accretionary wedge, Pacific-type magmatism, and formation of vertically stratified continental crust in the Altai Orogenic Belt. *Tectonics*, *35*(12), 3095–3118. https://doi.org/10.1002/2016TC004271

Jiang, Y., Schulmann, K., Sun, M., Weinberg, R. F., Štípská, P., Li, P. F., Zhang, J., Chopin, F., Wang, S., Xia, X. P., & Xiao, W. J. (2019). Structural and Geochronological Constraints on Devonian Suprasubduction Tectonic Switching and Permian Collisional Dynamics in the Chinese Altai, Central Asia. *Tectonics*, *38*(1), 253–280. https://doi.org/10.1029/2018TC005231

Jiang, Y., Štípská, P., Schulmann, K., Aguilar, C., Wang, S., Anczkiewicz, R., Zhang, J., Li, P., & Chopin, F. (2022). Barrovian and Buchan metamorphic series in the Chinese Altai: P–T–t– D evolution and tectonic implications. *Journal of Metamorphic Geology*, *40*(4), 823–857. https://doi.org/10.1111/jmg.12647

Jiang, Y., Štípská, P., Sun, M., Schulmann, K., Zhang, J., Wu, Q. H., Long, X. P., Yuan, C., Racek, M., Zhao, G. C., & Xiao, W. J. (2015). Juxtaposition of Barrovian and migmatite domains in the Chinese Altai: A result of crustal thickening followed by doming of partially molten lower crust. *Journal of Metamorphic Geology*, *33*(1), 45–70. https://doi.org/10.1111/jmg.12110

Jiang, Y., Sun, M., Kröner, A., Tumurkhuu, D., Long, X., Zhao, G., Yuan, C., & Xiao, W. (2012). The high-grade Tseel Terrane in SW Mongolia: An Early Paleozoic arc system or a Precambrian sliver? *Lithos*, *142–143*, 95–115. https://doi.org/10.1016/j.lithos.2012.02.016

Jiang, Y., Sun, M., Zhao, G., Yuan, C., Xiao, W., Xia, X., Long, X., & Wu, F. (2010). The 390 Ma high-T metamorphic event in the Chinese Altai: A consequence of ridge-subduction? *American Journal of Science*, *310*(10), 1421–1452. https://doi.org/10.2475/10.2010.08

Jiang, Y., Sun, M., Zhao, G., Yuan, C., Xiao, W., Xia, X., Long, X., & Wu, F. (2011). Precambrian detrital zircons in the Early Paleozoic Chinese Altai: Their provenance and implications for the crustal growth of central Asia. *Precambrian Research*, *189*(1–2), 140–154. https://doi.org/10.1016/j.precamres.2011.05.008

Kepezhinskas, P. K., Kepezhinskas, K. B., & Pukhtel, I. S. (1991). Lower Paleozoic oceanic crust in Mongolian Caledonides: SM-ND isotope and trace element data. *Geophysical Research Letters*, *18*(7), 1301–1304. https://doi.org/10.1029/91GL01643

Khukhuudei, U., Kusky, T., Otgonbayar, O., & Wang, L. (2020). The Early Palaeozoic mega-thrusting of the Gondwana-derived Altay–Lake zone in western Mongolia: Implications for the development of the Central Asian Orogenic Belt and Paleo-Asian Ocean evolution. *Geological Journal*, *55*(3), 2129–2149. https://doi.org/10.1002/gj.3753

Kohn, M. J. (2014). Himalayan Metamorphism and Its Tectonic Implications. *Annual Review of Earth and Planetary Sciences*, *42*(1), 381–419. https://doi.org/10.1146/annurev-earth-060313-055005

Kohn, M. J., & Malloy, M. A. (2004). Formation of monazite via prograde metamorphic reactions among common silicates: Implications for age determinations. *Geochimica et Cosmochimica Acta*, *68*(1), 101–113. https://doi.org/10.1016/S0016-7037(03)00258-8

Kong, L.-Z., Jiang, Y., Schulmann, K., Zhang, J., Weinberg, R. F., Sun, M., Wang, S., Shu, T., & Ning, J. (2022). Petrostructural and Geochronological Constraints on Devonian Extension-Shortening Cycle in the Chinese Altai: Implications for Retreating-Advancing Subduction. *Tectonics*, *41*(9), e2021TC007195. https://doi.org/10.1029/2021TC007195

Kong, L.-Z., Jiang, Y.-D., Li, P.-F., Collett, S., & Xiao, M. (2023). Devonian subduction retreat recorded in the Chinese Altai Orogen: Petro-structural and geochronological constraints from orogenic lower crust migmatite-granite complexes. *Journal of Asian Earth Sciences*, *244*, 105540. https://doi.org/10.1016/j.jseaes.2023.105540

Kovalenko, D. V., & Chernov, E. E. (2008). Paleomagnetism of Carboniferous-Permian and early jurassic geological complexes in Mongolia. *Izvestiya, Physics of the Solid Earth*, *44*(5), 427–441. https://doi.org/10.1134/S1069351308050078

Kozakov, I. K. (2002). Hercynian granulites of Mongolian and Gobian Altai: Geodynamic setting and formation conditions. *Doklady Earth Sciences*, *386*, 781–785.

Kozakov, I. K., Anosova, M. O., Kirnozova, T. I., Plotkina, Y. V., Tolmacheva, E. V., & Erdenezhargal, C. (2023). Polymetamorphism in the Geological Development of the South Altai Metamorphic Belt, Central Asian Foldbelt. *Stratigraphy and Geological Correlation*, *31*(S1), S1–S16. https://doi.org/10.1134/S0869593824010040

Kozakov, I. K., Didenko, A. N., Azimov, P. Y., Kirnozova, T. I., Sal'nikova, E. B., Anisimova, I. V., & Erdenejargal, C. (2011). Geodynamic settings and formation conditions of crystalline complexes in the south Altai and south Gobi metamorphic belts. *Geotectonics*, *45*(3), 174–194. https://doi.org/10.1134/S0016852111030022

Kozakov, I. K., Kirnozova, T. I., & Plotkina, Y. V. (2009). Age assessments for siliciclastic metasediments of the Bodonchin tectonic sheet, the South Altai metamorphic belt. *Stratigraphy and Geological Correlation*, *17*(1), 36–42. https://doi.org/10.1134/S0869593809010031

Kozakov, I. K., Kozlovsky, A. M., Yarmolyuk, V. V., Kirnozova, T. I., Fugzan, M. M., Oyunchimeg, T., & Erdenezhargal, C. (2019). Geodynamic Environments of the Origin of Poly- and Monometamorphic Complexes in the Southern Altai Metamorphic Belt, Central Asian Orogenic Belt. *Petrology*, *27*(3), 223–242. https://doi.org/10.1134/S0869591119030032

Kozlovsky, A. M., Yarmolyuk, V. V., Sal'nikova, E. B., Savatenkov, V. M., & Kovalenko, V. I. (2005). Age of Bimodal and Alkali Granite Magmatism of the Gobi–Tien Shan Rift Zone, Tost Range, Southern Mongolia. *Petrology*, *13*(2), 197–203.

Kozlovsky, A. M., Yarmolyuk, V. V., Salnikova, E. B., Travin, A. V., Kotov, A. B., Plotkina, J. V., Kudryashova, E. A., & Savatenkov, V. M. (2015). Late Paleozoic anorogenic magmatism of the Gobi Altai (SW Mongolia): Tectonic position, geochronology and correlation with igneous activity of the Central Asian Orogenic Belt. *Journal of Asian Earth Sciences*, *113*, 524–541. https://doi.org/10.1016/j.jseaes.2015.01.013

Kröner, A., Lehmann, J., Schulmann, K., Demoux, A., Lexa, O., Tomurhuu, D., Stipska, P., Liu, D., & Wingate, M. T. D. (2010). Lithostratigraphic and geochronological constraints on the evolution of the Central Asian Orogenic Belt in SW Mongolia: Early Paleozoic rifting followed by late Paleozoic accretion. *American Journal of Science*, *310*(7), 523–574. https://doi.org/10.2475/07.2010.01

Kulhánek, J., Faryad, S. W., Jedlicka, R., & Svojtka, M. (2021). Dissolution and Reprecipitation of Garnet during Eclogite-facies Metamorphism; Major and Trace Element Transfer during Atoll Garnet Formation. *Journal of Petrology*, *62*(11), egab077. https://doi.org/10.1093/petrology/egab077

Kylander-Clark, A. R. C., Hacker, B. R., & Cottle, J. M. (2013). Laser-ablation split-stream ICP petrochronology. *Chemical Geology*, *345*, 99–112. https://doi.org/10.1016/j.chemgeo.2013.02.019

Lamb, M. A., & Badarch, G. (1997). Paleozoic Sedimentary Basins and Volcanic-Arc Systems of Southern Mongolia: New Stratigraphic and Sedimentologic Constraints. *International Geology Review*, *39*(6), 542–576. https://doi.org/10.1080/00206819709465288

Le Fort, P. (1975). Himalayas: The collided range. Present knowledge of the continental arc. *American Journal of Science*, *275-A*, 1–44.

Lehmann, J., Schulmann, K., Lexa, O., Corsini, M., Kroner, A., Stipska, P., Tomurhuu, D., & Otgonbator, D. (2010). Structural constraints on the evolution of the Central Asian Orogenic Belt in SW Mongolia. *American Journal of Science*, *310*(7), 575–628. https://doi.org/10.2475/07.2010.02

Lehmann, J., Schulmann, K., Lexa, O., Závada, P., Štípská, P., Hasalová, P., Belyanin, G., & Corsini, M. (2017). Detachment folding of partially molten crust in accretionary orogens: A new magma-enhanced vertical mass and heat transfer mechanism. *Lithosphere*, *9*(6), 889–909. https://doi.org/10.1130/L670.1

Lexa, O. (2017). *PyPSbuilder—THERMOCALC front-end for constructing P–T pseudosections* (2.1.3). GitHub repository. https://github.com/ondrolexa/pypsbuilder

Lexa, O., Jeřábek, P., Schulmann, K., Racek, M., Jiang, Y., Kylander-Clark, A. R. C., Míková, J., & Spikings, R. (2025). Two Cycles of Devonian–Triassic Extension and Compression in the Altai Accretionary Wedge: Insights From Tsogt Core Complex. *Tectonics*, *44*(12), e2025TC008950. https://doi.org/10.1029/2025TC008950

Ludwig, K. R. (1998). On the Treatment of Concordant Uranium-Lead Ages. *Geochimica et Cosmochimica Acta*, *62*(4), 665–676. https://doi.org/10.1016/S0016-7037(98)00059-3

March, S., Hand, M., Morrissey, L., & Kelsey, D. (2024). The inhibited response of accessory minerals during high-temperature reworking. *Journal of Metamorphic Geology*, *42*(2), 257–289. https://doi.org/10.1111/jmg.12754

Miyashiro, A. (1961). Evolution of Metamorphic Belts. *Journal of Petrology*, *2*(3), 277–311. https://doi.org/10.1093/petrology/2.3.277

Nakano, N., Osanai, Y., Owada, M., Satish-Kumar, M., Adachi, T., Jargalan, S., Yoshimoto, A., Syeryekhan, K., & Boldbaatar, C. (2015). Multiple growth of garnet, sillimanite/kyanite and monazite during amphibolite facies metamorphism: Implications for the P-T-t and tectonic evolution of the western Altai Range, Mongolia. *Journal of Metamorphic Geology*, *33*(9), 937–958. https://doi.org/10.1111/jmg.12154

Nakano, N., Osanai, Y., Satish-Kumar, M., Adachi, T., Owada, M., Jargalan, S., Boldbaatar, C., Yoshimoto, A., & Syeryekhan, K. (2014). Paleozoic Subduction-Accretion-Closure Histories in the West Mongolian Segment of the Paleo-Asian Ocean: Evidence from Pressure-Temperature-Time-Protolith Evolution of High-Mg and -Al Gneisses in the Altai Mountains. *The Journal of Geology*, *122*(3), 283–308. https://doi.org/10.1086/675665

Nguyen, H., Hanžl, P., Janoušek, V., Schulmann, K., Ulrich, M., Jiang, Y., Lexa, O., Altanbaatar, B., & Deiller, P. (2018). Geochemistry and geochronology of Mississippian volcanic rocks from SW Mongolia: Implications for terrane subdivision and magmatic arc activity in the Trans-Altai Zone. *Journal of Asian Earth Sciences*, *164*, 322–343. https://doi.org/10.1016/j.jseaes.2018.06.029

Pan, Y., & Fleet, M. E. (1999). Kyanite in the western Superior province of Ontario: Implications for the Archean accretionary tectonics. *The Canadian Mineralogist*, *37*, 359–373.

Parfenov, L. M., Khanchuk, A. I., Badarch, G., Miller, R. J., Naumova, V. V., Nokleberg, W. J., Ogasawara, M., Prokopiev, A. V., & Yan, H. (2003). *Preliminary Northeast Asia Geodynamics Map* (Nos. 2003–205). U. S. Geological Survey. https://doi.org/10.3133/ofr03205

Pitra, P., Kouamelan, A. N., Ballèvre, M., & Peucat, J.-J. (2010). Palaeoproterozoic high-pressure granulite overprint of the Archean continental crust: Evidence for homogeneous crustal thickening (Man Rise, Ivory Coast). *Journal of Metamorphic Geology*, *28*(1), 41–58. https://doi.org/10.1111/j.1525-1314.2009.00852.x

Poujol, M., Pitra, P., Van den Driessche, J., Tartèse, R., Ruffet, G., Paquette, J. L., & Poilvet, J. C. (2016). Two-stage partial melting during the Variscan extensional tectonics (Montagne Noire, France). *International Journal of Earth Sciences*, *106*(2), 477–500. https://doi.org/10.1007/s00531-016-1369-1

Powell, R., & Holland, T. J. B. (1988). An internally consistent dataset with uncertainties and correlations: 3. Applications to geobarometry, worked examples and a computer program. *Journal of Metamorphic Geology*, *6*(2), 173–204. https://doi.org/10.1111/j.1525-1314.1988.tb00415.x

Rey, P. F., Teyssier, C., & Whitney, D. L. (2009a). Extension rates, crustal melting, and core complex dynamics. *Geology*, *37*(5), 391–394. https://doi.org/10.1130/G25460A.1

Rey, P. F., Teyssier, C., & Whitney, D. L. (2009b). The role of partial melting and extensional strain rates in the development of metamorphic core complexes. *Tectonophysics*, *477*(3–4), 135–144. https://doi.org/10.1016/j.tecto.2009.03.010

Robyr, M., Darbellay, B., & Baumgartner, L. P. (2014). Matrix-dependent garnet growth in polymetamorphic rocks of the Sesia zone, Italian Alps. *Journal of Metamorphic Geology*, *32*(1), 3–24. https://doi.org/10.1111/jmg.12055

Ryan, P. D., & Dewey, J. F. (2019). The sources of metamorphic heat during collisional orogeny: The Barrovian enigma. *Canadian Journal of Earth Sciences*, *56*(12), 1309–1317. https://doi.org/10.1139/cjes-2018-0182

Schulmann, K., Schaltegger, U., Jezek, J., Thompson, A. B., & Edel, J.-B. (2002). Rapid burial and exhumation during orogeny: Thickening and synconvergent exhumation of thermally weakened and thinned crust (Variscan orogen in Western Europe). *American Journal of Science*, *302*(10), 856–879. https://doi.org/10.2475/ajs.302.10.856

Skrzypek, E., Kawakami, T., Hirajima, T., Sakata, S., Hirata, T., & Ikeda, T. (2016). Revisiting the high temperature metamorphic field gradient of the Ryoke Belt (SW Japan): New constraints from the Iwakuni-Yanai area. *Lithos*, *260*, 9–27. https://doi.org/10.1016/j.lithos.2016.04.025

Soejono, I., Buriánek, D., Janoušek, V., Svojtka, M., Čáp, P., Erban, V., & Ganpurev, N. (2017). A reworked Lake Zone margin: Chronological and geochemical constraints from the Ordovician arc-related basement of the Hovd Zone (western Mongolia). *Lithos*, *294–295*, 112–132. https://doi.org/10.1016/j.lithos.2017.08.014

Soejono, I., Buriánek, D., Svojtka, M., Žáček, V., Čáp, P., & Janoušek, V. (2016). Mid-Ordovician and Late Devonian magmatism in the Togtokhinshil Complex: New insight into the formation and accretionary evolution of the Lake Zone (western Mongolia). *Journal of Geosciences*, *61*(1), 5–23. https://doi.org/10.3190/jgeosci.208

Soejono, I., Čáp, P., Míková, J., Janoušek, V., Buriánek, D., & Schulmann, K. (2018). Early Palaeozoic sedimentary record and provenance of flysch sequences in the Hovd Zone (western Mongolia): Implications for the geodynamic evolution of the Altai accretionary wedge system. *Gondwana Research*, *64*, 163–183. https://doi.org/10.1016/j.gr.2018.07.005

Soejono, I., Peřestý, V., Schulmann, K., Čopjaková, R., Svojtka, M., Štípská, P., Buriánek, D., Janoušek, V., & Lexa, O. (2021). Structural, metamorphic and geochronological constraints on Palaeozoic multi-stage geodynamic evolution of the Altai accretionary wedge system (Hovd Zone, western Mongolia). *Lithos*, *396–397*, 106204. https://doi.org/10.1016/j.lithos.2021.106204

Sonder, L. J., England, P. C., Wernicke, B. P., & Christiansen, R. L. (1987). A physical model for Cenozoic extension of western North America. *Geological Society, London, Special Publications*, *28*(1), 187–201. https://doi.org/10.1144/GSL.SP.1987.028.01.14

Spear, F. S., Selverstone, J., Hickmott, D., Crowley, P., & Hodges, K. V. (1984). P-T paths from garnet zoning: A new technique for deciphering tectonic processes in crystalline terranes. *Geology*, *12*(2), 87–90. https://doi.org/10.1130/0091-7613(1984)12

Stacey, J. S., & Kramers, J. D. (1975). Approximation of terrestrial lead isotope evolution by a two-stage model. *Earth and Planetary Science Letters*, *26*(2), 207–221. https://doi.org/10.1016/0012-821X(75)90088-6

Štípská, P., Hacker, B. R., Racek, M., Holder, R., Kylander-Clark, A. R. C., Schulmann, K., & Hasalová, P. (2015). Monazite Dating of Prograde and Retrograde P–T–d paths in the Barrovian terrane of the Thaya window, Bohemian Massif. *Journal of Petrology*, *56*(5), 1007–1035. https://doi.org/10.1093/petrology/egv026

Štípská, P., Peřestý, V., Soejono, I., Schulmann, K., Kylander–Clark, R. C. A., Aguilar, C., Collett, S., Racek, M., Míková, J., Dorjsuren, O., & Novotná, N. (2023). Anticlockwise metamorphic paths at ca. 890–790 Ma from the NE Baidrag block, Mongolia, indicate back-arc compression at the Rodinia periphery. *Geoscience Frontiers*, *14*(2), 101520. https://doi.org/10.1016/j.gsf.2022.101520

Štípská, P., Powell, R., & Racek, M. (2014). Rare eclogite-mafic granulite in felsic granulite in Blanský les: precursor of intermediate granulite in the Bohemian Massif? *Journal of Metamorphic Geology*, *32*(4), 325–345. https://doi.org/10.1111/jmg.12075

Štípská, P., Schulmann, K., Lehmann, J., Corsini, M., Lexa, O., & Tomurhuu, D. (2010). Early Cambrian eclogites in SW Mongolia: Evidence that the Palaeo-Asian Ocean suture extends further east than expected. *Journal of Metamorphic Geology*, *28*(9), 915–933. https://doi.org/10.1111/j.1525-1314.2010.00899.x

Štípská, P., Schulmann, K., & Powell, R. (2008). Contrasting metamorphic histories of lenses of high-pressure rocks and host migmatites with a flat orogenic fabric (Bohemian Massif, Czech Republic): A result of tectonic mixing within horizontal crustal flow? *Journal of Metamorphic Geology*, *26*(6), 623–646. https://doi.org/10.1111/j.1525-1314.2008.00781.x

Štípská, P., Schulmann, K., Racek, M., Lardeaux, J. M., Hacker, B. R., Kylander-Clark, A. R. C., Holder, R., & Košuličová, M. (2020). Finite pattern of Barrovian metamorphic zones: Interplay between thermal reequilibration and post-peak deformation during continental collision—insights from the Svratka dome (Bohemian Massif). *International Journal of Earth Sciences*, *109*(4), 1161–1187. https://doi.org/10.1007/s00531-019-01788-6

Sukhbaatar, T., Lexa, O., Schulmann, K., Aguilar, C., Štípská, P., Wong, J., Jiang, Y., Míková, J., & Zhao, D. (2022). Paleozoic Geodynamics and Architecture of the Southern Part of the Mongolian Altai Zone. *Tectonics*, *41*(8). https://doi.org/10.1029/2022TC007498

Sukhorukov, V. P., Polyansky, O. P., Krylov, A. A., & Zinoviev, S. V. (2016). Reconstruction of the metamorphic P–T path from the garnet zoning in aluminous schists from the Tsogt Block, Mongolian Altai. *Petrology*, *24*(4), 409–432. https://doi.org/10.1134/S0869591116040068

Tagliaferri, A., Schenker, F. L., Ulianov, A., Maino, M., & Schmalholz, S. M. (2023). Implications of New Geological Mapping and U-Pb Zircon Dating for the Barrovian Tectono-Metamorphic Evolution of the Lepontine Dome (Central European Alps). *Geochemistry, Geophysics, Geosystems*, *24*(3), e2022GC010772. https://doi.org/10.1029/2022GC010772

Teyssier, C., & Whitney, D. L. (2002). Gneiss domes and orogeny. *Geology*, *30*(12), 1139–1142. https://doi.org/10.1130/0091-7613(2002)030

Thiessen, E. J., Gibson, H. D., Regis, D., Pehrsson, S. J., Cutts, J. A., & Smit, M. A. (2019). High-grade metamorphism flying under the radar of accessory minerals. *Geology*, *47*(6), 568–572. https://doi.org/10.1130/G45979.1

Tirel, C., Brun, J.-P., & Burov, E. (2008). Dynamics and structural development of metamorphic core complexes. *Journal of Geophysical Research: Solid Earth*, *113*(B4), B04403. https://doi.org/10.1029/2005JB003694

Tirel, C., Brun, J.-P., & Sokoutis, D. (2006). Extension of thickened and hot lithospheres: Inferences from laboratory modeling. *Tectonics*, *25*(1). https://doi.org/10.1029/2005TC001804

Tomascak, P. B., Krogstad, E. J., & Walker, R. J. (1996). U-Pb Monazite Geochronology of Granitic Rocks from Maine: Implications for Late Paleozoic Tectonics in the Northern Appalachians. *The Journal of Geology*, *104*(2), 185–195. https://doi.org/10.1086/629813

Vanderhaeghe, O. (2012). The thermal–mechanical evolution of crustal orogenic belts at convergent plate boundaries: A reappraisal of the orogenic cycle. *Journal of Geodynamics*, *56–57*, 124–145. https://doi.org/10.1016/j.jog.2011.10.004

Vanderhaeghe, O., Teyssier, C., & Wysoczanski, R. (1999). Structural and geochronological constraints on the role of partial melting during the formation of the Shuswap metamorphic core complex at the latitude of the Thor-Odin dome, British Columbia. *Canadian Journal of Earth Sciences*, *36*(6), 917–943. https://doi.org/10.1139/e99-023

Varga, J., Raimondo, T., Daczko, N. R., & Adam, J. (2020). Experimental alteration of monazite in granitic melt: Variable U–Th–Pb and REE mobility during melt-mediated coupled dissolution-precipitation. *Chemical Geology*, *544*, 119602. https://doi.org/10.1016/j.chemgeo.2020.119602

Vermeesch, P. (2018). IsoplotR: A free and open toolbox for geochronology. *Geoscience Frontiers*, *9*(5), 1479–1493. https://doi.org/10.1016/j.gsf.2018.04.001

Viete, D. R., & Lister, G. S. (2017). On the significance of short-duration regional metamorphism. *Journal of the Geological Society*, *174*(3), 377–392. https://doi.org/10.1144/jgs2016-060

Viete, D. R., Richards, S. W., Lister, G. S., Oliver, G. J. H., & Banks, G. J. (2010). Lithospheric-scale extension during Grampian orogenesis in Scotland. *Geological Society, London, Special Publications*, *335*(1), 121–160. https://doi.org/10.1144/SP335.7

Wang, X., Huang, X.-L., & Yang, F. (2021). Geochronology and geochemistry of the Xiaoqinling Taihua Complex in the southern Trans-North China Orogen: Implications for magmatism during the early Paleoproterozoic global tectono-magmatic shutdown. *Lithos*, *402–403*, 106248. https://doi.org/10.1016/j.lithos.2021.106248

Waters, D. J. (2001). The significance of prograde and retrograde quartz-bearing intergrowth microstructures in partially melted granulite-facies rocks. *Lithos*, *56*(1), 97–110. https://doi.org/10.1016/S0024-4937(00)00061-X

Wei, C., Clarke, G., Tian, W., & Qiu, L. (2007). Transition of metamorphic series from the Kyanite- to andalusite-types in the Altai orogen, Xinjiang, China: Evidence from petrography and calculated KMnFMASH and KFMASH phase relations. *Lithos*, *96*(3–4), 353–374. https://doi.org/10.1016/j.lithos.2006.11.004

Weinberg, R. F., Wolfram, L. C., Nebel, O., Hasalová, P., Závada, P., Kylander-Clark, A. R. C., & Becchio, R. (2020). Decoupled U-Pb date and chemical zonation of monazite in migmatites: The case for disturbance of isotopic systematics by coupled dissolution-reprecipitation. *Geochimica et Cosmochimica Acta*, *269*, 398–412. https://doi.org/10.1016/j.gca.2019.10.024

Wells, P. (1980). Thermal models for the magmatic accretion and subsequent metamorphism of continental crust. *Earth and Planetary Science Letters*, *46*(2), 253–265. https://doi.org/10.1016/0012-821X(80)90011-4

Wernicke, B. P., & Axen, G. J. (1988). On the role of isostasy in the evolution of normal fault systems. *Geology*, *16*(9), 848–851. https://doi.org/10.1130/0091-7613(1988)016

Wernicke, B. P., England, P. C., Sonder, L. J., & Christiansen, R. L. (1987). Tectonomagmatic evolution of Cenozoic extension in the North American Cordillera. *Geological Society, London, Special Publications*, *28*(1), 203–221. https://doi.org/10.1144/GSL.SP.1987.028.01.15

White, R. W., Powell, R., & Clarke, G. L. (2002). The interpretation of reaction textures in Fe-rich metapelitic granulites of the Musgrave Block, central Australia: Constraints from mineral equilibria calculations in the system $K_2O$–FeO–MgO–$Al_2O_3$–$SiO_2$–$H_2O$–$TiO_2$–$Fe_2O_3$. *Journal of Metamorphic Geology*, *20*(1), 41–55. https://doi.org/10.1046/j.0263-4929.2001.00349.x

White, R. W., Powell, R., Holland, T. J. B., Johnson, T. E., & Green, E. C. R. (2014). New mineral activity–composition relations for thermodynamic calculations in metapelitic systems. *Journal of Metamorphic Geology*, *32*(3), 261–286. https://doi.org/10.1111/jmg.12071

White, R. W., Powell, R., Holland, T. J. B., & Worley, B. A. (2000). The effect of $TiO_2$ and $Fe_2O_3$ on metapelitic assemblages at greenschist and amphibolite facies conditions: Mineral equilibria calculations in the system $K_2O$–FeO–MgO–$Al_2O_3$–$SiO_2$–$H_2O$–$TiO_2$–$Fe_2O_3$. *Journal of Metamorphic Geology*, *18*(5), 497–511. https://doi.org/10.1046/j.1525-1314.2000.00269.x

White, R. W., Powell, R., & Johnson, T. E. (2014). The effect of Mn on mineral stability in metapelites revisited: New a–x relations for manganese-bearing minerals. *Journal of Metamorphic Geology*, *32*(8), 809–828. https://doi.org/10.1111/jmg.12095

Wilhem, C., Windley, B. F., & Stampfli, G. M. (2012). The Altaids of Central Asia: A tectonic and evolutionary innovative review. *Earth-Science Reviews*, *113*(3–4), 303–341. https://doi.org/10.1016/j.earscirev.2012.04.001

Williams, M. A., Kelsey, D. E., & Rubatto, D. (2022). Thorium zoning in monazite: A case study from the Ivrea–Verbano zone, NW Italy. *Journal of Metamorphic Geology*, *40*(6), 1015–1042. https://doi.org/10.1111/jmg.12656

Windley, B. F., Alexeiev, D., Xiao, W., Kröner, A., & Badarch, G. (2007). Tectonic models for accretion of the Central Asian Orogenic Belt. *Journal of the Geological Society*, *164*(1), 31–47. https://doi.org/10.1144/0016-76492006-022

Wolf, M. B., & London, D. (1995). Incongruent dissolution of REE- and Sr-rich apatite in peraluminous granitic liquids; differential apatite, monazite, and xenotime solubilities during anatexis. *American Mineralogist*, *80*(7–8), 765–775. https://doi.org/10.2138/am-1995-7-814

Wolfram, L. C., Weinberg, R. F., Hasalová, P., & Becchio, R. (2017). How Melt Segregation Affects Granite Chemistry: Migmatites from the Sierra de Quilmes, NW Argentina. *Journal of Petrology*, *58*(12), 2339–2364. https://doi.org/10.1093/petrology/egy010

Xia, X., Sun, M., Geng, H., Sun, Y., Wang, Y., & Zhao, G. (2011). Quasi-simultaneous determination of U-Pb and Hf isotope compositions of zircon by excimer laser-ablation multiple-collector ICPMS. *Journal of Analytical Atomic Spectrometry*, *26*(9), 1868–1871. https://doi.org/10.1039/c1ja10116a

Yakymchuk, C., & Brown, M. (2014). Behaviour of zircon and monazite during crustal melting. *Journal of the Geological Society*, *171*(4), 465–479. https://doi.org/10.1144/jgs2013-115

Závada, P., Štípská, P., Hasalová, P., Racek, M., Jeřábek, P., Schulmann, K., Kylander-Clark, A., & Holder, R. (2021). Monazite geochronology in melt-percolated UHP meta-granitoids: An example from the Erzgebirge continental subduction wedge, Bohemian Massif. *Chemical Geology*, *559*, 119919. https://doi.org/10.1016/j.chemgeo.2020.119919

SUPPLEMENTARY MATERIALS

## Supplementary material

Download: https://ajsonline.org/article/155605-permian-syn-extensional-barrovian-metamorphism-in-the-envelope-of-a-migmatite-dome-of-the-mongolian-altai-petrostructural-and-geochronological-argum/attachment/325762.zip